EXPERIMENTS AND MODELING OF MOTILITY AND CHEMOTAXIS OF *PSEUDOMONAS AERUGINOSA*

BY

QIAN, CHEN

A THESIS SUBMITTED

FOR THE DEGREE OF

DOCTOR OF PHILOSOPHY IN MECHANOBIOLOGY

MECHANOBIOLOGY INSTUTUTE

NATIONAL UNIVERSITY OF SINGAPORE

2014

Declaration

I hereby declare that this thesis is my original work and it has been written by me in its entirety. I have duly acknowledged all the sources of information which have been used in the thesis.

This thesis has also not been submitted for any degree in any university previously.

Qian, Chen

21 Jul 2014

Acknowledgements

First of all, I would like to express my sincere gratitude to my supervisors Dr. Keng-Hwee Chiam and Prof. Boon Chuan Low, for being patient advisors in this long journey. Thank you for all the discussions and encouragement, especially for being supportive of my little adventure deviating away from the research work of this thesis.

I want to thank the other members of my thesis committee: Prof. Jie Yan and Prof. Sanjay Swarup. Prof. Yan, as a physicist, provided many insightful comments regarding my experiments, and Prof. Swarup, as a collaborator of much of my work in this thesis gave great advice from the view of a microbiologist. I also want to thank my collaborators, Dr. Chui Ching Wong for helping me with experiments, and Prof. Sungsu Park for the fruitful collaboration on multiple projects. In addition I thank all members in Dr. Chiam's group for the supportive working environment.

Moreover I want to thank MBI as a whole for bringing people with different views and disciplines together, for the kind support in funding and for the administrative work as I am among the first batch of students.

To my amazing parents, thank you for making me what I am today and for making me feel loved, though you are so far away and I did not spend enough time with you in the past few years. Thank you my dear friends for being there and making my life full of joy.

Experiments and modeling of motility and chemotaxis of *Pseudomonas aeruginosa*

QIAN, Chen

National University of Singapore, 2014

Supervisors:

Dr. Low Boon Chuan

Dr. Chiam Keng-Hwee

SUMMARY

The “run-and-tumble” model is well-established for the motility and chemotaxis of peritrichous bacteria such as *Escherichia coli*. However, for monotrichous bacteria constrained in a "run-and-reverse" motion, the mechanisms are still not well-understood. In this thesis, we combined experiments and computational modeling to study the motility and chemotaxis of monotrichous *Pseudomonas aeruginosa*. We developed an analytical platform called Bacterial Tethering Analysis Program (BTAP) that can accurately analyze tethering experiments of monotrichous bacteria such as *P. aeruginosa*. Using this, we first discovered a novel pause phase that allows *P. aeruginosa* to change directions. Next, we found that *P. aeruginosa* undergoes chemotaxis by rectifying the run-and-reverse motion, leading to longer runs in the direction of increasing chemoattractant. Finally, we proposed a theoretical model for how such rectification can be implemented in a molecular circuit involving the chemotaxis regulatory protein CheY and the flagella motor proteins. Simulations from the model show good agreement with experiments.

TABLE OF CONTENTS

LIST OF TABLES

LIST OF FIGURES

1. INTRODUCTION

1.1 Overview

Starting from Purcell's influential paper, 'Life at low Reynolds number' [1], the mechanisms of motility of microorganisms in the microscopic environment have been of much interest to many scientists. In an environment of low Reynolds number, the fluid forces acting on swimming cells are dominated by the viscous effect rather than inertia, and can be vastly different from our experiences in the macroscopic world. The absence of inertia forbids many types of locomotion strategies that swimmers adopt in the macroscopic world. To cope with this, microorganisms have evolved different molecular apparatus to facilitate their swimming in the fluidic environment, including cilia and flagella. Many of the swimming microorganisms rotate one or more helically-shaped flagella for propulsion [2]–[4]. From decades of research, the motility of peritrichous bacteria (having multiple flagella covering the cell's surface) has been well studied from using *Escherichia coli* as a model species [3], [5]. In particular, the "run-and-tumble" model has been established for its motility and chemotaxis. The *E. coli* bacterium has multiple flagella growing over its cell body and these, when synchronized in counterclockwise (CCW) rotation driven by molecular motors (viewed from behind the cell), form a rotating bundle to propel the bacterium in a relative straight trajectory in the aquatic environment. The bundle at times is disrupted by a change in the rotation direction (to clockwise, CW) of one or more motors. Because of this, the bacterium stops swimming and tumbles to

reorient to a new direction before moving again. By adjusting the ratio between swimming and tumbling, *E. coli* cells are able to climb up the chemoattractant gradient and become enriched in regions where concentrations of their favorable chemicals are at maximum. This behavior model, together with the studies of *E. coli*'s molecular pathways in sensing and response to the ambient chemicals, elucidated the mechanism of chemotaxis of *E. coli* [6], [7]; for a detailed review see [3].

Most of the current understandings of bacteria motility and chemotaxis are based on the peritrichous bacteria *E. coli*. However, few motility mechanisms have been established for monotrichous polar bacteria (one with only one flagellum at one end of the cell body) such as *Pseudomonas aeruginosa*, much less the mechanisms of their chemotaxis. This problem is triggered by a fundamental question in physics. As a monotrichous bacterium, a *P. aeruginosa* cell has only one flagellum located at the pole of its cell body. Unlike the case of *E. coli*, in which two rotation directions of the molecular motors give rise to two asymmetrical moving patterns (CCW to straight swimming and CW to change of directions), monotrichous bacteria such as *P. aeruginosa* do not form bundles and therefore cannot re-orient. Limited by physical laws at low Reynolds number environment (see details in Section 2.1), theoretically the movement of this type of bacteria is confined in a one-dimensional space – the rotations of the single molecular motor in CCW and CW directions only lead to the forward and backward movement of the bacterium, respectively. It is still not fully clear how monotrichous bacteria

change their orientations to explore the three dimensional physical space they live in. Therefore *P. aeruginosa* becomes a good subject for studies to understand the motility and chemotaxis in monotrichous bacteria. In addition, as an opportunistic pathogen, *P. aeruginosa* colonize on surfaces such as human lungs, the urinary tract, or on medical devices such as catheters or implants, and form biofilms. This plays an important part of its virulence, as the production of exopolysaccharides in forming the biofilm make it hard to be eliminated by human white blood cells. Their resilience to harsh conditions and natural resistance to antibiotics such as penicillin make them an emerging threat in clinical settings. Many members of the *Pseudomonas* family also play significant roles in their environment. For example, *Pseudomonas putida* has the capability to biodegrade organic waste; *Pseudomonas stutzeri* is known to colonize roots of plants and fix nitrogen. Therefore, elucidating the motility and chemotactic mechanisms for *P. aeruginosa* can be beneficial in many studies extending to bioremediation and host-pathogen interactions.

1.2 Thesis outline

The rest of this thesis is organized as follows.

Chapter 2 is a literature review of the up-to-date knowledge in bacterial motility and chemotaxis, primarily accumulated from the studies of model species *E. coli*. Section 2.1 gives an introduction of the physics at the low Reynolds number environment, which may be counter-intuitive regarding movement and motion developed from our daily life. Hopefully this will help

the readers to develop a sense of the lives for microswimmers. Section 2.2 provides a detailed review of the apparatus that microorganisms developed to facilitate motions in low Reynolds environment – the bacterial rotary motor (BRM). This section will start from the molecular structure of the motor and then follow with its two basic functions: rotation and direction switch. Section 2.3 reviews the motility and chemotaxis in the model species *E. coli* in both macro behavioral level and micro molecular level. Following that are some computational models having been developed which can be used to simulate *E. coli*'s behaviors. Section 2.4 and 2.5 reports the current knowledge of the motility and chemotaxis of monotrichous bacteria, and in particular the knowledge of *P. aeruginosa* and how it is linked with the biofilms formation. Section 2.6 summarizes experimental techniques developed in this community for the study of bacterial motility and chemotaxis.

Having provided the background knowledge that is relevant to this thesis, Chapter 3 and Chapter 4 consist of two related studies aimed at addressing some of the key questions raised in Chapter 2. Chapter 3 develops a novel computational tool and software platform (Bacterial Tethering Analysis Program, BTAP) that solved some of the problems in studying monotrichous bacteria and proposes a "run-reverse-turn" model for *P. aeruginosa*'s motility. In particular, the work of Chapter 3 identifies a pause phase of the molecular motor that may enhance the motion capability of monotrichous bacteria. Building on the results from Chapter 3, studies in Chapter 4 further explore the chemotactic response of *P. aeruginosa* and

reveal a “rectified run-and-reverse” strategy for *P. aeruginosa*’s chemotaxis. A molecular model is proposed to explain this observation.

My final conclusions are followed in Chapter 5, bringing a summary of my work and a closure of this thesis.

2 BACKGROUND

In this chapter I will introduce the background information that is relevant to this thesis. I will start with the basic physics of microswimmers and then introduce the structure and functions of the bacterial rotary motor. I will also introduce the established motility and chemotaxis model in *E. coli*, these in monotrichous bacteria especially in *P. aeruginosa*, and some of the experimental techniques involved. In the last part I will identify some research gaps in the field and how this thesis aims to solve them.

2.1 Life at low Reynolds number

2.1.1 Reynolds number

The Reynolds number of an object moving in a fluid is defined as:

$$Re = \frac{\rho L v}{\mu} \tag{2.1}$$

where L and v are the characteristic length and velocity of the object, and ρ and μ are density and kinematic viscosity of the fluid, respectively. It is a dimensionless parameter that describes flow patterns under different conditions.

One interpretation of the Reynolds number is by looking at the Navier-Stokes equations, the governing equations that describe the motion of fluids. The Navier-Stokes equations for an incompressible Newtonian fluid are:

$$\rho\left(\frac{\partial \mathbf{v}}{\partial t}+\mathbf{v}\cdot\nabla\mathbf{v}\right)=-\nabla p+\mu\nabla^2\mathbf{v}+\mathbf{f} \qquad (2.2)$$

$$\nabla\cdot\mathbf{v}=0 \qquad (2.3)$$

where ρ and μ are the fluid density and kinematic viscosity respectively, $\mathbf{v}$ is the flow velocity, p is the pressure, f are body forces acting on the fluid (per unit volume) and ∇ is the gradient operator. The left-hand-side of equation (2.2), often written in the material derivative $\rho\left(D\mathbf{v}/Dt\right)$ represents the effect of inertia on the fluid while the terms on the right-hand-side describe effects of pressure, viscosity and other body forces respectively. Equation (2.3) is the continuity equation to state a conservation of volume. In practice one always first attempts to convert this equation to a dimensionless one, so that the behavior of the fluid does not depend directly on the scale of the system. If we multiply equation (2.2) by $\left(L/V^2\rho\right)$, where L is the characteristic length (m), V is the mean velocity relative to the fluid (m/s) and ρ is the density of the fluid (kg/m^3), the equation can be re-written as:

$$\frac{D\mathbf{v}'}{Dt'}=-\nabla' p'+\frac{\mu}{\rho LV}\nabla'^2\mathbf{v}'+\mathbf{f}' \qquad (2.4)$$

where we define $\mathbf{v}'=\mathbf{v}/V$, $t'=tV/L$, $\nabla'=\nabla/L$, $p'=p/\rho V^2$, $\mathbf{f}'=\mathbf{f}L/V^2$. Note that the term $\mu/\rho LV=1/Re$, so after dropping the primes the dimensionless Navier-Stokes equation (2.4) becomes:

$$\frac{D\mathbf{v}}{Dt} = -\nabla p + \frac{1}{Re}\nabla^2\mathbf{v} + \mathbf{f} \qquad (2.5)$$

This shows that all incompressible Newtonian flows with same Reynolds numbers behave similar, irrespective of physical dimensions. Also note that, when $Re \gg 1$ the viscous term in equation (2.5) can be neglected. Therefore the inertial forces dominate the flow; on the other hand, when $Re \ll 1$, the viscous forces dominate the flow and the inertia term $D\mathbf{v}/Dt$ can be neglected.

To develop an intuitive sense of the Reynolds number, one can do a back-of-the-envelope calculation of the Reynolds number of a person swimming in a pool. In water ($\rho \approx 10^3$ kg·m^{-3}, $\mu \approx 10^{-3}$ kg·s^{-1}·m^{-1}), a human ($L \approx 1$m) typically swims at $v \approx 1$ m/s. This gives a Reynolds number at the order of (10^6). For a fish with a size of $L \approx 0.1$m, the Reynolds number gets down to $\mathcal{O}(10^5)$, which is still much higher than 1. For a bird ($L \approx 0.1$ m, $v \approx 10$ m/s) flying in the air ($\rho \approx 1$ kg·m^{-3}, $\mu \approx 10^{-5}$ kg·s^{-1}·m^{-1}), the Reynolds number is also at the order of (10^5). Clearly we as humans live in a world of predominantly inertial forces and all our experiences are based on this world of high Reynolds number.

Now consider the case at low Reynolds number. A typical bacterium such as *E. coli* has a size of 1 μm (=10^{-6} m) and moves at a speed of 10 μm/s (=10^{-5} m/s), which gives us a Reynolds number of (10^{-5}). To make an analogy of human swimming at the same Reynolds number, one has to swim in a pool

full of honey ($\rho \approx 10^3$ kg·m^{-3}, $\mu \approx 10$ kg·s^{-1}·m^{-1}) and be forbidden to move any part of his body faster than 1 mm/min. It is easy to see that at low Reynolds number, all the swimming techniques developed by human will fail and the motion becomes extremely hard.

Now consider the effect of forces in such a system. If a swimmer, which swims by deforming its body suddenly stops its body deform, it will eventually be stopped by the fluid due to the drag force. For motions at high Reynolds number, such as human swimming, the drag force is primarily the inertial force determined by the inertial term in the left-hand-side of equation (2.2):

$$\mathbf{F} = \rho\left(\mathbf{v}\cdot\nabla\mathbf{v}\right) \sim \rho V^2 L^2 \tag{2.6}$$

According to Newton's second law $\mathbf{F} = m\mathbf{a}$ (m is the mass and $\mathbf{a}$ is the acceleration rate), one can estimate the coasting time of such a swimmer:

$$t_{coast} \sim \frac{V}{a} = \frac{Vm}{F} \sim \frac{Vm}{\rho V^2 L^2} \tag{2.7}$$

Assuming the swimmer has similar density ρ as water and has a dimension ~L,

$$t_{coast} \sim \frac{V\left(\rho L^3\right)}{\rho V^2 L^2} = \frac{L}{V} \tag{2.8}$$

In a human swimming case this is in the order of seconds. Similarly one can calculate the relative costing distance:

$$\frac{d_{coast}}{L} \sim \frac{V^2}{aL} \sim 1 \tag{2.9}$$

These results show that after stopping strokes, a human swimmer will coast for a distance about his body length in the order of seconds.

On the contrary, for motions at low Reynolds number, the drag force is dominated by the viscous force:

$$\mathbf{F} = \mu\nabla^2\mathbf{v} \sim \mu VL \tag{2.10}$$

The coasting time and relative coasting distance are:

$$t_{coast} \sim \frac{V}{a} \sim Re\frac{L}{V} \tag{2.11}$$

$$\frac{d_{coast}}{L} \sim \frac{V^2}{aL} \sim Re \tag{2.12}$$

For a swimmer swimming at a speed of the same order of magnitude of its body length per second, both coasting time and relative coasting distance equal to the Reynolds number. These means that at low Reynolds number, a swimmer such as *E. coli* ($Re = 10^{-5}$) will stop in around 10^{-5} second within a distance around 10^{-5} of its body length. The implication of this result is that all

motions at low Reynolds number are driven by forces at the moment of application , and if these forces are gone, motion stops immediately [1].

Life at low Reynolds number is somewhat counter intuitive from our daily, high Reynolds number experience.

2.1.2 The Scallop theorem

As mentioned in the previous section, at low Reynolds number the inertial forces become irrelevant to the motion in the fluid. Therefore the Navier-Stokes equation (2.2) reduces to the Stokes equation:

$$\nabla p = \mu \nabla^2 \mathbf{v} \tag{2.13}$$

Note that this equation is independent of time. This leads to two important insights of the locomotion at low Reynolds number [1]. The first is the rate-independence of the movement: If a microswimmer is swimming by deforming its body, the distance it travels does not depend on the rate at which its body deforms. The second is the invalidity of reciprocal motions (or the Scallop Theorem): If a swimmer deforms its body through a sequence of configurations and reverts to the original shape following exactly the same sequence of configurations reversed, there can be no net displacement and swimming becomes impossible. Note that this does not require the motions to be strictly time-reversal (same configuration at the same time if reversed), but the sequence of configurations being the same in time reversal (so rate of change does not matter). The name comes from the motion of scallops. A

scallop opens its shells slowly and closes them fast to jet water out in a direction, and as a result of that the scallop moves in the opposite direction. The faster it closes its shells the longer distance it moves. A scallop in the real world repeats this sequence of motions to move a long distance in the sea. In a world at low Reynolds number however, a scallop would be doomed. Such a sequence of motions will not result in any net movement on average – the scallop will move a slight distance as it opens its shells and returns back to its exact final position as it closes its shells, fast or slow.

2.1.3 Evolved strategies of microswimmers & swimming organelles

Based on the physical restrictions of the motion at low Reynolds number, many of the common swimming strategies exist in the world of high Reynolds number are not applicable at the microscopic level. Microswimmers have evolved many mechanisms in nature in such an environment. Spirochaetes are long helical bacteria that have axial filaments beneath the outer membrane, which help rotating the whole cell body in a spiral fashion, enabling the bacteria to move [8]. The periodic motion of the spiral shaped cell body is non-reciprocal therefore it breaks the right-left symmetry and generates a non-zero force on average to propel the cell forward. Other bacteria have developed organelles to facilitate swimming, notably cilia and flagella. Cilia are flexible slender tubes protruding from cell bodies and are more common in eukaryotic cells or larger microorganisms. They usually consist of nine microtubule doublets arranged along a circumference surrounding another microtubule doublet in the center. Cilia usually perform

back and forth strokes to facilitate motions. A typical example is *Paramecium*, which is covered by thousands of cilia over its surface and is propelled by the coordinated beat of these cilia [9].

What is more relevant to this thesis is the flagellum. A flagellum is a lash-like appendage protruding from the cell body of some microorganisms. In eukaryotic cells such as some of the spermatozoa the flagella, consists of microtubules, undergo a whipping undulation by sliding microtubules relative to the others [9], [10]. Flagella in prokaryotic cells such as *E. coli* consists of flagellins and can form a relative rigid helix (like a corkscrew) that is rotated by a flagellar motor embedded in the cell wall [2]. The flagellar filament has a diameter of about 20 nm, consists of single protein called flagellin. The shape of the flagellar filament depends on the arrangement of the flagellin monomers [11] and in normal condition without external forces, the filament forms a left-hand helix with a pitch of around 2.5 μm and diameter around 0.5 μm of the helix [12]. The flagellum is connected to the rotary motor by a flexible joint called hook [4], [11]. By rotating the flagellum, the propagated wave of the flagellar helix travels in a time-irreversible manner that beat the limitations mentioned in the scallop theorem and propels the bacteria. The exact hydrodynamics of this process is out of the scope of this thesis and are summarized in the review [13].

Bacteria may have different numbers of flagella with different arrangements round the cell body (Figure 2.1). Monotrichous bacteria are those with only single flagellum, such as *P. aeruginosa*. Amphitrichous

bacteria are those having a single flagellum on each of the ends of the cell's body. Lophotrichous bacteria are those with multiple flagella growing closely from the only one end of the bacteria's surfaces. Peritrichous bacteria are those with multiple flagella growing over the surface, such as *E. coli*. In the case of *E. coli*, when all the flagella rotate in a counter-clockwise way (when viewed from the end tip of the flagella to the motor), they form a bundle and act as one filament; when one or more flagella rotate in a clockwise way, the bundle is separated [14], [15].

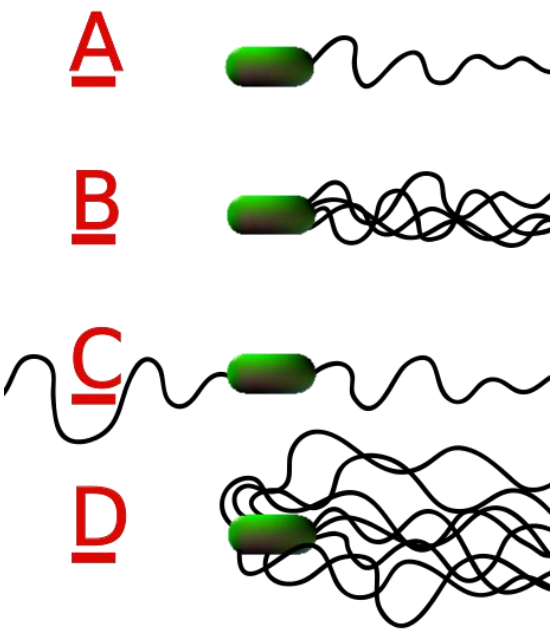

Figure 2.1 Illustrations of different bacteria flagella arrangements

(A) Monotrichous bacteria; (B) Lophotrichous bacteria; (C) Amphitrichous bacteria; (D) Peritrichous bacteria. The figure is taken from Wikipedia.org

2.2 The flagellar motor

The flagellar rotary motor is the largest organelle in a bacterium. The most well studied flagellar motor is the one in *E. coli*. The following section of the literature review will use *E. coli*'s flagellar motor as an example to demonstrate the structure and functions of the motor.

2.2.1 The molecular structure of the flagellar motor

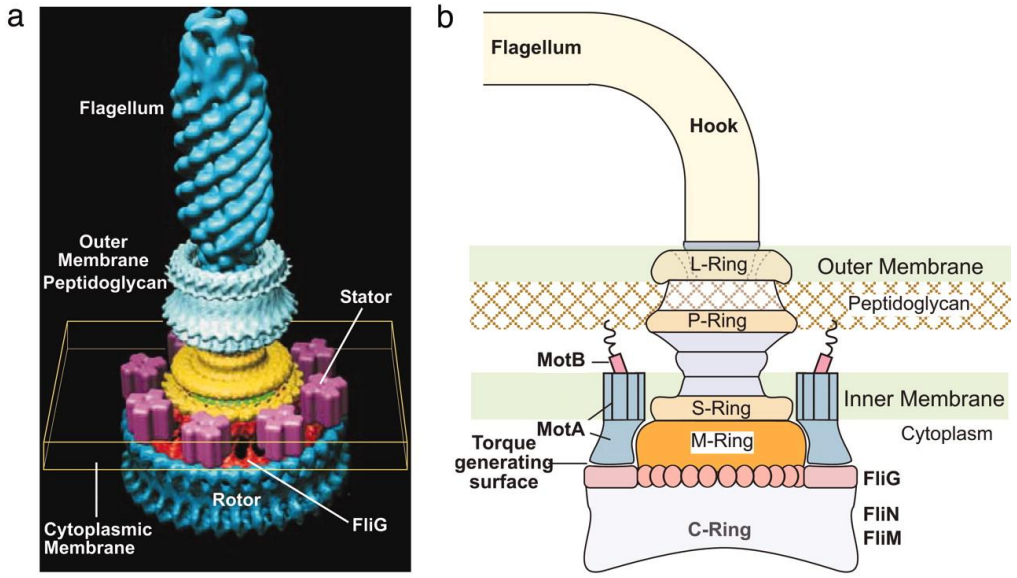

Figure 2.2 The molecular structure of the bacterial flagellar motor

(A) The overall 3D structure of the motor. (B) A schematic illustration of the key structural components of the flagellar motor. The cell has two layers of lipid membranes and a more rigid peptidoglycan cell wall in between. The flagellum and hook are components outside the outer membrane, driven by the rotation of the motor. The L-Ring and P-Ring, embedded on the cell wall work as a bushing. The S-Ring, M-Ring, C-Ring and the rod connecting S-Ring to the hook form the rotor. The MotA/ MotB complex, partly anchored to the cell wall, is the stator. Torque is generated at the surface between FliG proteins on the C-Ring and MotA proteins. The electro-chemical potential transfers to a mechanical force on MotA/MotB, which drives the rotation of the rotor. The

figure is taken from [16]

Over decades, the overall structure of *E. coli*'s flagellar motor has been examined by genetic and biochemical studies and verified by electron microscopy (EM). The *E. coli*'s flagellar motor has a molecular mass of around 11 MDa, with around 11 components (Figure 2.2) from 40 gene products [11]. *E. coli* is a Gram-negative bacterium, so it has multiple layers of membrane structure: a peptidoglycan cell wall in between the outer and inner (cytoplasmic) membranes. The flagellum and the hook are components outside the outer membrane. The flagellum is a long (~10 μm) and thin (~20 nm) helical filament shaped like a screw. The flagellum is a tubular polymer consists of 11 helical protofilaments containing monomer proteins called flagellin. At steady rotation, the flagellar filament is a rigid propeller. The hook links the flagellum to the rotary motor which drives the rotation of the flagellum. Similar to a flagellum, a hook has 11 protofilaments, but is much more flexible. Like any rotary motor, the motor can be separated into a rotor and a stator. The rotor rotates relative to the cell wall and the stator is the stationary part of the motor which is anchored to the cell wall. From outside to the inside, the motor consists of several circular structures: an L-Ring, a P-Ring, an S-Ring, a-M-ring (usually called together as the MS-Ring), the C-Ring and the MotA and MotB proteins (Figure 2.2 B). The L-Ring (FlgH) and P-Ring (FlgI) are hollow rings embedded in the outer membrane and peptidoglycan cell wall, respectively, and serve as a bushing between the outer parts (the hook) and the rotor (MS-Ring and C-Ring). A rod passes through the L and the P rings to connect the hook and the MS-Ring (FliF). The M-Ring

and the S-Ring were originally thought to be two rings [17] but were later discovered to comprise different domains of the same protein (FliF) and function as one [18], [19]. The cytoplasmic face of the MS-Ring attaches to the C-Ring, which consists of FliG, FliN and FliM. MotA and MotB, which cross the inner membrane and are arranged in a ring surrounding the MS-Ring, forming the stator of the motor. In particular, MotA is embedded in the inner membrane while MotB anchors MotA to the more rigid peptidoglycan cell wall [17]. The surface between MotA/B units and the FliG proteins on the C-Ring are thought to generate the torque and drive the rotation of the rotor.

2.2.2 How does the motor rotate?

The *E. coli*'s rotor can rotate at a speed of 100 Hz [11]. It is powered by chemical and electrical potential from the concentration difference of ions between the cytoplasm and the inner-outer membrane gap. To now two types of ions have been linked to the bacterial flagellar motor: sodium (in marine *Vibrio* species) and proton (in *E. coli*). The work an ion can do during crossing the inner membrane, or the motor's ion-motive force (IMF) is therefore called sodium-motive force (SMF) and proton-motive force (PMF) respectively. The IMF is a mixture of an electrical component and a chemical component:

$$\mathrm{IMF} = \left(V_i - V_0\right) + \frac{k_B T}{e} \ln \frac{C_i}{C_o} \tag{2.14}$$

where V_i and V_o are electrical potential inside and outside of the inner membrane, respectively, C_i and C_o the concentration of ions inside

and outside the inner membrane, respectively, k_B the Boltzmann's constant, T the absolute temperature and e the charge of the corresponding ion. The first term on the right hand side is the actual voltage difference across the inner membrane. The second term is the voltage difference expected based on equilibrium ion concentrations inside and outside of the inner membrane, hence the Nernst potential. The result of the two terms indicates a non-equilibrium high free energy state that drives the motion of the molecular motor.

The C-Ring contains 26 FliG units and each stator has 4 copies of MotA and 2 copies of MotB, forming two proton transmembrane ion channels [20]. Both the C-Ring and MotA/MotB complexes has a diameter of around 30 nm and are thought to closely couple [21]. Charge groups of MotA interact with charge groups in the C-terminal domain of FliG [22], [23]. Proton translocation in the MotA/MotB complex causes conformation changes in the cytoplasmic residues of MotA which interacts with FliG to deliver the mechanical force of rotation [24]. Quantitatively the rotational speed is linearly associated with the PMF [25].

It is known that the flagellar motor's duty ratio, the fraction of time that a stator is attached to rotors, is close to 1. This indicates that at any given time a stator is interacted with one of the FliG protein on the C-Ring and the rotor rotates by discrete steps at micro-level [26], driven by stators. As the exact molecular-level mechanism of the torque generation is still lacking, researchers have proposed many models to explain the observed experiment al

results [27], [28]. Notably the framework proposed along the works of [16], [29]–[31] provides a general explanation without referring to the energy-transduction details (Figure 2.3). It was proposed that, each stator has two force generating subunits (the light and dark part in Figure 2.3 A), one of which is linked with a FliG protein on the rotor. As a proton passed through a stator, the stator changes its configuration and interact with the rotor in a hand-over-hand fashion, in which one hand releases its attachment of a FliG protein and another establishes a new interaction with the adjacent FliG protein (Figure 2.3 B). The relative angular coordinates between the stator and rotor follow a concave-shaped energy landscape and the "hand-switching" is caused by the low energy configuration (Figure 2.3 C). When protons pass through the stators, the PMF is reflected in the shifting of energy landscapes (Figure 2.3 C, indicated by the dashed arrow) which causes the stator to "switch hands" continuously.

At low Reynolds number, all the forces acting on the rotor are balanced. At any moment, the rotor experiences forces from the sum of the energy potential, forces from the resistance load on the flagellum and a stochastic Brownian force. Thus one can model the rotor system in a Langevin Equation [29]:

$$\xi_R = -\frac{\partial}{\partial\theta}\left(\sum_{i=1}^{N} V\left(\theta^R - \theta_i^S\right)\right) - F\left(\theta - \theta^L\right) + \sqrt{2k_B T \xi_R}\cdot\eta(t) \qquad (2.15)$$

where on the left hand side, ξ_R is the drag coefficients for the rotor in the fluid. The first term on the right hand side represents the force on the rotor caused by the change of the energy potential from the relative configurations between the rotor and each stator. Each stator has two stable configurations interacting with the rotor, illustrated in (Figure 2.3 A) as two spring hands. $N = 26$ is the number of stators in the motor, V is the energy potential between the rotor and a stator, which is a function dependent on the relative angle $\Delta\theta = \left(\theta^R - \theta_i^S\right)$ between the reference angle θ_i^S of a stator $i (i \le N)$ and that of the rotor θ^R. For every hand-switching transition (Figure 2.3 B), θ_i^S increase by $\delta_0 = 2\pi/2N$. The second term on the right hand side represents the influence of the force from the motor to the motion of the flagellar that we can observe. F is a nonlinear elastic term transducing the rotation from the motor to the load on the flagellum, through the flexible hook structure. θ^R is a referencing angular coordinate on the flagellum. The last term of Eqn. (2.15) represents stochastic forces on rotor. η is an independent white noise term with unity intensity, while k_B is the Boltzmann constant and T is the absolute temperature. The rotation of the rotor is the combined effort of the discrete hand-switching of each stator: the probability of a single stator shifting its angle is $\Pr\left(\theta_i^S \to \theta_i^S + \delta_0\right) = f\left(\theta^R - \theta_i^S\right)$. f must be a quasi-monotonic function (Figure 2.1 E) such that if $\left(\theta^R - \theta_i^S\right) > 0$ (which means the stator is lagging behind the rotor and is being pulled, increasing its stepping probability), f is higher. If $\left(\theta^R - \theta_i^S\right) < 0$ (which means that the stator is

moving ahead of the rotor and is being dragged by the rotor, decreasing its stepping probability), f is lower. For simplicity one can use $f\left(\theta^R-\theta_i^S\right)=k\left(\theta^R-\theta_i^S\right)\Delta t$, $k=12000$ s^{-1} if $\left(\theta^R-\theta_i^S\right)<0$ and $k=24000$ s^{-1} if $\left(\theta^R-\theta_i^S\right)>0$. Each stator steps according to this probability relationship $\Pr$ and updates the energy potential V in Eqn. (2.15). The model explained the motor dynamics by two characteristic time scales: the moving time scale of the rotor through mechanical forces, and the waiting time scale of the stators through chemical transition. The crossover the two time scales explained the two regimes observed in the torque-speed curve [16]. In addition, it predicted a speed variation from the motor, which is dependent on the number of stators and the load.

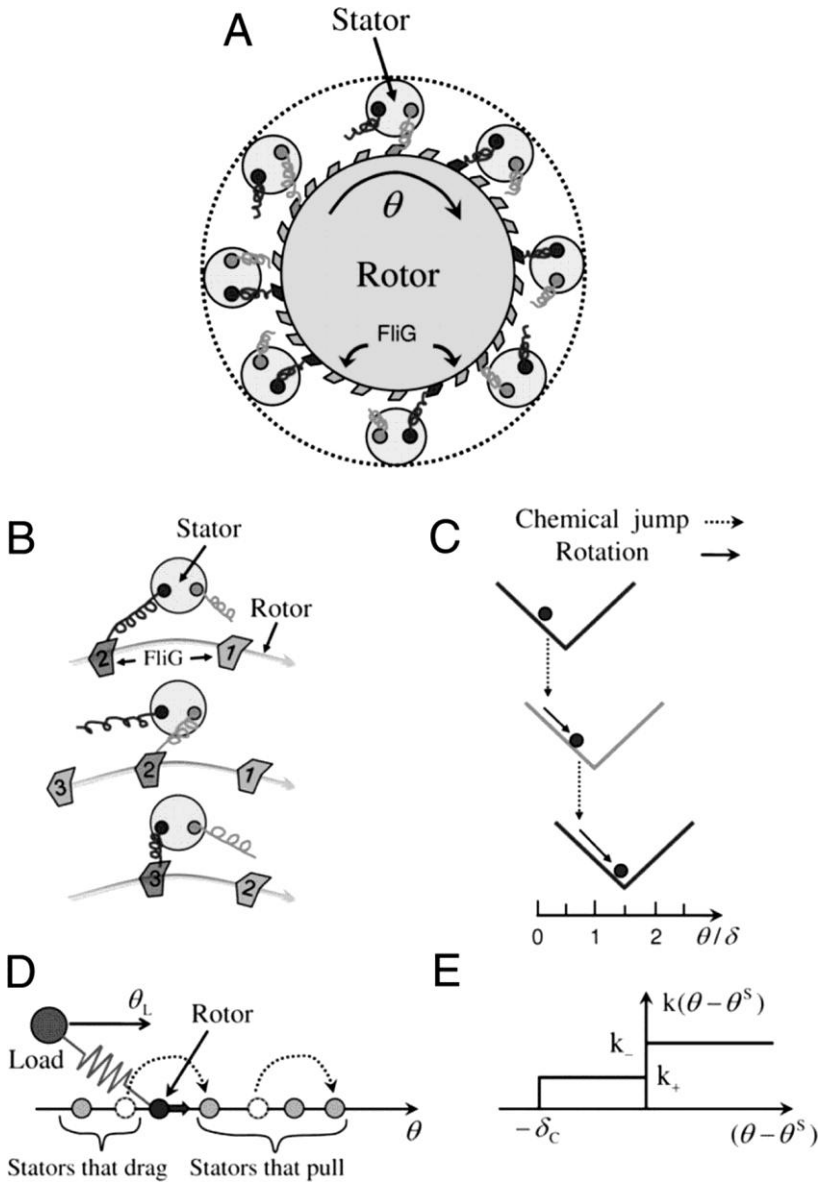

Figure 2.3 The Meacci-Tu stepping model to explain flagellar motor rotation

(A) A schematic illustration of the rotor-stator arrangement from a top view. The rotor has 26 units of FliG. Multiple stators surround the rotor, each with two subunits (dark and light springs). (B) A three-step sequence of the hand-over-hand interaction between the FliG proteins and the two subunits of a stator. (C) The same sequence shown in the energy landscape. Chemical jump indicates the shift of the PMF energy landscape and the rotation is discrete with a step size of δ_0. (D) The schematic view of the relative angular coordinates of the rotor and stators. A rotor is either pulled by the stators rotating ahead of it or dragged by stators rotating behind it. (E) The jumping

probability of a stator with respect to its relative angular difference to the rotor. The rate is higher at k_- if $\left(\theta^R - \theta_i^S\right) > 0$ (rotor pulling) and lower k_+ if $\left(\theta^R - \theta_i^S\right) < 0$. δ_c is a cutting off value to prevent runaway stators. The figure is taken from [29].

2.2.3 How does the motor switch rotation directions?

Most of the bacterial molecular motors are reversible, being able to rotate in both counter-clockwise (CCW) and clockwise directions (CW) [32]. This involves the direction switch of the motor, which lasts only 1ms [33]. FliG, FliM and FliN are all responsible for the direction switch of the motor [34]. The chemotactic signaling protein CheY-P (phosphorylated CheY) in the cytoplasm binds to FliM and FliN [35], [36] and induces a conformational change of the FliG protein [37], [38], which switches the rotor's rotational direction through interactions with stators. In wild-type condition, the FliG proteins are more stable in the CCW state than in the CW state and subsequently the motor rotates in a default CCW direction [39].

The binding of CheY-P to the motor has a cooperative effect on the switching. Usually a cooperative binding (between a ligand and a receptor) can be expressed in Hill's equation:

$$\theta = \frac{1}{\left(K_{1/2}/[L]\right)^n + 1} \tag{2.16}$$

where θ is the occupancy fraction of CheY-P ligand binding, $K_{1/2}$ is the ligand concentration at which CW bias is 0.5, $[L]$ is the free ligand (unbounded) concentration, and n is the Hill's coefficient indicating the level of allostery of ligand binding effect, where a coefficient of 1 indicates completely independent binding.

In the rotary motor, similarly, the effect of CheY-P binding on the motor switching can be expressed in the format of Hill's function where θ is the CW bias and $[L]$ is the concentration of CheY-P. It has a Hill's coefficient as high as 10.3 [7]; however the binding of CheY-P to the protein FliM is much less cooperative [40], [41]. This indicates a high cooperativity during the switch process. The cooperativity of the conformational change can be explained by a stochastic approach [42], which was experimentally supported and theoretically advanced as the conformational spread model [43], [44] (Figure 2.4). In the most simplified form, the conformational spread model states that the binding of CheY-P to FliG induces a conformational change of the protein that favors another rotational direction. This conformation of the FliG protein will spread to its neighbors and eventually the whole ring to stabilize the new rotation direction.

Specifically, the model assumes that the C-Ring consists of 34 protomers, each contains 1 FliG, 1 FliM and 4 FliN subunits. Each protomer may be bounded or unbounded by CheY-P, represented by "*B*" and "*b*". In addition each protomer is either in a conformation that corresponds to CCW rotation or a conformation that corresponds to CW rotation, represented by

active "*A*" and inactive "*a*" respectively. The combination of these gives 4 possible states: *Ab*, *AB*, *aB*, and *ab*, between which transitions are possible. *AB* and *ab* have lower free energy so these conformations are more stable (Figure 2.4 B). Without CheY-P binding, the protomer favors a CCW conformation because the free energy E(*ab*) < E(*Ab*). The CheY-P binding shifts the free energy landscape and E(*aB*) > E(*AB*), subsequently the protomer favors a CW conformation. The binding rate of CheY-P is dependent on the concentration of CheY-P in the cytoplasm, and once bound the conformational change of the protomer is a stochastic process regulated by the free energy level. Once a protomer flips to a new conformation, it will affect its neighboring protomers. There is a free-energy penalty E_J from the adjacent protomers if they are not in the same conformation as the one in the middle: Free energy is lowered by E_J for any like pair compared to any unlike pair (Figure 2.4 C), hence a protomer changing its conformation results in its neighbors adopting a similar conformation, and that conformation "spreads" further to the next neighbors. To summarize, for majority of the time the motor rotates in a coherent state (either CW or CCW). The rotor switch stems from a stochastic event of a protomer changes its conformation due to CheY-P binding/unbinding, followed by the conformational spread of the domain in random-walk fashion, until it either encompass the whole ring or collapses back to the original coherent state (Figure 2.4 D). Monte Carlo simulations based on this model fit well with experiment data, especially in explaining the dynamics of the observed "incomplete" switches due to the collapse-back of the conformational spread [43].

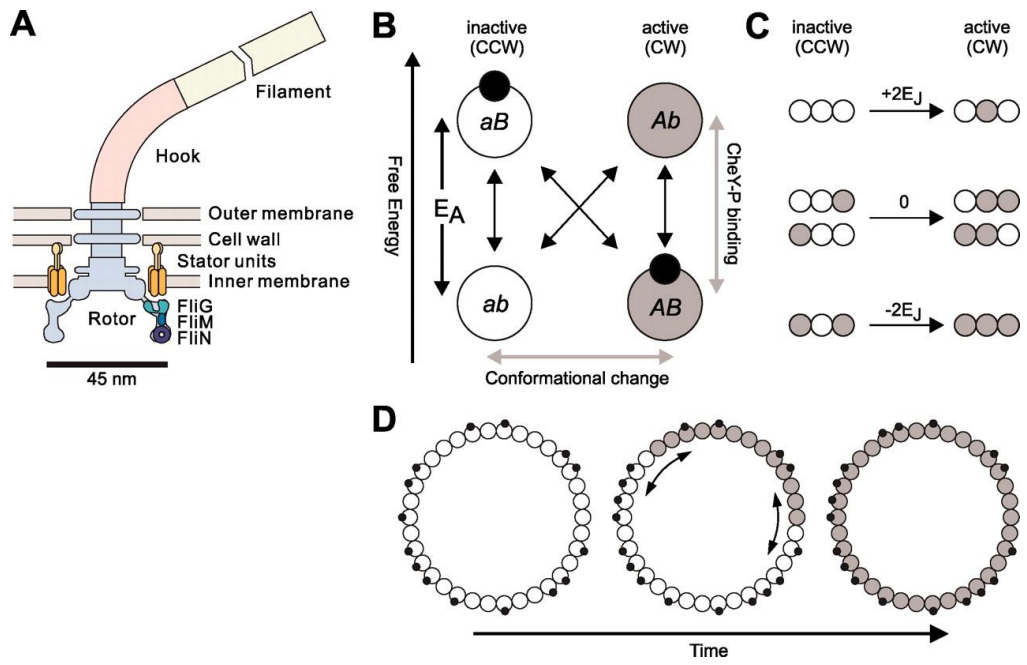

Figure 2.4 The conformational spread model of the motor switch

(A) A schematic figure of the structure of the *E. coli* flagellar motor. (B) Assume the C-Ring has 34 protomers, each contain 1 FliG, 1 FliM and 4 FliN subunits. Each protomer has a single binding site of CheY-P, and results in a state of either binding (*B*) or unbinding (*b*) (the black dot). Also each protomer has two conformations: active (*A*, corresponding to CW rotation) or inactive (*a*, CCW rotation). The permutation of these gives four possible states, which are demonstrated in this free-energy diagram. E_A is the free-energy difference between the favored and unfavored states and for simplicity it is assumed to the same between aB/ab and Ab/AB (the black dot). (C) Possible interactions between the adjacent protomers. Free energy is lowered by E_J for any pair of the same conformation compared to any dissimilar pair. (D) Above a critical energy value E_J the motor spends most of the time in a coherent state, with occasional stochastic switch between CCW and CW states. A switch happens from a single nucleation event of CheY binding or unbinding, followed by a conformational spread of in a random-walk fashion, until it either encompasses the whole ring (results in a switch) or collapses back to the original coherent state (results in no switch). The figure is taken from [43]

2.3 Motility and chemotaxis of *E. coli*

2.3.1 The run-and-tumble motion of *E. coli*

Berg and colleagues laid the ground work in establishing the *E. coli*'s "run-and-tumble" model [2], [45]–[47]. The CCW and CW rotation of the molecular motor in E .coli lead to two distinctive motile patterns: run and tumble. When all the molecular motor rotate in CCW state, they are entangled together in a bundle and act like one single filament, propelling the bacterium forward in a run; when one or more molecular motor switch the rotation to CW state, the bundle separates and the bacterium stops advancing and tumble at the same place (Figure 2.5 A) before running again. During tumbling, a bacterium usually changes its orientation to an almost random direction. Therefore the swimming direction after the tumbling is different from that of the previous trajectory.

An *E. coli* cell typically runs along its body major axis for about a second at a speed of ≈20 μm/s before it tumbles for ≈0.1s and starts run again. Run intervals and tumble intervals follow exponential distributions [47]. While average tumbling intervals are steady in distribution among individuals with a mean of 0.1s, run intervals, although following an exponential distribution for a single cell, have means that vary among individuals [48].

Chemotaxis is defined as the movement of an organism in response to an external chemical stimulus. For bacteria, that means they need to sense the environment and swimming towards the highest concentration of their favored

molecules (such as glucose or amino acids). During chemotaxis, the chemical receptor clusters located on the membrane of a bacterium sense molecules of interest which the cell uses to control (details explained in the next section) the rotation direction of the flagellar motors to modify its movement. *E. coli* changes its probability of tumbling in response to the chemoattractant gradient. When the bacterium is moving up a chemoattractant gradient, the tumbling frequency is reduced; therefore the bacterium runs for longer distance without changing its moving direction from tumbling. When the bacterium is moving down the chemoattractant gradient, the tumbling frequency is increased; therefore the bacterium re-orients more frequently until it is in a direction that it can move up the gradient again. As a result of this strategy, *E. coli* cells are able to climb up the chemoattractant gradient and become enriched in regions of high attractant concentrations.

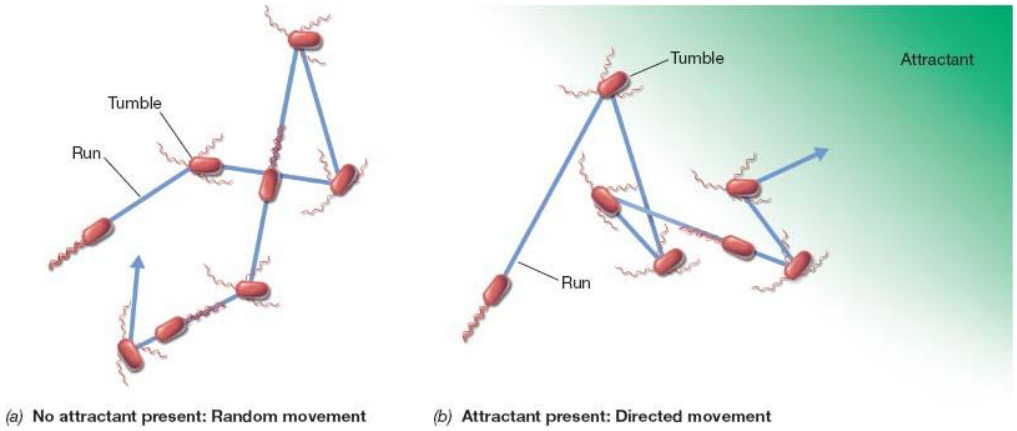

Figure 2.5 Schematic illustration of the run-and-tumble movement of *E. coli*

(A) *E. coli*'s two types of basic movement: run and tumble. When it runs, it advances in a relative straight trajectory (yellow lines); when it tumbles, it jiggles at the same place for a while (blue circles) and reorients its direction

for the next run. (B) Run-and-tumble in chemotaxis: the cell tumbles less if it is moving up the chemoattractant gradient and tumbles more in the opposite situation. Eventually, the cell moves towards regions with higher concentrations of chemoattractant. The figure is taken from [49].

2.3.2 The molecular basis of *E. coli*'s chemotaxis

In *E. coli*, in response to decreased attractant ligands binding to chemoreceptors clustered (MCPs) on the cell surface, the signaling protein CheA is activated for auto-phosphorylation and becomes CheA-P (Figure 2.6). CheA-P in turn phosphorylates two response regulator proteins, CheY and CheB [50]. The phosphorylated CheY, CheY-P, is released from the cluster and diffuses to the flagellar motor, where it binds to the motor proteins, FliM and FliN, causing a conformational change of the flagellar motor ring [37], [43]. This results in a switch of the rotational direction of the motor ring from CCW to CW [36], [51]. The protein CheZ acts antagonistically to CheY-P and de-phosphorylates it. CheA, CheY and CheZ serve as the proteins in the signaling pathway for immediate response to the external stimulus. At the same time, the phosphorylated signal protein CheB, CheB-P, works antagonistically to CheR, which increases the ability of the chemoreceptors to activate CheA [50]. The CheB/CheR system serves as a primitive memory to reset the signaling sensitivity to the time-averaged ligand concentration in the recent past.

As a result, if a bacterium is moving in the favorable direction (towards higher concentration of chemoattractant), the network results in a lower CheY-P concentration, which causes the motors spin CCW longer than

they would otherwise. The methylation and de- methylation of the MCPs react slower and lead to the adaptation which resets the response back to the base-level. There have been many studies based on this basic mechanism to further the understanding of the sensing characteristics, controlling network and chemotactic-search strategy, both experimental and mathematical [25], [52]–[55].

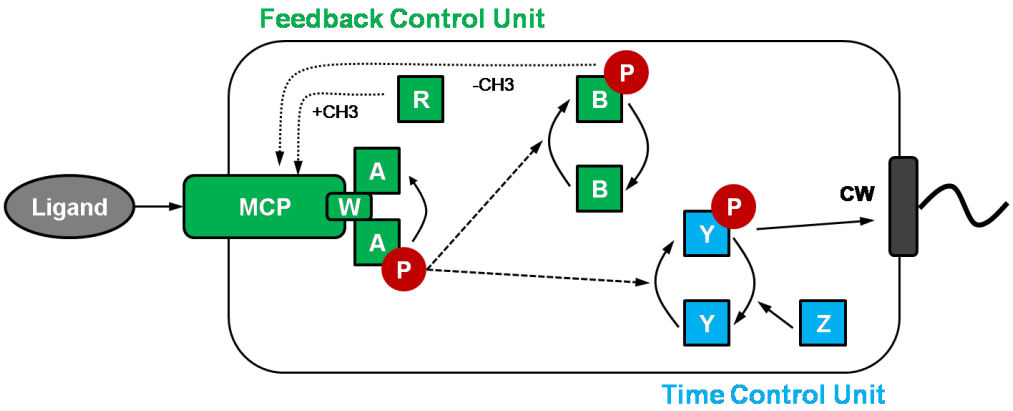

Figure 2.6 Illustration of the *E. coli* chemotaxis network

Components in green and blue are proteins involved in the chemotactic pathway of *E. coli*. MCP is the receptor complex, CheW, CheA, CheY, CheZ, CheR and CheB are proteins coded by the *che* gene family. Red circle labeled with a 'P' represents phosphate group. CheA is an auto-phosphorylating protein that transfers its phosphate group to two possible targets – CheB or CheY. CheY-P binds to the molecular motor and increases the probability of CW rotation and CheZ constuitively de-phosphorylate CheY-P to CheY. CheB-P reduces the methylation level of MCP against protein CheR. The ligand binding to the MCP suppresses auto-phosphorylation of CheA protein, leading to less CheY-P and CheB-P. This results in a higher probability of CCW rotation and accumulated methylation of MCP, which enhances the auto-phosphorylation of CheA proteins. Figure is adapted from [50]

2.4 Motility and chemotaxis in monotrichous bacteria

In contrast to peritrichous bacteria such as *E. coli*, the motility and chemotaxis of monotrichous bacteria is less established. *E. coli* takes advantage of an asymmetric outcome (run versus tumble) from the symmetric rotations (CCW versus CW) of the motors. However in monotrichous bacteria, there is no such asymmetry to exploit, as the CCW and CW rotations of the motor both lead to symmetric forward and backward movements, respectively. In order for monotrichous bacteria to undergo chemotaxis, there has to be some alternative mechanisms other than *E. coli*'s "run-and-tumble" to generate biased movement.

Early studies implied that the monotrichous bacteria *Pseudomonas citronellolis* change moving direction by a short reversal of the flagellar rotation [56], but did not fully examine the details of this response on the molecular level and the adaptation in the sensing-feedback loop. More importantly, questions such as how that mechanism of monotrichous motility forms the search strategy in chemotaxis and how the mechanism is involved in the group behavior of some of the pathogenic bacteria require further investigation.

Some models for other monotrichous bacteria motility have been proposed in recent years, including a three step "run-flick-reverse" model of the monotrichous marine bacterium *Vibrio alginolyticus* [57], [58] and "run-and-stop" of monotrichous *Rhodobacter sphaeroides* [59], [60]. The flick

motion in the “run-flick-reverse” in *Vibrio alginolyticus* was further attributed to the instability of the flagellar buckling due to higher compression stress at fast forward swimming [61]. Such discovery shed light on how the monotrichous bacteria, seemingly doomed by its one dimensional physical limitation, are able to generate additional degrees of freedom and explore the three dimensional space more effectively. However, as the buckling is a passive physical process resulted from forward swimming, the controlling mechanism for it during locomotion especially in chemotaxis is still lacking.

Similarly, in *P. aeruginosa*, the mechanism of motility and chemotaxis is less clear. Previous genetic studies have shown that *P. aeruginosa* possesses two sets of flagellar stators compared with one set for *E. coli* [62]. In addition, the chemosensory system of *P. aeruginosa* is more complex than *E. coli* or other species: For example, while *E. coli* has only one gene cluster with 5 methyl-accepting chemotaxis proteins (MCPs) and 6 chemotaxis (*che*) genes [63], *P. aeruginosa* has 4 gene clusters involved in chemotaxis, with 26 methyl-accepting chemotaxis proteins (MCPs) and 20 chemotaxis (*che*) genes [64]. Among these gene sets, one (PA408-PA417) is involved in the pili-mediated twitching motility [65], [66], one is believed to control biofilm formation [67], [68], and the remaining two sets, *che* and *che2*, are similar to their *E. coli* counterparts and regulate flagella-mediate chemotaxis [69]. Besides chemoreceptors located on the cell surface, *P. aeruginosa* also possesses cytoplasmic chemoreceptors [70]. It is still unclear how this complex set of proteins function to regulate chemotaxis.

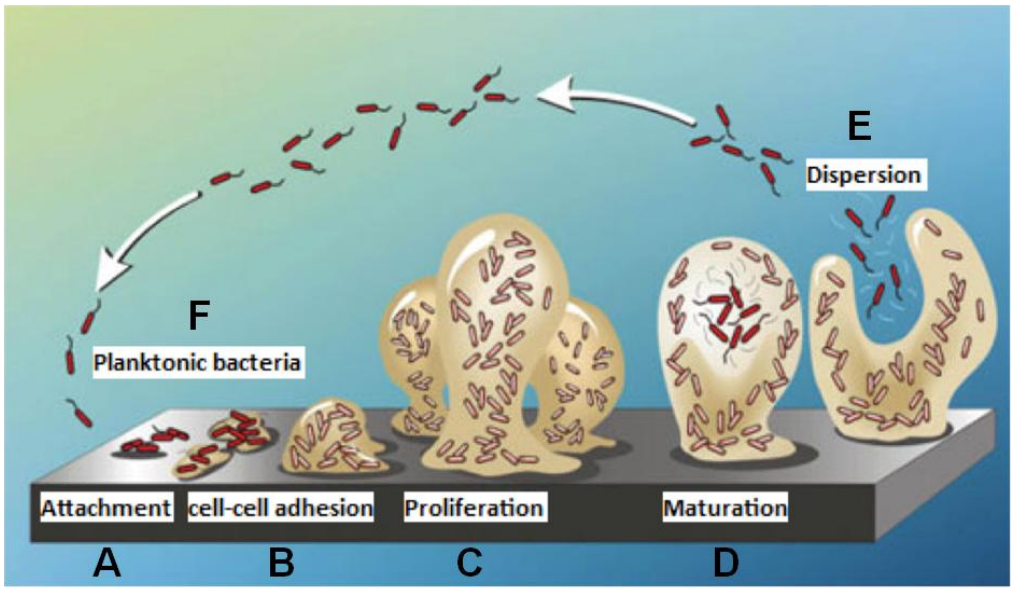

Figure 2.7 Schematic illustration of the life cycle of a biofilm

(A) Reversible attachment. (B) Irreversible attachment. (C) Maturation I. (D) Maturation II (E) Dispersion of planktonic bacteria. (F) Planktonic bacteria forming attachments to a surface. The figure is taken from MicrobeWiki.

2.5 Motility and chemotaxis of *P. aeruginosa* in biofilms formation

One of the motivations of studying *P. aeruginosa* is its strong ability to form biofilms. It can survive in both normal and hypoxic atmospheres, and because of that, colonize many environments which may include soil, water, human skin, industrial structures, hospitals and clinics, in the form of biofilms. A biofilm is an aggregate of microorganisms in which cells adhere to each other on a surface. Cells are usually embedded within a self-produced matrix of extracellular polymeric substance (EPS), which allows them to form complex three dimensional structures.

A biofilm has several stages in its live cycle development (Figure 2.7) [71]. The bacteria form initial attachments to a surface and start to produce slimy EPS. EPS allows the biofilm to grow as a community with bacteria proliferating inside to form complex three dimensional structures. This process can take anywhere from within a few hours to a few days. When the biofilm reaches maturation, cells secrete enzymes that degrade the EPS and disperse cells from the biofilm colony to the environment again. The cells released to the aqueous system are called planktonic cells. Their flagella-mediated motility and chemotaxis play critical roles in biofilm spreading and colonization of new surfaces [72], [73].

2.6 Established experimental techniques in the study of bacterial motility and chemotaxis

In the studies of bacterial motility and chemotaxis, methods such as the capillary [74] and agar plate [75] assays have been used to obtain a qualitative and macroscopic view. In the capillary assay, a capillary containing chemoattractant is inserted into a suspension of motile bacteria and the accumulation of the bacteria to the mouth and interior of the capillary is measured. In the agar plate assay, agar plates with bacteria colonies are incubated and the expansion of the colonies is measured as an indicator of motility.

To have a more quantitative and microscopic view, various groups have established systems to track either a single bacterium [45] or a group of

bacteria [76] in three-dimensional space in response to chemoattractants during swimming. The first method uses a mechanical feed-back system to move the stage of the microscope so that the bacterium of interest always stays in the focal plane. The second method measures the sizes of aberration rings of the images taken from the optical microscope to gauge the distance of bacteria to the focal plane. However, the first method requires a sophisticated mechanical control of the microscopic system and can only track one bacterium at a time; while the second method suffers from short depth in the tracking space and lack spatial resolution. In addition, both methods have difficulties in the precise control of the chemoattractants in the micro-environment surrounding a bacterium as it moves freely in the three-dimensional space.

Alternatively, as the movement of a bacterium is caused by the rotation of the flagellum, one can also study that rotation to gain insights into bacterial motility and chemotaxis (Figure 2.8). To do this, one can either fix the cell body to a surface and observe the rotation of the flagellum by tracking a bead attached to it [77], [78] or fix the flagellum to a surface and observe the rotation of the cell body [32]. The latter method, known as the tethering assay, is widely used to study the bacterial response to stimuli due to its easy control of the micro-environment and ability to monitor a large number of bacteria at a time. It has been the key technique to quantitatively reveal the fundamental properties and mechanisms of *E. coli* chemotaxis by measuring tumbling frequency, run length and kinetic response [6], [46], [47].

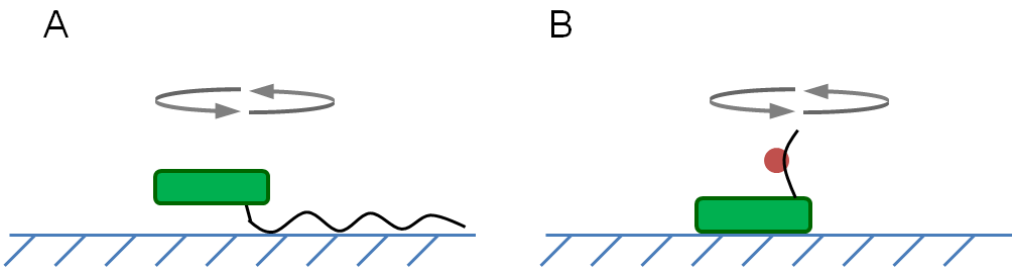

Figure 2.8 Schematic illustration of the tethering and bead tracking experiment

(A) The tethering experiment. The sheared flagellum of the bacteria is tethered to a surface coated with flagellin antibody. The rotation of the flagellar motor is then translated to the rotation of the cell body (greed rod) and can be observed under the microscope. (B) The bead tracking experiment. The cell body (green rod) is attached to a surface and a bead (red dot) coated with flagellin antibody is attached to the sheared flagellum. The rotation of the flagellar motor is translated into the rotation of the bead which can be observed under the microscope..

While the tethering assay works well in the peritrichous bacteria such as *E. coli*, it results in more unstable measurements in monotrichous bacteria such as *P. aeruginosa* due to the location of the flagellum (see Section 3.3.2). Thus there is a need for a more reliable experimental and computational analysis system which will allow more accurate measurements of the tethered bacteria and a good control of the micro-environment.

2.7 Purpose of the study

In view of the aforementioned issues, further research on both experiments and computational modeling of the motility and chemotaxis of

monotrichous bacteria is imperative. In particular, this thesis aims to address the following aspects:

► Develop a more stable and reliable experimental platform to study the motor property and chemotaxis response of monotrichous bacteria such as *P. aeruginosa,*

► Understand the molecular motor properties of *P. aeruginosa* and the motor's response to chemoattractant gradients in the micro-environment,

► Understand the searching strategies of *P. aeruginosa*'s in normal conditions/chemotaxis.

These studies should result in a more reliable system that will allow other microbiologists to study the motility and chemotaxis particularly for monotrichous bacteria such as *P. aeruginosa*. We will also propose new models of motility and chemotaxis in monotrichous bacteria which will help in understanding the movement and population behavior of *P. aeruginosa*.

More specifically, this thesis presents two pieces of interrelated studies. In Chapter 3, we will present a new computational tool (BTAP) that addresses the rotational instability of the tethered monotrichous bacteria and make corrections. The tool eases the image and data processing with a higher precision. By using BTAP, a novel pause phase of the flagellar motor was identified, and we discovered the "run-reverse-turn" mechanism for *P. aeruginosa*. In Chapter4, we will use BTAP to study the chemotactic response of *P. aeruginosa*. Its responses reveal a "rectified run-and-reverse" strategy for

its chemotaxis, which may also be plausible for other monotrichous bacteria. Taken together, these two chapters advanced our understanding of the motility and chemotaxis mechanism of monotrichous bacteria, in particular *P. aeruginosa* which is a threatening pathogen presented widely in the environment.

3 BACTERIAL TETHERING ANALYSIS REVEALS A "RUN-REVERSE-TURN" MECHANISM FOR *PSEUDOMONAS* SPECIES MOTILITY

Chapter 3, in most part, is a reprint of [79] as it appeared in Applied Environmental Microbiology 2013. Appl. Environ. Microbiol. 2013, 79(15):4734. DOI:10.1128/AEM.01027-13. The dissertation author was the co-first author. (C.Q., C.W and K.-H.C designed the study, C.W. performed the experiments, C.Q. developed the BTAP program and conducted the analysis, C.Q., C.W. and K.-H.C wrote the manuscript)

3.1 Introduction

In recent years, some models have been elucidated for the motility of monotrichous bacteria, including the three-step "run-reverse-flick" chemotactic response for the sodium-driven, monotrichous *Vibrio alginolyticus* [57], [80] and that of varying "run-and-stop" frequencies in monotrichous *Rhodobacter sphaeroides* which has a motor rotates in only one direction [60], [81]. The diversity of flagellar motor structures [82], flagellar arrangements, and genes involved in chemotactic [63], across the bacterial kingdom likely account for the presence of these different systems.

However, in the case of *Pseudomonas* spp., mechanisms of motility and chemotaxis still remain unclear. Current evidence suggests that the

chemosensory system and flagellar organelle arrangement in the strains belonging to this genus are more complex that those of other bacterial species. For example, *P. aeruginosa* has five gene clusters involved in chemotaxis, with 26 methyl-accepting chemotaxis proteins (MCPs) and 20 chemotaxis (*che*) genes, compared to *E. coli*, which has one gene cluster, with four MCPs and six *che* genes [83]. Additionally, there are two sets of flagellar stators in *Pseudomonas* spp. compared to one set for *E. coli* and *Salmonella entetrica* serovar Typhimurium [62], [84]. As *Pseudomonas* spp. are polar-flagellated, they are likely to possesses a "run-and-reverse" trajectory [56] rather than the typical "run-and-tumble" trajectory. Since both the *Pseudomonas* flagellar motor and chemosensory system present some unique features, it would therefore be interesting to study the motor dynamics of *Pseudomonas* spp.. Notably, many members of this genus play significant roles in their environment, such as in the degradation of organic hydrocarbons, in plant growth promotion, and in nitrogen fixation. Other members, however, are pathogenic to humans, insects, or plants [85]. Therefore, elucidating the motility and chemotactic mechanisms for *Pseudomonas* spp. can be beneficial in many studies extending to bioremediation and host-pathogen interactions. Additionally, across *Pseudomonas* spp., different species also exhibit dissimilar flagellar arrangement. In the plant growth promoting rhizobium (PGPR) strain, *P. putida*, the flagellum is arranged in a polar multitrichous manner [86], whereas in the human pathogen, *P. aeruginosa*, the flagellum is polar monotrichous [87]. Hence, it would also be interesting to elucidate if

there are differences in the role of each flagellum in contributing to *Pseudomonas* motility.

In order to study bacterial chemotaxis, various methods such as the capillary [74] and agar plate [75] assays have been previously developed to study the population movement in a macroscopic view. Tracking of a single bacterium [45] or a group of bacteria [76] in a three-dimensional environment has been used to study the response of a single bacterium to chemoattractants during swimming. Since the flagellar motor is directly coupled with this chemotactic response, one can study the rotation of the motor by fixing the cell body to a surface so as to observe the rotation of a bead attached to the flagella [77], [78]. Alternatively, this can also be achieved by fixing (tethering) the flagella to a surface to observe the rotation of the cell body [32]. The latter approach, also known as the cell-tethering method, is most widely used to study the response to stimuli of a large number of bacteria.

In this study, we have developed a program, which we name the Bacterial Tethering Analysis Program (BTAP) that can track large numbers of tethered cells and extract accurate and reliable rotation data. Our program dynamically adjusts the centers of the cell's rotational trajectories and applies piecewise linear approximation to the accumulated rotation curve to reduce noise and separate the motion of bacteria into different phases. This is particularly useful for polar-flagellated bacteria, such as *Pseudomonas* spp., as they tend to give rise to unstable rotation trajectories [88]. Using our program, we were therefore able to elucidate the flagellar motor properties of two

Pseudomonas strains, KT2440 and PA01, belonging to *P. putida* and *P. aeruginosa*, respectively. We show that unlike *E. coli*, cells belonging to both *Pseudomonas* strains spend an equal amount of time rotating in the counterclockwise (CCW) and clockwise (CW) directions. Interestingly, the *Pseudomonas* cells also have an additional pause phase that constitutes nearly 10 % of the total observed time, and we propose that this pause phase allows the cells to vary their turn angle, adopting a "run-reverse-turn" trajectory. In addition, BTAP analysis of a *cheY* chemotaxis mutant in *P. aeruginosa* also revealed that *Pseudomonas* cells vary their run-lengths, pause frequencies, and pause durations, as part of their chemotactic response. By analyzing trajectories of free-swimming cells, we established a role for the pauses, where *Pseudomonas* cells vary their pause duration to affect different turn angle sizes.

3.2 Materials & Methods

3.2.1 Growth condition

Pseudomonas aeruginosa PA01 wild-type, *cheY* [89], and *Escherichia coli* MG1655 cells from single colonies were separately cultured overnight in 10 ml Luria-Bertani (LB) broth at 37 ℃, 250 rpm. Cultures were diluted to $O.D._{600}$ = 0.1 using LB broth and grown at 37 ℃, 250 rpm until the late-exponential growth phase was reached. For *P. putida* KT2440, cultures were grown at 30 ℃, 250 rpm. Cell cultures were then diluted 1:10 prior to imaging using video microscopy.

3.2.2 Cell tethering and video capture

For cell tethering assays, standard methods [32] were adapted as follows: glass coverslips were pre-coated with flagellar antibodies prior to use and cell chambers (2.0 cm × 1.0 cm × 150 μm) were created using three layers of double sided tape between the microscope slide and coverslips. Flagella were sheared off by passing the bacterial cells through a 34-gauge blunt end needle for four times. Cells were loaded into the cell chamber for few minutes and non-tethered cells were rinsed away using LB broth. Cells were visualized using an inverted microscope (Nikon TE2000U) under 100X objective. Videos of tethered bacteria were taken at 120 fps for 1-5 mins using a CMOS camera (Thorlabs DCC1645). Following the convention, cells are considered to be rotating CW/CCW when viewed from the medium they are tethered in [48]. In the experiment of multitrichous *P. putida*, to eliminate the case, where more than one filaments are tethered and where the filaments do not rotate in sync, only cells that exhibit clear rotations were selected for analyses.

Free swimming *P. aeruginosa* cells, with their intact flagellum, were loaded in cell chambers and observed in the middle of the chamber depth (away from the coverslip surface or microscope slide surface). Cells were visualized under 40X objective and videos of bacteria were taken at 25 fps. Bacterial swimming trajectories in 2D were captured using Image Pro Plus 6.3 (Media Cybernetics, Rockville, MD, USA) and images with cell outlines were obtained using ImageJ (NIH, Bethesda, MD, USA).

3.2.3 Pause detection for 2D swimming trajectories

The instantaneous speed for free-swimming bacteria was calculated from the 2D trajectories frame by frame. Trajectories with frames fewer than 25 were discarded. A pause was identified when $N(N>3)$ consecutive instantaneous speed data points that were below 5 μm/s appeared. The moving direction of a bacterium at certain time was defined as the vector connecting its current coordinates to its next coordinates. Accordingly, the change of angle was the angle difference between two such directions which ranged between $-\pi$ and π. Additionally, as we are observing from the microscope, only cells moving in the plane horizontally to the microscope's focal plane (the x-y plane) will be captured accurately. The larger the movement in z-axis (i.e. the moving direction more close to the z-axis) of a cell, the larger the error in observed angle as the angle is projected on the x-y plane. Moreover, a cell with z-axis movement with quickly swims out of the focal plane, rendering to a very short trajectory segment being recorded, most likely without any turning. To ensure that the cells swimming in the z-axis direction did not affect the angle size tracked, only cells that were in focus, and thus swimming within the x-y focal plane, were selected for analysis.

3.2.4 Image extraction and data preprocessing for tethered cells

For image processing, movies of single, tethered cells were converted to gray scale and their contrasts were adjusted (saturated pixels=0.4, histogram stack) using ImageJ (NIH, Bethesda, MD, USA). The image of the rotating cell body was binarized to be isolated from the background for each frame in

the video. Next, using the "Set Measurements" function in ImageJ, the coordinates of the center of mass of the rotating cell body were measured from the binarized image stack, and imported into MATLAB (MathWorks, Natick, MA) for BTAP analyses.

3.3 Results

3.3.1 Signal processing in BTAP

BTAP is a code package in Matlab. BTAP has two essential components to reduce the noise from the video and separate the motion of motor into phases. The first component of BTAP is to adjust for variations in the rotational axes of the moving trajectories of tethered cell bodies. For *Pseudomonas* spp., we noticed that the rotation of the tethered cell was not stable: i.e., the rotational trajectories of the cell bodies did not collapse onto a single circle but instead frequently collapsed as "clouds" (Figure 3.3 B) or multiple partially overlapped circles (inset, Figure 3.4 D). As this instability was not observed in tethered *E. coli* cells (Figure 3.2 B), it is likely due to the inherent location of the Pseudomonas flagellum at the cell pole, resulting in a rotating cell body that is able to vary its axis of rotation (Figure 3.3 F). It was, therefore, critical to adjust the axes of the rotational trajectories. If the instantaneous rotational speeds were translated directly from the positions of the cell body measured, and the rotational axes were not adjusted, large biases would be observed from data. Therefore, to perform this adjustment, we first denoted the centroid coordinates of each tethered cell at each video frame i

as (x_i, y_i). To remove the impact of a changing axis on the rotational trajectory of the tethered cell, the location of the rotational axis (a_i, b_i) was identified. This was performed by fitting a circle to the trajectory as follow: a circle was fitted using the adjacent data points in the most recent 0.25 s of trajectories (30 points in our video samples taken at a frame rate of 120 fps) with the modified least squared error method, which minimizes the sum of squared errors (SSE):

$$\mathrm{SSE}(a,b,r) = \sum_{i=n+15}^{i=n-15} \left(r^2 - (x_i - a)^2 - (y_i - b)^2 \right)^2 \qquad (3.1)$$

Here, x_i and y_i are coordinates of the cell body centroid at frame i, and a, b, r are the centroid coordinates and radius of the best fitting circle respectively. Next, the corresponding data point (x_i, y_i) was re-adjusted as $(x_i - \mathrm{a}, y_i - b)$ (Figure 3.1).

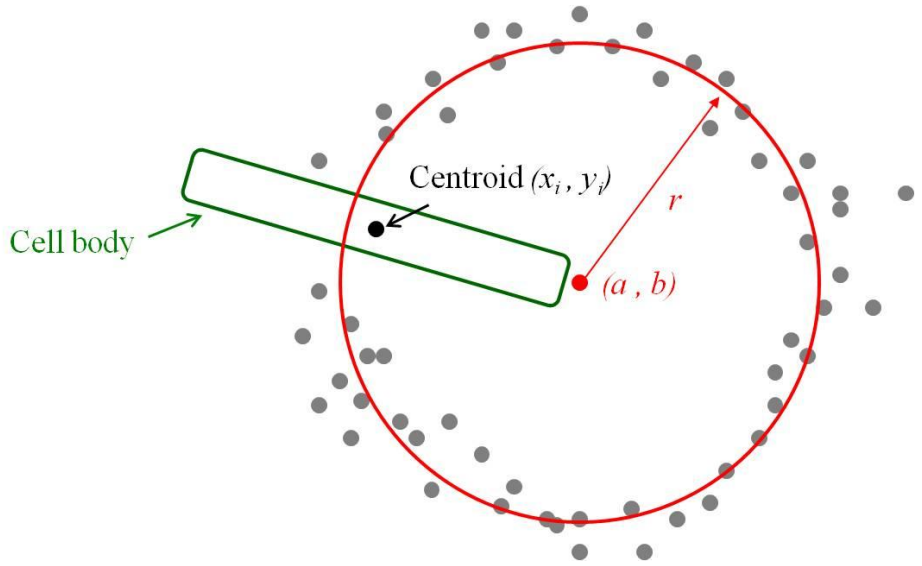

Figure 3.1 Illustration of equation (3.1)

The green rod represents the outline of the cell body, the black dot (x_i, y_i) represent as the centroid of the cell body, gray dots represent the most recent centroids measured. The red circle is the best fitting circle for all the gray dots, centered at (a,b) with a radius of r.

As the major problem we encountered was the shifting of the rotational axis. The re-adjustment serves as a local fitting which can accommodate even the change of moving rotational axis because even if globally (the period of the whole video) the rotation is not stable such as in Figure 3.3 B, locally (during a short period of time when the axis does not change) the adjacent centroids fall on a trajectory of a circle. This resulted in a more rounded scattering pattern for trajectories of the rotating cell body (Figure 3.3 D). Thus, the instantaneous rotational speeds were no longer subject to bias from the varying positions of rotation axis (Figure 3.3 A). In some cases, it was observed that the tethered cell body stopped rotating and the centroid

oscillated near the same position, leading to a biased circle-fitting. For these cases, if the radius of the fitted-circle was smaller than a threshold (1/2 of the global fitted circle), the center coordinates were reassigned to those of the global center of a circle (Figure 3.3 D, cross) fitted from all data points.

The second component of BTAP is translation of the re-adjusted rotational trajectories into the rotational angle $\theta_i = \arctan(x_i / y_i)$ in order to measure the rotational speed (Figure 3.3 A). There are two considerations in this second component: to reduce the noise inherent in the rotations, and to obtain the rotational phase (i.e., CCW or CW) of the motor. To accomplish these two tasks, we generated the cumulative rotations (CR) from the rotational angles of the cell bodies as $CR = \sum_{k=0}^{k=i} \theta_k$ (Figure 3.3 E). This curve was then smoothed using a piecewise linear approximation algorithm, where the cumulative rotation curve was fitted with line segments. Such task has a computational complexity of $\mathcal{O}$ (n^3). To make the BTAP processing speed faster, we used the greedy bottom-up approach [90] to approximate the linear fitting: The curve was initially divided into many small segments, where each line segment only connects two adjacent data points. During each iteration, BTAP merges two neighboring line segments into a new segment if the benefit from the merge is the highest among all possible neighboring pairs. It reduces the computational cost from (n^3) to (n^2) without any significant compromise in finding the best linear approximation:

1> The cumulative rotation curve is separated into $N/2$ segments (N equals to total data points rounded down to even number), define as $seg_i (i = 1...N/2)$. So for each segment, marked as seg_i, it initially contains data points (x_{2i-1}, y_{2i-1}) and (x_{2i}, y_{2i}).

2> For each iteration, two neighboring linear segments with the lowest merging cost are merged into one linear segment. The merging cost is defined as the increase of sum of squared errors (SSE) results from such merge: the SSE of the newly formed line segment minus the sum of SSE of the two neighboring segments before the merge.

3> The greedy merge stops when total number of segments reaches an arbitrary cut – in our case this equals to $4N$ /(frame rate).

An empirical threshold was set at 0.5 Hz to distinguish the pause phase and rotation phases: any segment with its slope between -0.5 Hz to 0.5 Hz was considered as pause; any segment with its slope higher than 0.5 Hz was considered as CW; any segment with its slope lower than -0.5 Hz was considered as CCW.

3.3.2 Speed analysis of peritrichous and monotrichous bacteria

To determine the effectiveness of BTAP, we first applied it on peritrichous *E. coli*, which has been extensively studied using cell tethering analyses [32], [47], [91]. The scattering raw data of *E. coli* rotation follows an exact circle (Figure 3.2 B), which reflects the stable rotation of tethered *E.*

coli. Because of this stability, BTAP does not drastically change the measured results (Figure 3.2 A, C and B, D). In order to reduce the noise from the instantaneous rotation speed (Figure 3.2 C), data were transformed into cumulative rotations, where the slopes of the curve indicate the rotational speeds (Figure 3.2 E). This resulted in rotational trajectories with clear rotation directions. It is also noteworthy that for each rotation phase (CCW or CW), the corresponding segment in the cumulative curve was very close to a straight line, indicating that for each phase the bacterium keeps a relatively constant rotation speed. These results agree with previous studies using tethered *E. coli* strains [92].

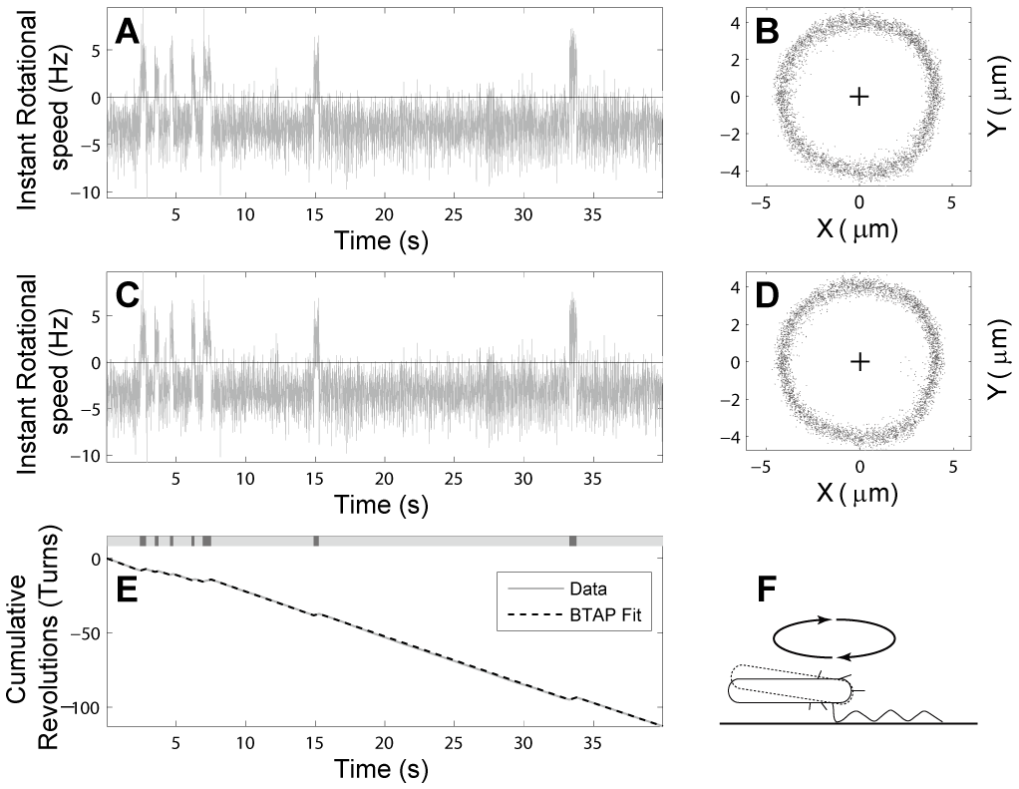

Figure 3.2 Rotation profile of a sample tethered *E. coli*

(A & C) Instantaneous rotational speed of the tethered *E. coli* cell before and

after BTAP adjustment, respectively. (B & D) The scattering of the centroid positions of the tethered cell before and after the BTAP adjustment, respectively. The cross indicates the assumed rotation axis. Note that the points fall into a smooth circle and does not require re-fitting. (E) Cumulative rotation of the same cell (solid gray line) and the line fitted by BTAP algorithm (dashed black line). Top bar: labeling of rotational phases, where dark gray denotes CW, light gray CCW, and white the pause phase. CW and CCW phases can be clearly separated. (F) Illustration of a tethered *E. coli* cell. The cell is tethered parallel to the surface and a small perturbation to the cell body (dashed) does not change its centroid position by much as viewed from the top.

Next, we tested BTAP on the monotrichous *P. aeruginosa* tethered cells. Compared to *E. coli*, the rotation speed translated directly from the uncorrected coordinates appeared to have many pauses and fluctuations (Figure 3.3 A). The rotational trajectory of *P. aeruginosa* was also less stable (Figure 3.3 B). However, BTAP successfully resolved these. After BTAP correction, the high/low spike artifacts in the instantaneous speed (Figure 3.3 A) curve were eliminated and the true rotation of the cell was recovered, where coordinates fell into a clear circular shape (Figure 3.3 D), and the rotation speed also showed less noise (Figure 3.3 C). The re-adjustment, therefore, helped in representing the rotation phases in the cumulative speed curve precisely (Figure 3.3 E). This algorithm can, thus, separate the different rotational phases and calculate the average rotational speed for each rotation segment; yielding accurate statistics for the particular cell (Figure 3.3 E). A comparison between BTAP results and human manually labeled results has been shown in the Appendix section Figure 7.1. BTAP results are very robust against manual labeling.

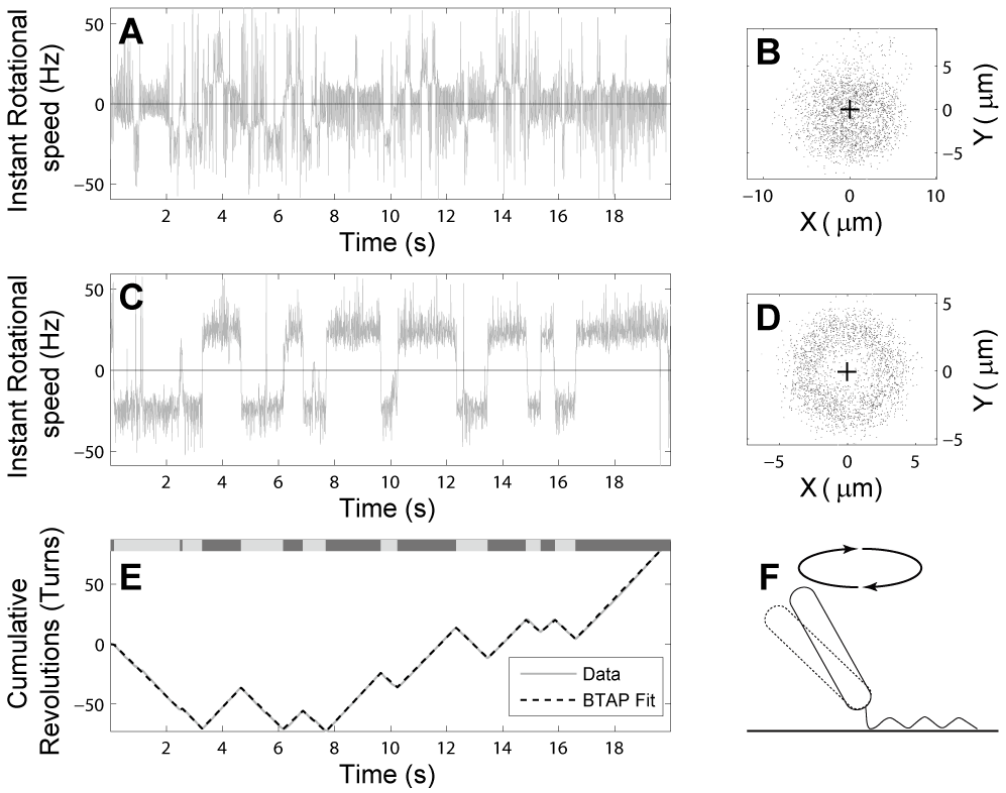

Figure 3.3 Rotation profile of a sample tethered *P. aeruginosa* cell

(A & C) Instantaneous rotational speed of the tethered *P. aeruginosa* cell before and after BTAP adjustment, respectively. (B & D) The scattering of the centroid positions of the tethered cell before and after the BTAP adjustment, respectively. The cross indicates the assumed rotation axis. Note that the points do not fall into a smooth circle in B and require re-fitting. (E) Corresponding cumulative rotations (E, gray line) and the line fitted by BTAP algorithm (E, dashed black line). Top bar: labeling of rotational phases, where dark gray denotes CW, light gray CCW, and white the pause phase. (F) Illustration of a tethered *P. aeruginosa* cell. The cell is tethered at an angle to the surface and a small perturbation to the cell body (dashed) largely changes its centroid positions as viewed from the top.

3.3.3 Comparison of BTAP with previous methods

In a previous study, the moving average or weighted average method has been used to reduce the noise in data of instantaneous rotational speed [60]. To demonstrate the performance of BTAP, we therefore compared BTAP to a simple moving average system (MA), which uses a 30-point moving

average window to smooth the instantaneous speed. We saw that MA yielded results that were very noisy (Figure 3.4 B) compared with the data treated with BTAP (Figure 3.4 C). Although by applying the moving average, one can get a smooth speed curve, it did not correct the systematic error rooted from the incorrect positioning of the rotational axis, as many of the speed time series were near zero (Figure 3.4 B). It was also difficult to differentiate the rotational phases (Figure 3.4 B, D) by either using instantaneous rotational speed or cumulative revolution curve from MA system. However, using BTAP, cell phases that had been earlier incorrectly recognized to be in the pause phase, were now identified to be in the CW rotation (Figure 3.4 C, E). The cumulative curve, therefore, had an increase in the CW/CCW contrast, allowing BTAP to accurately differentiate the CW/CCW/Pause phases and mark the precise moment at which the motor switched its rotation direction (Figure 3.4 E, top bar). As a result, BTAP measured the tethering data with correction of the positions combined with noise reduction, and can better capture the statistical properties of the *P. aeruginosa* flagellar motor.

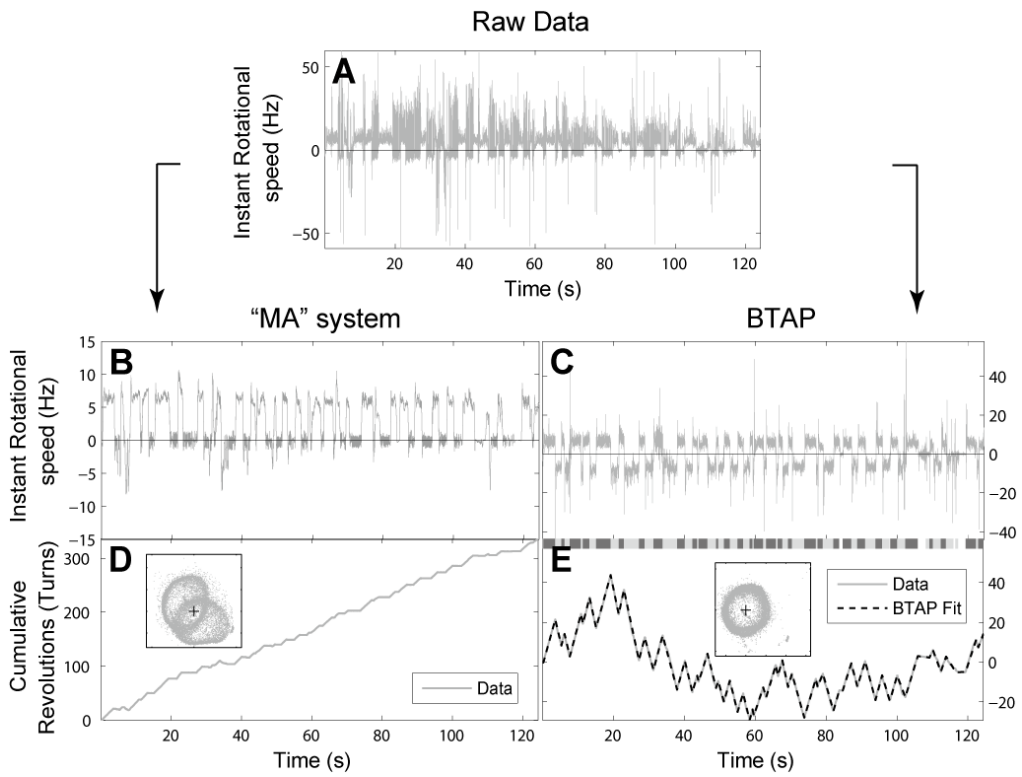

Figure 3.4 Comparison between a simple moving average system ("MA") based on instant rotational speed (Left panels) and BTAP (Right panels)

(A) Raw instantaneous rotational speed signal before "MA" and BTAP processing. (B) The moving average of the raw signal (without BTAP adjustment) using a window of 30-points by the "MA" system. (C) Raw signal after BTAP correction. (D) Cumulative revolution measured by "MA". (E) Cumulative revolution and fitting measured by BTAP. Top bar: labeling of rotational phases where dark gray denotes CW, light gray CCW, and white the pause phase. Inset of (D & E): The scattering of the centroids positions of the tethered cell. The cross indicates the assumed rotation axis. BTAP is able to re-fit the shifting centers of rotation in a polar-flagellated, tethered cell, in order to recover the true rotational behavior of the motor.

3.3.4 BTAP reveals the *P. aeruginosa* and *P. putida* flagellar motor to function with an additional pause phase

As the improved noise reduction and center adjustment system in BTAP allows for analyses of polar-flagellated bacteria, we next studied the

flagellar motor function of Pseudomonas spp. in detail. First, in the analyses, we tracked the CCW and CW speed distribution of both *P. aeruginosa* and *P. putida*, and showed that for both strains, the speed distributions of both the CCW and CW rotation directions were symmetric to each other (Figure 3.5 A-B). In comparison of the two, *P. aeruginosa* had a similar speed distribution to *P. putida* (Figure 3.5 A-B), where the average speed was not significantly different as well (Figure 3.5 G). In addition, the interval distributions for CCW/CW/Pause followed an exponential distribution (Figure 3.5 D-E), with mean times of 1.30 s/1.15 s/0.85 s respectively, for *P. putida*, and, 1.10 s/1.05 s/0.61 s respectively, for *P. aeruginosa* (Figure 3.5 H). The average durations of CCW/CW/Pause for *P. aeruginosa* were all lower than *P. putida* (Figure 3.5 D-E, H) while the speed distribution (Figure 3.5 A-B) and average speed (Fig. 4G) was comparable, indicating that *P. putida* exhibits less switching frequency (Figure 3.5 I). Notably, the rotation speeds for both Pseudomonas strains (5-6 Hz, Figure 3.5 G) were also comparable to those previously reported for *R. spharoides* (~5 Hz) and *E. coli* (4-9 Hz) under similar, unstimulated growth conditions [11], [80], [92]. The interval distributions for *E. coli* were also exponentially distributed, but the mean time for CCW phase is considerably longer than that of CW phase (CCW/CW 2.59 s/1.38 s). This is similar to previous reports for *E. coli* where the CW/CCW rotation interval of distribution showed to follow an exponential distribution [91], [92].

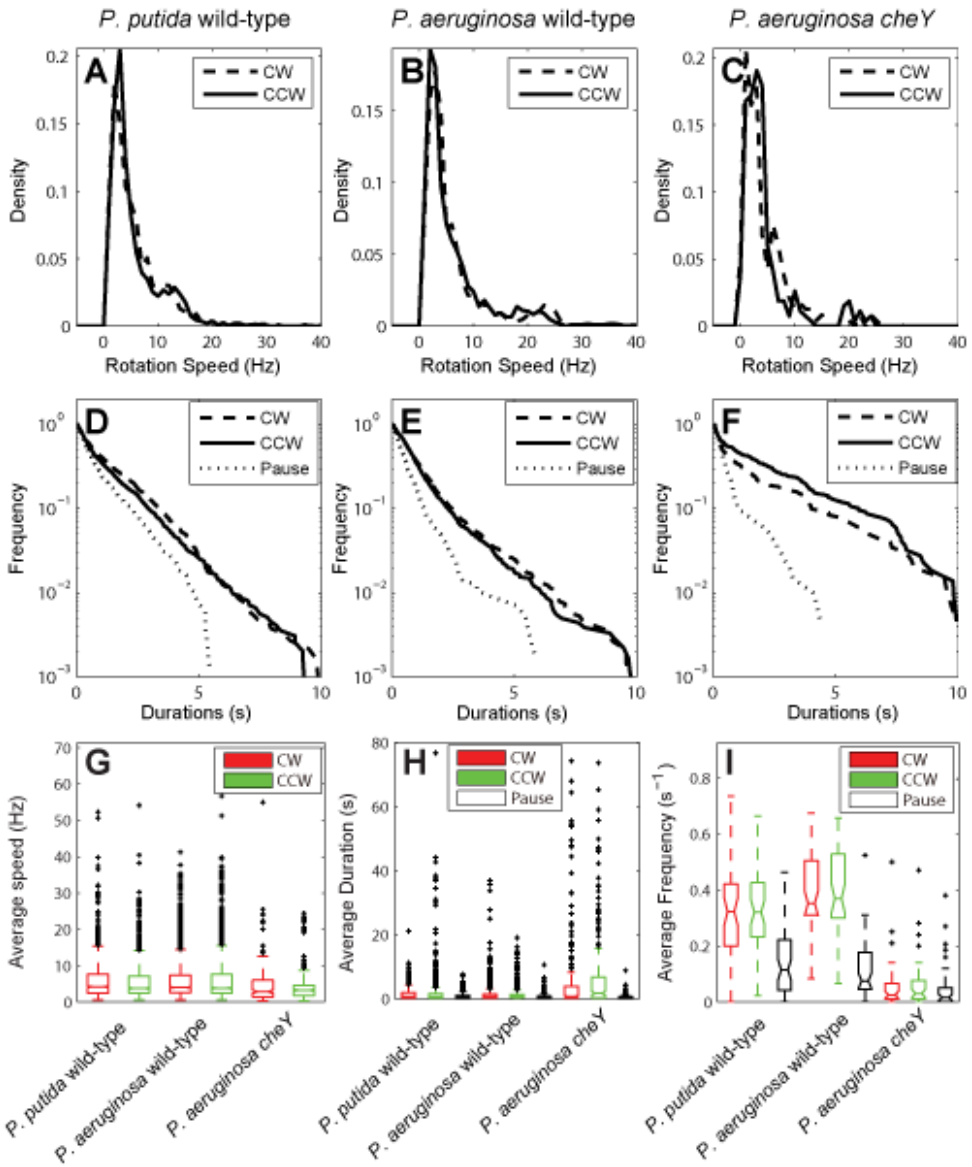

Figure 3.5 Speed and interval analysis between *P. aeruginosa* wile-type, *P. aeruginosa cheY* mutant and *P. putida* wild-type

(A-C) are rotational speed distributions of *P. putida* (KT2440) strain, and *P. aeruginosa* (PA01) strains wild-type, and *cheY*, respectively. (D-F) The corresponding cumulative distribution of interval durations from the strains in Fig. 4A-C, respectively. Solid lines denote CCW rotation; dashed lines denote CW rotation; dotted lines denote pauses. Note that the wild-type *P. aeruginosa* has longer pause durations compared to *cheY*. (G, H & I) The average speed, average duration of intervals, and occurrence frequency of phases, for the strains in Fig. 4A-C, respectively. Red box denote CW, green CCW, and block

the pause phase. On each box, the central mark is the median, the edge of the box are the 25^{th} and 75^{th} percentiles, the whiskers extend to the most extreme data points not considered outliers, and outliners are plotted individually as small black crosses. The maximum whisker length $w = 1.5$ and points are drawn as outliers if they are larger than $q_3 + w(q_3 - q_1)$ or smaller than $q_3 + w(q_3 - q_1)$, where q_1, q_3 are the 25^{th} and 75^{th} percentiles respectively. $w = 1.5$ corresponds to 99.3 coverage if the data are normally distributed. The frequencies for CW/CCW/Pause in *cheY* were reduced compared to the wild-type. Unlike *P. aeruginosa* wild type, *cheY* mutants also have increased CCW and CW durations.

We observed that *P. aeruginosa* cells spent nearly equal duration of time during CW (43%) and CCW (49%) rotation, and in addition, a pause phase which consisted of 8% of the total time tracked (Figure 3.6 B). During this pause phase, the tethered cell body stopped rotating for a short time interval before it resumed motion. *P. putida* also exhibited three phases, CW (47%), CCW (41%) and pause (12%) (Figure 3.6 A). This rotational pattern is different from that exhibited by *E. coli* cells, where the total time spent in CCW phase in *E. coli* is 50% longer than that in CW phase and the total pause phase is short (6%) [92]. There are three possible transitions for *P. aeruginosa* and *P. putida*: CW↔CCW, CW↔Pause, CCW↔Pause. The transition probabilities between phases for both strains were symmetric. For instance in the CW↔CCW transition, the chances of switching from CW to CCW were similar (37% for *P. aeruginosa*, and 32-33% for *P. putida*) to that from CCW to CW. The transition between CW and CCW in *E. coli* was also shown to be symmetric (data not shown).

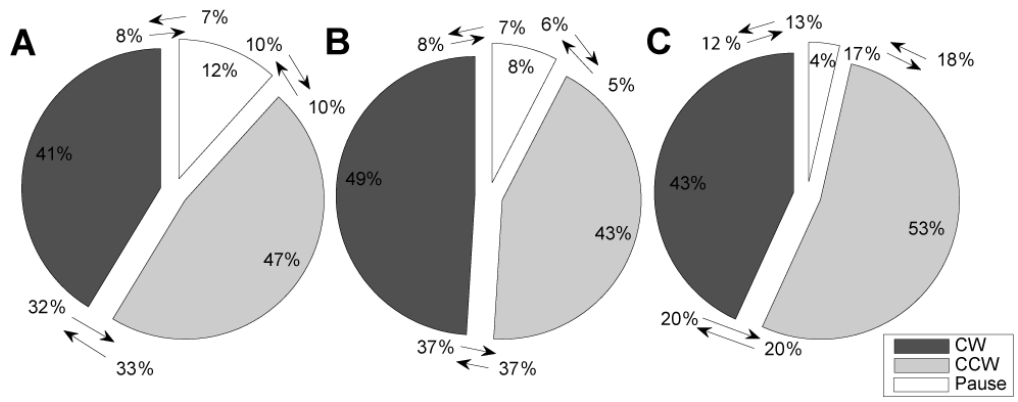

Figure 3.6 Time spent on different phases

(A) Time spent on CW/CCW/Pause phase for *P. putida* are 47%/41%/12%

respectively. (B) Time spent on CW/CCW/Pause phase for *P. aeruginosa* mPA01 are 43%/49%/8% respectively. (C) Time spent on CW/CCW/Pause phase for *P aeruginosa cheY* are 43%/53%/4% respectively. The transition probabilities between phases are shown as the arrows indicate. Dark gray denotes CW, light gray CCW, and white the pause phase. Note the drastic decrease in time spent in pause frequency between *P. aeruginosa cheY* (4%) and wild-type (8%) strains.

3.3.5 Positive correlation of pause phase with turn angles reveals a novel "run-reverse-turn" mechanism

It is noteworthy that although *Pseudomonas* cells pause at similar frequencies (0.12-0.14 Hz versus 0.16 Hz) compared to *E. coli*, the *Pseudomonas* cells spend a higher fraction of time pausing (8-12 % vs. 4.8 %). While earlier reports for *E. coli* may have omitted this phase due to the shorter duration [93], the pause phase may be a genuine and unique feature of the bacterial flagellar motor, being particularly pronounced for the polar flagellated *Pseudomonas* spp. In order to examine this phase further, we tested a *cheY* chemotaxis mutant of *P. aeruginosa*. The frequency of CW/CCW phases was lower than the wild-type *P. aeruginosa* PAO1 (0.05 s^{-1} vs. 0.4 s^{-1}, Figure 3.5 I) and as expected, the duration for a CW/CCW phase was longer (~ 8.0s versus ~1.5s, Figure 3.5 E-F, H). However, in contrast, the duration of pauses did not increase as in the CW/CCW phase but decreased instead (Figure 3.5 E-F). This suggests that the run length of a cell, and, both the frequency and duration of a pause are regulated by CheY in *P. aeruginosa*. In addition, the *cheY* mutant has a suppressed CW rotation, such that the tethered cells spend slightly more time in CCW rotation phase (53% versus 43%, Figure 3.6 C).

We propose that the pause phase allows the cell body to reorient and swim at a different direction, and we tested this by observing if the pause periods corroborated with turn angles in trajectories of free-swimming *P. aeruginosa* cells (Figure 3.7 A-B). Speed analyses revealed that the speed of the free swimming cells (≈5-40 μm/s) corroborated with previous reports (≈40 μm/s) [62], and additionally, we noticed that cells also exhibited pauses in their trajectories. Notably, these cells that pause (Figure 3.7 C) also often turn at an angle (inset). In these examples, when cells are swimming, they often do so in a clear direction, but when cells enter the pause phase, the cell bodies appear to be reorienting their position, allowing the cell to change direction when they resume swimming. The level of reorienting can be defined as turn angles - angles of moving directions before and after pauses. As a bacterium may follow (run) or change (reverse) its moving status after a turn, the according turn angle by definition is θ and $\pi-\theta$ respectively, the turn angles from population analyses of the trajectories are folded into the range of $(0,\pi/2)$ (Figure 3.7 A). The average turn angle sizes are positively correlated with pause durations (Figure 3.7 B), and we hypothesize that this positive relation is due to the rotational diffusion. This positive correlation was also observed in *cheY* cells (Figure 3.7 D-E), although the overall pause durations were not as long as wild-type cells (Figure 3.7 B, E). Notably, the shorter pause durations in *cheY* free swimming cells also corroborated with the shorter pause durations of tethered cells when compared to wild-type cells.

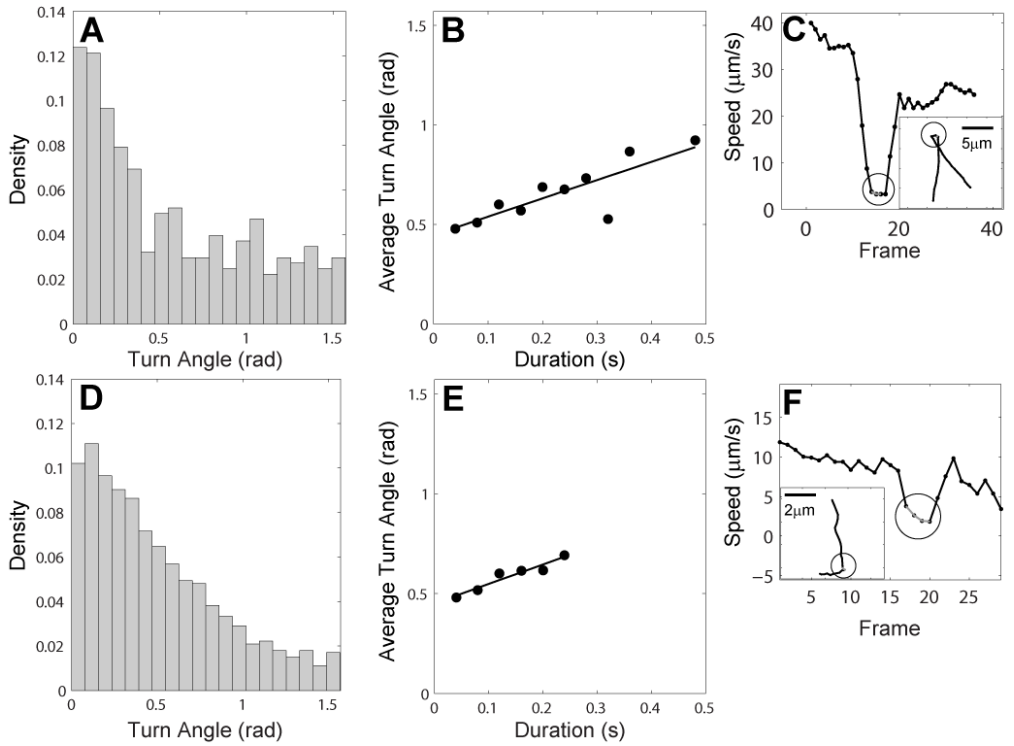

Figure 3.7 Pause durations are positively correlated with turn angles

(A & D) Distribution of the turn angles (change of directions) during pauses for *P. aeruginosa* wild-type and *cheY* mutant strains respectively. Angles between $\pi/2$ and π are subtracted from π as the change of cell body orientation during a pause followed by a reversal. The densities for both strain decrease as turn angles become larger. The pauses are defined when the moving speed of the cell is below 5 μm/s for at least 3 consecutive frames. (frame rate=25fps) (B & E) The average turn angle sizes are positively correlated with pause durations. The line is a linear regression fitting of the data. The y-value of each point is the average of all the turning angles at certain duration (x-value). If the turn angle at certain duration measured is less than two, the point will not be counted to avoid bias from data scarcity. (C & E) Speed of two sample cells from *P. aeruginosa* wild-type and *cheY* respectively. The insets are their corresponding trajectories. The circles mark the section of pauses.

3.3.6 The function of stator protein MotAB and MotCD in motility of *P. aeruginosa*

Comparing to *E. coli*, whose motors are powered by a set of torque generating MotAB protein complexes, *P. aeruginosa*'s flagellar motor has two

sets of torque generators named as MotAB and MotCD [62], [94]. In these two sets, MotA and MotC are homologous counterparts whereas MotB and MotD are homologous counterparts. It was known that either stator MotA/B or MotC/D is sufficient for the motility of *P. aeruginosa*, but their double mutant has a total elimination of the swimming function. In addition, MotA/B and MotC/D can function interchangeably (i.e. MotA/D and MotB/C also provide motility capability), suggesting a mixed function between the two complexes [62]. On the other hand, both MotAB and MotCD are crucial in biofilm formation, as mutation in either stator resulted in dysfunction of early attachment of the bacteria to a surface, and subsequently the formation of the biofilm [95]. The detailed function of MotAB and MotCD and their relation are not yet clear. Therefore, it is interesting to use BTAP to study the role that MotAB and MotCD play during the motility and chemotaxis of *P. aeruginosa*.

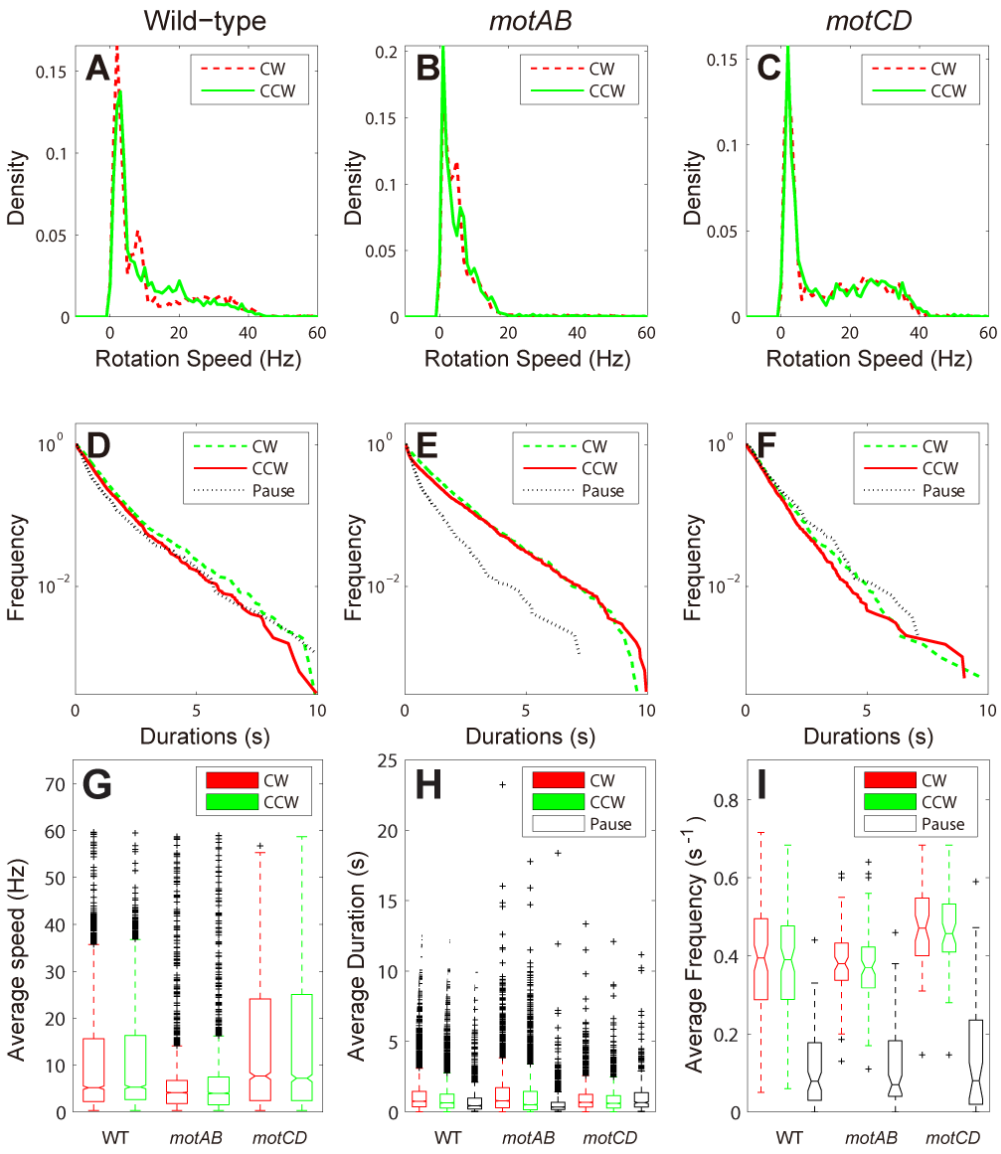

Figure 3.8 Speed and interval analysis between *P. aeruginosa* wile-type, *P. aeruginosa motAB* mutant and *motCD* mutant

(A-C) are rotational speed distributions of *P. aeruginosa* wild-type strain, *motAB* and *motCD mutant* strains, respectively. (D-F) The corresponding cumulative distribution of interval durations from the strains in A-C, respectively. Solid green lines denote CCW rotation; dashed red lines denote CW rotation; dotted black lines denote pauses. (G, H & I) Boxplots of the average speed, average duration of intervals, and occurrence frequency of phases, for the strains in A-C, respectively. Red box denote CW, green CCW, and block the pause phase. On each box, the central mark is the median, the edge of the box are the 25th and 75th percentiles, the whiskers extend to the most extreme data points not considered outliers, and outliners are plotted individually as small black crosses. The maximum whisker length $w = 1.5$

and points are drawn as outliers if they are larger than $q_3 + w(q_3 - q_1)$ or smaller than $q_3 + w(q_3 - q_1)$, where q_1, q_3 are the 25th and 75th percentiles respectively. $w = 1.5$ corresponds to 99.3 coverage if the data are normally distributed. Results are from 96 wild-type cells, 85 *motAB* mutant cells and 53 *motCD* mutant cells.

We compared the wild-type with the *motAB* and *motCD* mutants through BTAP analysis (Note: due to the conflict in strain naming among different research groups, the *motAB* mutant strain we obtained from the research group of Prof. Linda L. McCarter had a deletion of genes that accounts for "MotA/B" proteins in *P. aeruginosa* and the *motCD* mutant strain we obtained had a deletion of genes that accounts for "MotC/D" proteins in *P. aeruginosa*. However the "MotC/D" proteins in *P. aeruginosa* is a closer homolog to *E. coli*'s "MotA/B" proteins. So for the strains that we used, *motAB* mutant strains possesses stator proteins that are similar to those in *E. coli*, not the *motCD* mutant). While the average durations of CW/CCW rotation (Figure 3.8 H) and the frequencies of these (Figure 3.8 I) appeared to be similar, the average speeds for the wild-type/*motAB*/*motCD* were 10.59/5.69/13.21 Hz for CW rotations and 10.40/5.71/13.51 Hz for CCW rotations, respectively (Figure 3.8 G). It appeared that the *motCD* strain was significantly faster than the wild-type, which was also faster than the *motAB* mutant strain. We also analyzed the speed profile of each strain. In each strain, the speed distributions of both the CCW and CW rotation directions were similar to each other (Figure 3.8 A-C). The speed distribution of the *motCD* mutant strain had two modal clumps, one peaked at a slow speed at < 5 Hz and the other peaked at a much faster speed at ~25 Hz (Figure 3.8 C). However the

speed distribution of *motAB* mutant strain had only a single mode (Figure 3.8 B), comparable to the peak at slow speed of *motCD*. The wild-type, containing both MotAB and MotCD protein complexes, also showed two modal clumps in the distribution of speeds. Moreover, the two modes of the wild-type and the *motCD* peaked at around the same speed level, suggesting that the speed levels exhibited in the wild-type resulted from the combination of MotAB and MotCD stator proteins, and overall the effect from the MotAB proteins and MotCD proteins overlapped in the wild-type.

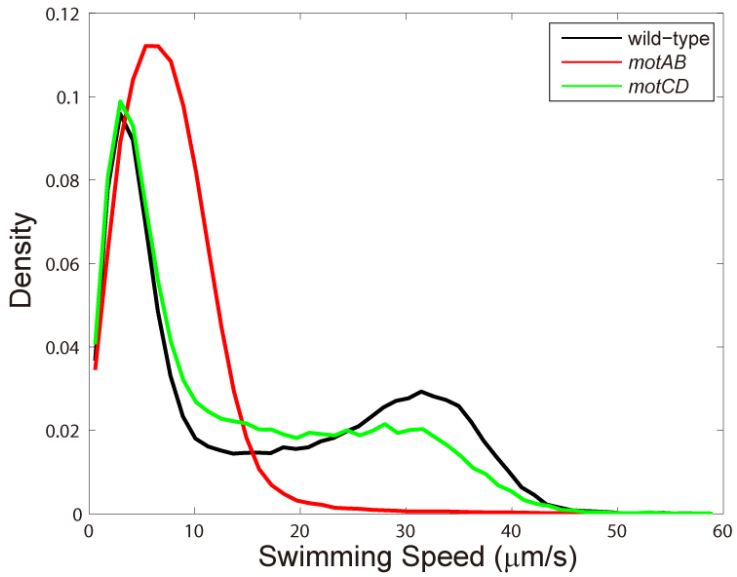

Figure 3.9 2D speed distribution of swimming *P. aeruginosa* wile-type, *P. aeruginosa motAB* mutant and *motCD* mutant strains

The black curve designates wild-type cells, red curve *motAB* cells and green curve *motCD* cells. Data are analyzed from tracked trajectories of 10852 wild-type cells, 10368 *motAB* cells and 6348 *motCD* cells.

The results from the tethered experiments were corroborated by the measurement of swimming speeds of *P. aeruginosa* wile-type, *P. aeruginosa motAB* mutant and *motCD* mutant strains. The *motCD* mutant strain and the wild-type had two modal clumps in the distribution of its swimming speed in

the 2D space while speed distribution of the *motAB* mutant strain had only one mode (Figure 3.9). For the two major speed levels represented by the two peaks in the *motCD* mutant strain and the wild-type, there could be two interpretations: 1) The two modes are represented by two sub populations in *P. aeruginosa* where one has lower speed motors and the other has high speed motors. In this interpretation, we thus required each flagellar motor to have only one speed level. 2) The two speed levels result from the property of the flagellar motors possibly having different rotational speed levels. To our understanding the latter interpretation is more likely, because it would be hard to justify a separation of population that grew in same experimental conditions, especially that the *motAB* mutant strain did not exhibit such separation. More importantly, we did observe varied rotational speed levels in single cells of wild-type (Figure 3.10) and *motCD* mutant strain (Figure 3.11). In the case of the wild-type, the instantaneous rotational speed of the tethered cell displayed one consistent speed level for CCW rotation at about 3 Hz, and two consistent speed levels for CW rotation at about 3 Hz and 20 Hz, respectively (Figure 3.10 A). In the case of the *motCD* mutant strain, the instantaneous rotational speed of the tethered cell displayed two consistent speed level for CCW rotation at about 5 Hz and 15 Hz, and two consistent speed levels for CW rotation at about 5 Hz and 20 Hz, respectively (Figure 3.11 A).

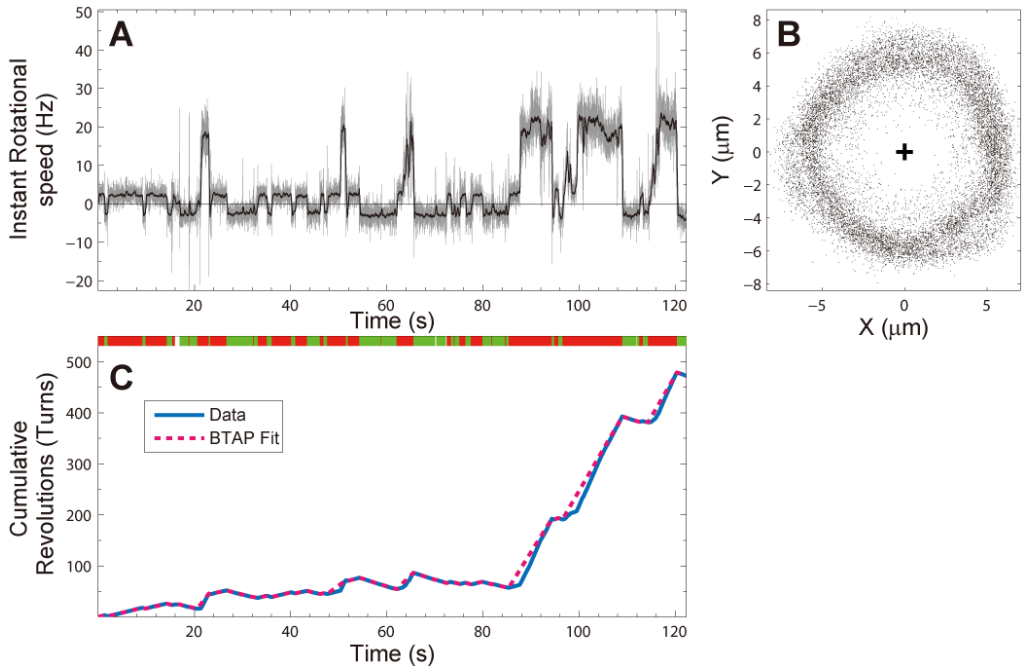

Figure 3.10 Rotational profile of a wild-type *P. aeruginosa* cell showing varied speed levels

(A) Instantaneous rotational speed of a tethered wild-type *P. aeruginosa* cell (gray line) and its moving average with a window of 0.25 s (40 frames) (black line). Note that the moving average line shows two regimes of rotational speed for the CW rotation: one below 3 Hz and the other around 20 Hz. (B) The scattering of the centroid positions of the tethered cell before and after the BTAP adjustment, respectively. The cross indicates the assumed rotation axis. (E) Corresponding cumulative rotations (C, blue line) and the line fitted by BTAP algorithm (E, dashed purple line). Top bar: labeling of rotational phases, where red denotes CW, green CCW, and white the pause phase.

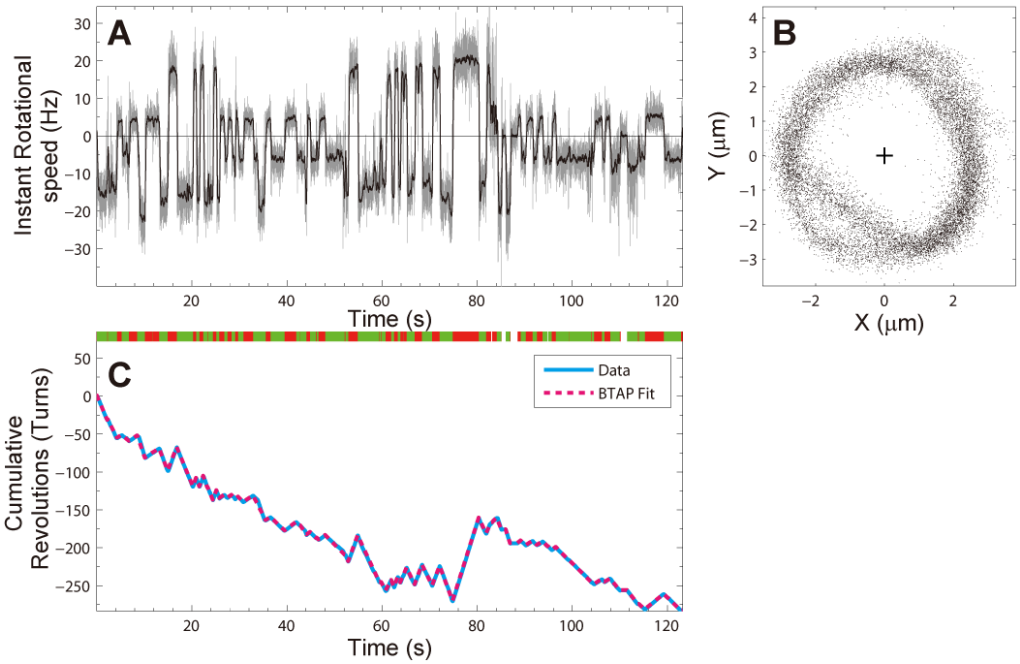

Figure 3.11 Rotational profile of a *motCD* mutant *P. aeruginosa* cell showing varied speed levels

(A) Instantaneous rotational speed of a tethered *motCD P. aeruginosa* cell (gray line) and its moving average with a window of 0.25 s (40 frames) (black line). Note that the moving average line shows two regimes of rotational speed for the CW rotation: one around 5 Hz and the other around 20 Hz, and two regimes for the CCW rotation: one around 5 Hz and the other around 15 Hz. (B) The scattering of the centroid positions of the tethered cell before and after the BTAP adjustment, respectively. The cross indicates the assumed rotation axis. (E) Corresponding cumulative rotations (C, blue line) and the line fitted by BTAP algorithm (E, dashed purple line). Top bar: labeling of rotational phases, where red denotes CW, green CCW, and white the pause phase.

This is corroborated with a recent study [96] which found that another species in the *Pseudomonas* family, *P. putida*, possessed alternating two levels of swimming speeds separated by reversals. The two speed levels form a bi-model distribution and are alternating (i.e., one from forward movement and the other from backward movement, or vice versa). The swimming speed changed between these two speeds on average by a factor of two, and this motion pattern may largely enhance the mean-square displacement of the

species as compared to swimmers moving at constant speed. This may give evolutionary advantage to some monotrichous bacteria that can only undergo "run-and-reverse" type of movement so that they can explore their environment more efficiently without additional energy cost.

3.3.7 The function of stator protein MotAB and MotCD in chemotaxis of *P. aeruginosa*

To further understand the function of MotAB and MotCD in chemotaxis, we analyzed their chemotactic response after the addition of chemoattractant serine (Figure 3.12) and chemorepellent trichloroethylene (TCE) (Figure 3.13). The interval durations of CW and CCW rotation for wild-type, *motAB* and *motCD* mutant strain all increased after the addition of the chemotattractant (Figure 3.12 E-H, M-P and U-X). These increases were most prominent during the most immediate 30 seconds after the addition of the chemoattractant (Figure 3.12 F, N and V), as the cumulative distribution curves are shifted toward longer duration intervals, and they reduced gradually to their levels before the addition of the chemoattractant (Figure 3.12 G, H, O, P, W and X) However, the changes of speed distributions of these strains after the addition of the chemoattractant were less significant (Figure 3.12 A-D, I-L and Q-T). Compared to their respective control groups, speed distributions in the wild-type and the *motCD* mutant after the addition of chemoattractant seemed had more cases of higher speed levels (Figure 3.12 B-D and R-T) whereas the speed distribution of the *motAB* mutant strain had almost similar speed distribution before and after the addition of the chemoattractant. This

may suggest that the wild-type and *motCD* mutant strain, which possessed a similar set of stator proteins, may regulate the rotational speed of motors so that more high speed levels appear in response to an increased chemoattractant concentration. The *motAB* mutant strain on the other hand, due to the deletion of such genes, did not alter the speed of its motor.

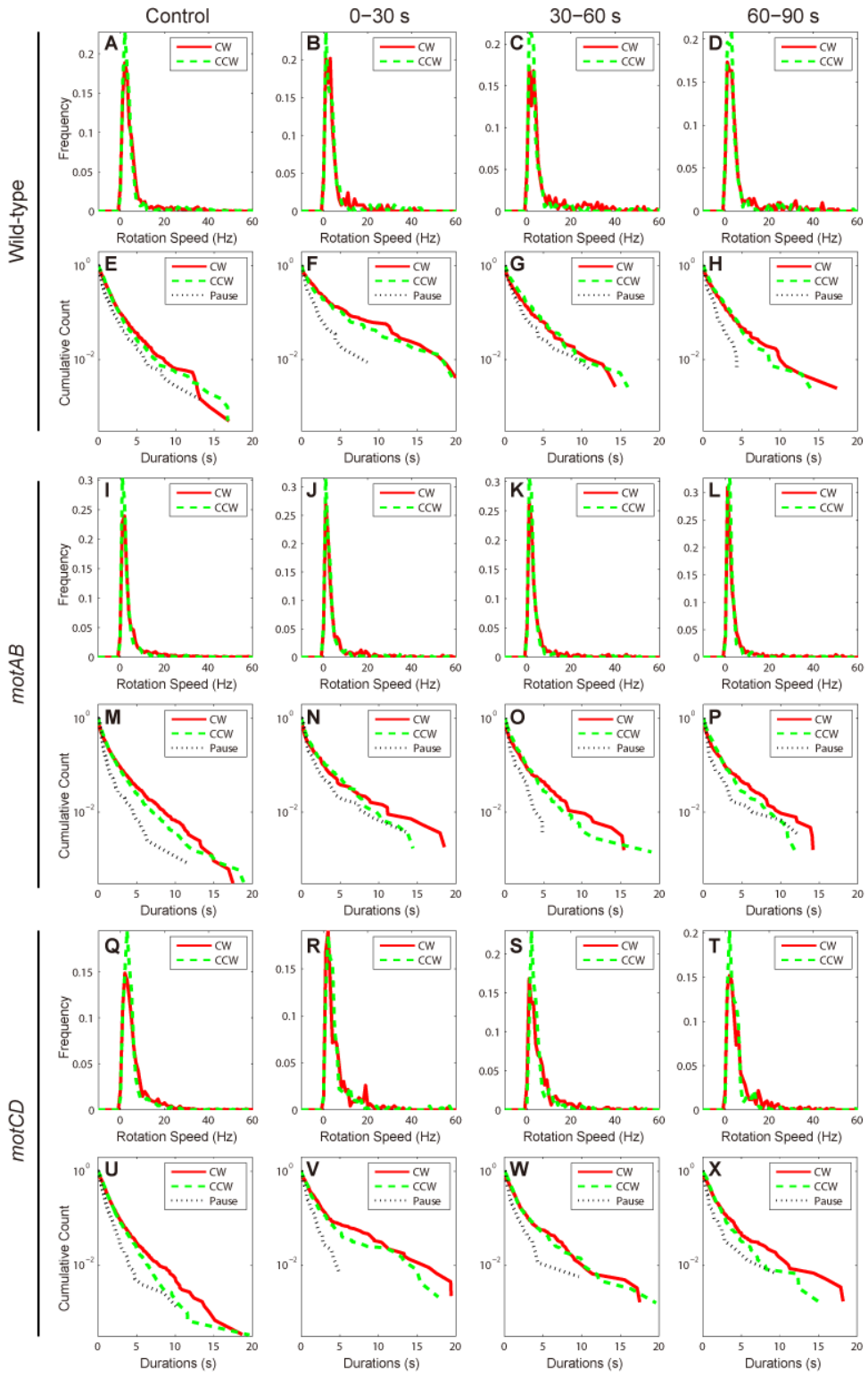

Figure 3.12 Speed and interval analysis between *P. aeruginosa* wile-type, *P. aeruginosa motAB* and *P. aeruginosa motCD* mutants after exposing to chemoattractant (Serine)

(A-D, I-L, Q-T) are rotational speed distributions of *P. aeruginosa* wild-type strain, *motAB* and *motCD* mutant strains, respectively. (E-H, M-P, U-X) are the corresponding cumulative distribution of interval durations from the three strains, respectively. of *P. aeruginosa* wild-type strain, *motAB* and *motCD* mutant strains, respectively. (A, E, I, M, Q and U, column of A) are corresponding samples in M9 control buffer for ~120 s. (B, F, J, N, R and V, column of B) are these samples in chemotaxis 0-30 s after adding 10 mM chemoattractant serine. (C, G, K, O, S and W, column of C) are these samples in chemotaxis 30-60 s after adding 10 mM serine. (D, H, L, P, T and X, column of D) are these samples in chemotaxis 60-90 s after adding 10 mM serine.

Dashed green lines denote CCW rotation; solid red lines denote CW rotation; dotted black lines denote pauses. Data are from 45 wild-type cells, 57 *motAB* cells and 66 *motCD* cells, respectively.

The interval durations of CW and CCW rotation for wild-type, *motAB* and *motCD* mutant strain all decreased after the addition of the chemorepellent (Figure 3.13 E-H, M-P and U-X). Different from the results from chemoattractant experiments as shown in Figure 3.12, we saw that these decreases were most prominent during the 30-60 seconds after the addition of chemorepellent (Figure 3.13 G, O and W), as the cumulative distribution curves are shifted toward shorter duration intervals. This indicated that the chemotactic responses to the chemorepellent are slower than that to the chemoattractant. This is partly corroborated with a study of chemotaxis of *P. aeruginosa* in the microfludic device. In the study, the wild-type *P. aeruginosa* in a flow with chemotaxis gradient responded positively to the attractant and negatively to the repellent, but it was suggested that the repellent, TCE, did not completely induce the chemotactic behavior as compared to the attractant [97]. In contrast to the chemoattractant test, the changes in speed distributions of these strains after the addition of chemoattractant seemed to be less significant (Figure 3.13 A-D, I-L and Q-T),

that in both the wild-type and the *motCD* mutant frequencies of the high speed levels did not change significantly. Taking together, the wild-type and both of the *motAB* and *motCD* mutants increased their durations of CW and CCW rotations in response to an increase of chemoattractant, but decreased these durations in response to a increase of chemorepellent. On the other hand, the changes of speed distribution of two sets of experiments were less conclusive. Nevertheless, these may indicate an asymmetric tactic of *P. aeruginosa* in chemotaxis that it increases its diffusion coefficient [96] if the external environment is favorable (increase in concentration of the chemoattractant) but decreases its diffusion coefficient if the external environment is unfavorable (increase in concentration of the chemorepellent).

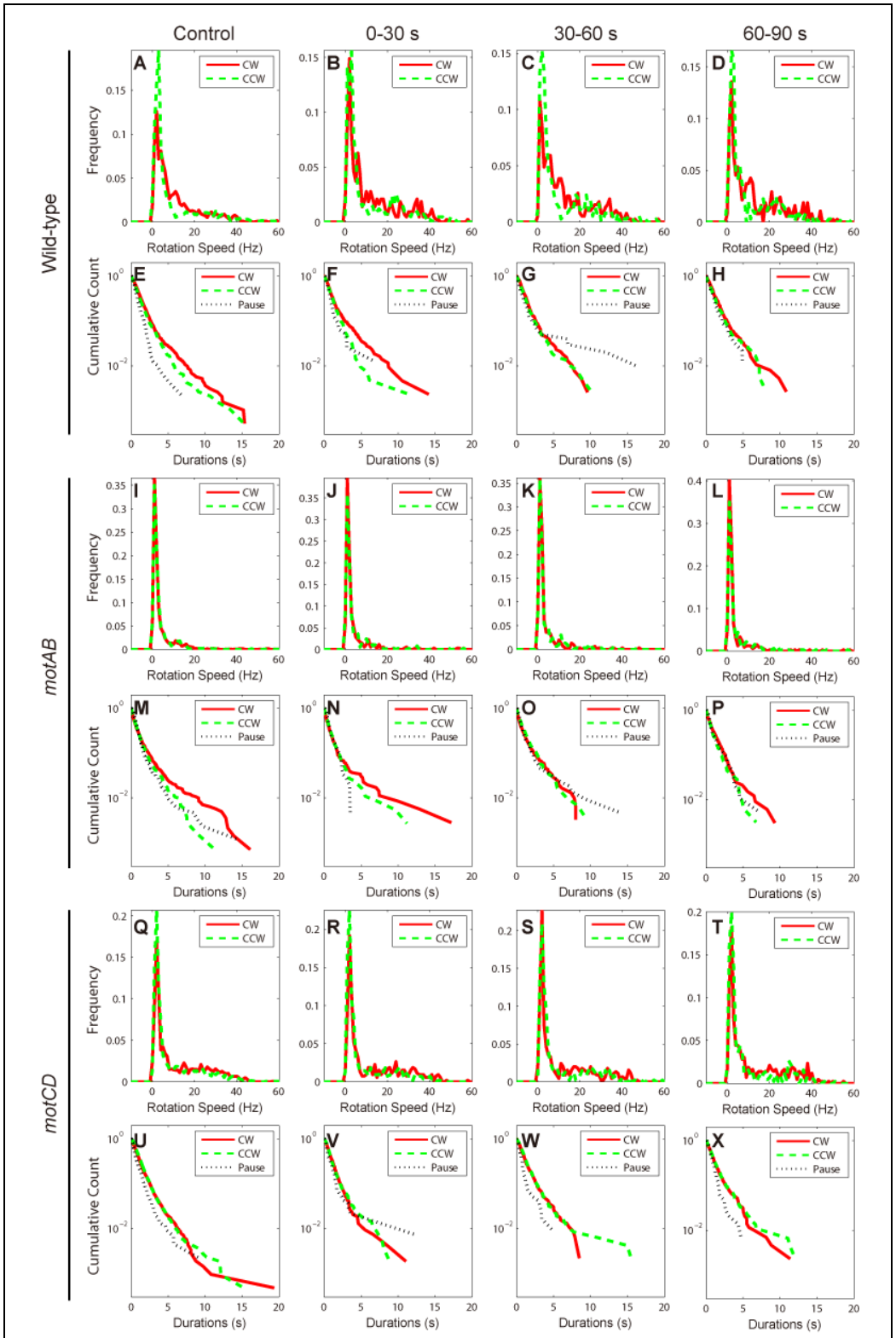

Figure 3.13 Speed and interval analysis between *P. aeruginosa* wile-type, *P. aeruginosa motAB* and *P. aeruginosa motCD* mutants after exposing to chemorepellent (Trichloroethylene, TCE)

(A-D, I-L, Q-T) are rotational speed distributions of *P. aeruginosa* wild-type strain, *motAB* and *motCD* mutant strains, respectively. (E-H, M-P, U-X) are the corresponding cumulative distribution of interval durations from the three strains, respectively. of *P. aeruginosa* wild-type strain, *motAB* and *motCD* mutant strains, respectively. (A, E, I, M, Q and U, column of A) are corresponding samples in M9 control buffer for ~120 s. (B, F, J, N, R and V, column of B) are these samples in chemotaxis 0-30 s after adding 10 mM chemorepellent TCE. (C, G, K, O, S and W, column of C) are these samples in chemotaxis 30-60 s after adding 10 mM serine. (D, H, L, P, T and X, column of D) are these samples in chemotaxis 60-90 s after adding 10 mM serine.

Dashed green lines denote CCW rotation; solid red lines denote CW rotation; dotted black lines denote pauses. Data are from 35 wild-type cells, 27 *motAB* mutant cells and 41 *motCD* mutant cells, respectively.

3.4 Discussion

Peritrichous bacteria such as *E. coli*, have multiple flagella growing everywhere their cell surface, while monotrichous bacteria such as *P. aeruginosa* has only one flagellum located at the pole of its cell body. Therefore, in cell-tethering experiments, when one flagellum is tethered to the surface after being sheared-off , the flagellum stub has a high chance of being at the side of the cell body, such that the cell body is nearly parallel to the surface it tethered, allowing a full rotation to be observed under the microscope (Figure 3.2 F). However, when polar flagellated bacteria such as *P. aeruginosa* are tethered to the surface, the cell body is usually not parallel to the tethered surface (Figure 3.3 F), allowing the cell body to change its orientation easily because of the flexibility at the flagellar hook [98]. Also, although theoretically the cell body should rotate with its own major axis even when it is tilted such as in (Figure 3.3 F), usually the connecting point at where the flagellar filament attached to the cell body is not perfectly at the pole, and the shape of the cell body is not perfect rod. The asymmetry in the

flagella's location causes the rotation of the cell body with respect to a rotational axis perpendicular to the tethered surface as in (Figure 3.3 F). In addition during the experiment, if a flagellum happens to attached perfectly at the pole aligning to the rotational axis, as what the top figure shows, the cell body will only rotate around its own axis. This will appeared to be a still cell from the microscopy since it will be impossible to discern the actual rotation of the cell body. These cells, even though they are rotation, are discarded from the microscopy point of view because it is impossible to separate them from the real 'still' dead cells.As a result of all these, the tethered cells with observable rotations cause difficulty in the image analysis process, as the observed tethered cells no longer rotate in a circular trajectory but often shift around, giving rise to a noisy rotational signal.

Our new program, therefore, has several advantages. 1) It reduces the position noise in the rotational tethered cell. Traditional methods only translate the centroid coordinate directly into the rotational phases, which is prone to error because when the actual rotation axis is slightly deviated from the presumed axis, a rotating rod with constant radial speed will show a changing instantaneous rotational speed. By correcting the actual rotational axis, we are able to isolate the rotational data that best reflect the actual rotation of the motor from the experimental video. 2) By measuring the accumulative revolution instead of instantaneous rotation, we can further reduce the rotational noise from the piecewise linear fitting. Previous method uses instantaneous speed to measure the rotation ω_i at frame i

$$\omega_i = \frac{\theta_i - \theta_{i-1}}{t_i - t_{i-1}}, \tag{3.2}$$

where θ_i is rotational angle at frame i and t_i is the corresponding time.

However, this approach results in a very noisy speed curve with a large variance. This is because tethered cells are not always rotating smoothly, but exhibit fluctuations in speed within each rotation. In addition, the tethered cells in the fluidic environment are affected by other surrounding factors, such as hydrodynamic effects or Brownian force, causing the position of the cell body to have a large variance [99]. The problem is more significant when the acquisition frame rate is high, that an incidental large angle change $\theta_i - \theta_{i-1}$ between two frames can produce a spike in the instantaneous speed curve. This can be partially alleviated by introducing a (weighted) moving average window to smooth the data, but the size of the window is subjective and can have a huge impact on the result. Conversely, our approach uses the cumulative revolution to fit the curve with multiple linear segments. Although the instantaneous speed curve may be noisy and have many spikes, because the time intervals between two frames are small, the impact of such spikes on the cumulative curve would be small and thus not affect the rotation trend (the slope of the curve). These noises can be easily removed by a linear fitting in the cumulative curve (3). Through extracting the turning points on the cumulative curve, we could separate the rotation phases of the tethered cell into clockwise, counterclockwise, and pause clearly. This is difficult to achieve in the instantaneous curve because the moving average window will

blur the boundary between different phases. As the smoothing result improves (i.e. the larger the window size), the ability for phase separation, in turn, weakens. However, using our approach, we were able to achieve both noise reduction and phase separation without sacrificing the accuracy of either.

As the cell-tethering experiment is one of the key techniques in quantifying the motor properties and its response in the chemotactic environment, it is important to enhance the accuracy of the data acquisition and analysis to reflect the change of motor phases in chemotaxis. Our new program, therefore, helps image processing and data analysis in monotrichous bacteria research and gives credible results for following studies.

We used our program to distinguish novel properties of the flagellar motor in *Pseudomonas* spp., where we were able to study its flagellar rotation in a high-throughput manner for the first time. First, the *Pseudomonas* flagellar motor spends an equal time in both CCW and CW rotations, which corroborates with earlier reports for free swimming cells, where trajectories adopt a "run and reverse" strategy [56]. Additionally, speeds in both directions are similar, suggesting that the flagellar motor is symmetric. Notably, we observed an additional pause phase, where about 12-23% of cells in motion (either CCW or CW) will choose to transit into. As there was a positive correlation between pause duration and turn angle sizes, our findings indicate that *Pseudomonas* spp. can vary its pause duration in order turn at different angles, resulting in a "run-reverse-turn" trajectory. This novel mechanism, therefore, allows the cell to swim and explore spaces more

efficiently that a typical "run-and-reverse" trajectory for polar flagellated bacteria.

Cells of polar-flagellated bacteria have a limited degree of freedom in motility where they can only swim forward and backward. It appears now that there are diverse ways, where such type of bacterial cells can compensate for their limited, bidirectional movement. In the case of *R. sphaeroides*, of which the motor can only rotate in one direction, cells adopt a "run-and-stop" motility [81] with variable speed [60], whereas in the sodium-driven *V. alginolyticus*, cells adopt three-step "run-reverse-flick" chemotactic response [57], [80] instead. Here, in the case of *Pseudomonas* spp., we observe a "run-reverse-turn" trajectory for both monotrichous and multitrichous *Pseudomonas* cells. The "run-reverse-turn" is mostly likely different from the "run-reverse-flick" reported. The mechanism of the "flick", proposed by a recent study [61], is the buckling instability of the hook structure at the base of the flagellar filament, which undergoes compression at the onset of forward swimming. The compression force exceeds critical load of the hook, rendering a bending of the structure and therefore causing the "flick". Note that the buckling is high-speed dependent with a threshold at around 50 μm/s. *Vibrio alginolyticus* has a sodium-driven motor [100] spinning much faster (~1000 Hz) than the motor in *P. aeruginosa* (< 50 Hz, Figure 3.4 B), and *V. alginolyticus* swims faster (~100 μm/s) beyond that threshold than *P. aeruginosa* (<50 μm/s, Figure 3.8). So we believe that the "flick" will not happen in the motion of *P. aeruginosa*. While earlier reports made brief

references to these turns in free-swimming trajectories [56], [88], we have now shown that the additional pause phase in the flagellar motors allow the cells to turn at larger angles.

In addition, it is known that chemotaxis mutants of *P. aeruginosa* are motile but rarely change their swimming directions [101], [102]. The question, therefore, arises whether the *Pseudomonas* chemotactic mechanism is similar to that of the peritrichous *E. coli*, or, whether the *Pseudomonas* motor employs a different response in general. We were able to elucidate this using BTAP - a chemotaxis mutant of *P. aeruginosa*, which has reduced CCW and CW frequency, and the duration in both CCW and CW directions are increased.

Interestingly, there is a reduction in both the frequency and duration of pauses as well. This suggests that the cells "turn" at a smaller angle, therefore, giving rise to trajectories that tend to be straight. Also, the average durations of the pause do not differ significantly, suggesting that the pause process may be an independent event that is not regulated by chemotaxis signaling pathways. Taken together, the *Pseudomonas* motor may undergoes chemotaxis by varying its pause or switch durations, and therefore the frequencies, resulting in cells that have longer "runs" and fewer "turns". In comparison to other species, it is known that *E. coli* increases its run length through a decrease in switch frequency resulting in an increase in CCW rotation [48]. In the case for *P. aeruginosa*, we show that unlike *E. coli*, run length is increased through a decrease in pause frequency and duration, and an increase in both CW and CCW durations. In the case for the three-step run-reverse-flick *V.*

alginolyticus, cells have decreased flicking frequency while retaining their turn angle sizes [57]. Notably, while *V. alginolyticus* uses a "flick" to change its turn angle, we show here that *P. aeruginosa* adopts a pause mechanism to turn, and these "turn" angles are decreased as part of the chemotactic response. In the case for *R. sphaeroides*, a decrease in stop frequency was observed [103], which was a similar response observed in the *cheY P. aeruginosa* mutant. Therefore, in comparison to these three species, we show that while the details of the control of the flagellar motor differs, the outcomes of longer run lengths and reduced turn (or tumbling) frequency remains broadly conserved in *P. aeruginosa*. The *Pseudomonas* motor, therefore, adopts a combination of different properties in its chemotactic response, once again revealing the complexity of the *Pseudomonas* chemosensory system [83].

4 COMBINED EXPERIMENTS AND COMPUTATIONAL MODELING REVEAL A RECTIFIED RUN-AND-REVERSE MECHANISM FOR *PSEUDOMONAS AERUGINOSA* CHEMOTAXIS

Chapter 4, in most part, is a reprint of the material in a manuscript that has been submitted. The dissertation author was the first author who conducted the research and wrote this paper.

4.1 Introduction

Flagellated bacteria swim by rotating their flagella [2]. Each flagellum is controlled by a molecular motor that can rotate either counterclockwise (CCW) (when viewed from behind the cell) or clockwise (CW). In the model peritrichous species *Escherichia coli*, motility is best described by a "run-and-tumble" mechanism: When all the flagella rotate CCW, they form a bundle that propels the bacterium to "run" in a nearly straight path; when some of the flagella switch their rotation direction to CW the bundle is disrupted, causing the cell to "tumble" and change swimming direction [3]. The probability of a motor in CW rotation and therefore the cell "tumbling" is determined by the concentration of a signaling protein CheY in the cytoplasm, which varies according to the concentration of the extracellular attractant that the cell is sensing. The cell will "tumble" less if it is moving in the favorable condition, and "tumble" more otherwise, to reorient themselves in the favorable direction

[45]. This biased random walk results in the bacteria moving toward regions with better conditions, a phenomenon commonly called chemotaxis.

In *E. coli*, the sensing and signaling network and its link to the CW/CCW bias has been well elucidated [6], [78], [104], [105]. In particular, in response to decreased attractant ligands binding to chemoreceptors clustered on the cell surface, the signaling protein CheA is activated for auto-phosphorylation, becoming CheA-P. CheA-P in turn phosphorylates two response regulator proteins, CheY and CheB [50]. The phosphorylated CheY, CheY-P, is released from the cluster and diffuses to the flagellar motor, where it binds to the motor proteins, FliM and FliN, causing a conformational change of the flagellar motor ring [37], [43]. This results in a switch of the rotational direction of the motor ring from CCW to CW [36], [51]. At the same time, the phosphorylated CheB, CheB-P, works antagonistically to CheR, which increases the ability of the chemoreceptors to activate CheA [50]. This serves as a primitive memory to reset the signaling sensitivity to the time-averaged ligand concentration in the recent past.

However, such molecular mechanisms of chemotaxis have not been established for other bacterial species. In particular, it is still not clear how monotrichous bacteria such as *P. aeruginosa* undergo chemotaxis. Due to it having only a single motor and a single flagellum, the monotrichous bacterium's CCW and CW rotation results in forward and backward movement, respectively. There has been some previous work on the motility of several monotrichous species. For example, it was found that the sodium-

driven marine bacteria, *Vibrio alginolyticus*, executes a cyclic three-step "run-reverse-flick" swimming pattern [57]. The flick has also been later shown to be due to the instability of the flagellar bucking [61]. There has also been studies about the varying "run-and-stop" mechanism in monotrichous *Rhodobacter sphaeroides* [60], [81]. In a previous study [79], we have shown that *P. aeruginosa* can remain stationary for short periods of time, leading to the existence of a pause phase of the flagellar motor, during which the cell body turns. Thus, we suggested a "run-reverse-turn" paradigm for the motility of monotrichous species. However, the chemosensory system of *P. aeruginosa* is more complex than *E. coli* or other species: For example, while *E. coli* has only one gene cluster with 5 methyl-accepting chemotaxis proteins (MCPs) and 6 chemotaxis (*che*) genes [63], *P. aeruginosa* has 4 gene clusters involved in chemotaxis, with 26 methyl-accepting chemotaxis proteins (MCPs) and 20 chemotaxis (*che*) genes [64]. Among these gene sets, one (PA408-PA417) is involved in the pili-mediated twitching motility [65], [66], one is believed to control biofilm formation [67], [68], and the remaining two sets, *che* and *che2*, are similar to their *E. coli* counterparts and regulate flagella-mediate chemotaxis [69]. Therefore there is *cheY* and there is *cheY2*. Although homologues to the *cheY* gene in *E. coli*, the cheY2 gene only shares 35% identical amino acid compared with *cheY* gene's 58%. The over-experession and complementation data of CheY2 does not alter chemotaxis function, suggesting that unlike CheY, the CheY2 protein does not interact with the flagellar motor [106]. Besides chemoreceptors located on the cell

surface, *P. aeruginosa* also possesses cytoplasmic chemoreceptors [70]. It is still unclear how this complex set of proteins function to regulate chemotaxis.

In this paper, we subjected tethered *P. aeruginosa* cells to a chemoattractant stimulus and measured the durations of the CW/CCW rotations, using a previously developed tethering analysis program [79]. We found that, in response to the chemoattractant stimulus, *P. aeruginosa* cells prolonged the durations of their rotations, regardless of whether they are CCW or CW. In other words, the cells may be "running" (CCW rotation) or "reversing" (CW rotation), but upon sensing an increased gradient of the chemoattractant, the running or reversing is prolonged, resulting in prolonged swimming up the chemoattractant gradient. We term this chemotactic response "rectified run-and-reverse." Moreover, we also showed that such a response is modulated through the CheY protein (which is homologous to CheY in *E. coli*). However, the response of the motor to CheY-P in *P. aeruginosa* is very different from that in *E. coli:* In *E. coli*, CheY-P binding to the motor promotes CW rotation whereas unbinding promotes CCW rotation. In contrast, in *P. aeruginosa*, CheY-P binding to the motor can result in two opposite outcomes – either promoting CW rotation like in *E. coli*, or promoting CCW rotation (i.e., demoting CW rotation). The outcome is likely to depend on a short memory on the motor's rotation. Based on these observations, we proposed a potential mechanism for the CheY-motor interaction and built a quantitative model of *P. aeruginosa*'s chemotactic response.

4.2 Materials & Methods

4.2.1 Growth condition

Pseudomonas aeruginosa PA01 wild-type and *cheY* cells from single colonies were separately cultured overnight in 5 ml Luria-Bertani (LB) broth (BD Biosciences) at 37℃, 250 rpm. Cultures were diluted to $O.D._{600}$ = 0.2 using M9 media (MP Biomedicals) and grown at 37℃, 250 rpm until the cells reach the late-exponential growth phase. Cell cultures were then diluted 1:10 prior to imaging using video microscopy.

4.2.2 Cell tethering & video capture

The cell tethering protocol and video capture process is the same as in Section 3.2.2, except that the media used was M9 motility media (MP Biomedicals) instead of LB. Only cells with smooth and continuous rotations were extracted from videos for following processing and analysis.

4.2.3 Chemotaxis experiments

A tube with a hollow steep tip was used to connect the cell chamber with the syringe filled with the chemical to be injected (10 mM serine, etc). Two holes were punched into the PDMS layer and the tube was inserted into one of the holes. For the chemotaxis experiment, a constant flow of 5 μl/min was applied for 2 seconds using a syringe pump (Chemyx Inc.). Cells were visualized using an inverted microscope (Nikon Ti-U) under a 40x objective. Videos of tethered bacteria were taken at 120 frames per second (fps) for 1 to

5 minutes using a complementary metal-oxide semiconductor (CMOS) camera (Thorlabs; DCC1645). Following the convention, cells are considered to be rotating CW/CCW when viewed from the medium that they are tethered in [79].

4.2.4 Image processing of tethered cells

Image processing is the same as in Section 3.2.4 and also in [79].

4.3 Results

4.3.1 *P. aeruginosa* chemotaxis protein CheY regulates CCW/CW rotation durations but not the speed nor pause duration

Due to the symmetry of *P. aeruginosa*'s CCW and CW rotations (corresponding to forward and backward movements of the cell, respectively), the "run-and-tumble" mechanism as proposed for *E. coli* does not apply. Consequently, there must be other mechanisms to generate biased swimming in order for chemotaxis to occur. For example, there could be the following three possibilities: (1) Make use of the pause phase in a fashion similar to tumbling in *E. coli*: Because we have previously shown that the duration of a cell's pause is positively correlated with the angle of the cell turning [79], the cell can have less frequent pauses and/or shorter pauses when it moves towards the favorable condition (similar to less tumbling in *E. coli* moving towards a favorable condition), and vice versa, (2) Have the motor rotate more quickly when the cell moves towards the favorable condition and more slowly

otherwise, (3) Have the motor spin for a longer duration when the cell moves toward the favorable condition and shorter otherwise.

To determine which of these three possibilities actually occur in *P. aeruginosa*, we analyzed the rotation of tethered wild-type and the *cheY* mutant of *P. aeruginosa*. Bacterial flagella are shortened by shearing and tethered to a glass slide by antibodies. The rotation of the single motor is then observed as the rotation of the cell body, which can be recorded by an optical microscope and a digital camera (see Material and Methods). The *cheY* mutant has a deletion of the *cheY* gene, a gene homologous to the *cheY* gene in *E. coli*, and does not undergo chemotaxis [89].

First, we found that possibility (1) is unlikely because we did not find the pause phase to exhibit significant differences in both its duration and frequency between the wild-type and *cheY* mutant (Figure 4.1, A and B). This suggested that the pause phase is unlikely to be directly controlled by the chemotaxis protein CheY. Next, we found that possibility (2) is also unlikely because the average speed of both the CW and CCW rotations were not significantly different between the wild-type and *cheY* mutant (Figure 4.1 C). Again, this suggested that although the rotational speeds of individual cells may vary, the chemotaxis network does not directly regulate the rotational speeds. Finally, we found that possibility (3) is likely. The average durations of both the CW and CCW rotations in the *cheY* mutant were significantly longer than those of the wild-type (Figure 4.1 D) and subsequently with lower

frequencies (Figure 4.1 E). This difference suggested that the chemotaxis network regulates the rotation durations.

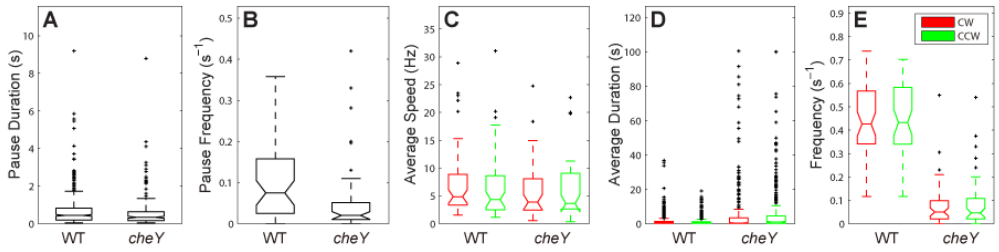

Figure 4.1 Rotation profiles of the wild-type and the *cheY* mutant

Each measure is plotted in box-plot. On each box, the central mark is the median, the edge of the box are the 25th and 75th percentiles, the whiskers extend to the most extreme data points not considered outliers, and outliners are plotted individually as small black crosses. (A) The average pause duration in wild-type (WT) (0.8 s) and *cheY* mutant (0.75 s) (t-test p-value = 0.55). (B) The average pause frequency in WT (1.20 s^{-1}) and *cheY* (1.22 s^{-1}) mutant (p-value = 0.08). (C) The average speeds of CW/CCW rotations in WT (6.22/5.28 Hz for CW/CCW, respectively) and *cheY* mutant (7.35/7.73 Hz for CW/CCW, respectively) (p-value of CW rotation between WT and *cheY* is 0.53; p-value of CCW rotation between WT is 0.17). (D) The average duration of CW/CCW rotations in WT (1.24/1.22 s) and *cheY* mutant (2.95/2.85 s) (p-value of CW rotations between WT and *cheY* $\ll$ 0.001; p-value of CCW rotations between WT and *cheY* $\ll$ 0.001). (E) The average CW and CCW frequency in WT (0.36/0.36 s^{-1} for CW and CCW, respectively) and *cheY* (0.1/0.1 s^{-1} for CW and CCW , respectively). (p-value of CW frequencies between WT and *cheY* $\ll$ 0.001; p-value of CCW frequencies between WT and *cheY* $\ll$ 0.001).

Red box denote CW, green CCW and black the pause phase. The maximum whisker length $w = 1.5$ and points are drawn as outliers if they are larger than $q_3 + w(q_3 - q_1)$ or smaller than $q_3 + w(q_3 - q_1)$, where q_1, q_3 are the 25th and 75th percentiles respectively. $w = 1.5$ corresponds to 99.3 coverage if the data are normally distributed. The rotational speed for each cell is calculated as the weighted average speed where the weights are the duration of a CW/CCW interval and respective speeds are the average speed of that interval. The average duration and average frequency bar graphs are created from the aggregate of all the interval durations among all the cells. The frequency is defined as numbers of events occur (CW, CCW or pause intervals) in a second. Error bars show one standard deviation. Data are taken from 45 wild-type cells and 36 *cheY* mutant cells respectively.

We note that, in *E. coli cheY* mutants, the absence of the CheY protein means that the bacteria lack phosphorylated CheY, CheY-P, to bind to the motors. Thus, the motors remain in the default CCW rotation continuously. This resulted in a lack of tumbling and hence inability for the mutants to undergo chemotaxis [36]. However, in the *P. aeruginosa cheY* mutants, we observed that the cells still spent roughly equal amounts of time in CW and CCW rotations (Figure 3.6). In addition, they also switch from CW to CCW and vice versa (Figure 3.6). Thus, while the *cheY* gene in *P. aeruginosa* is homologous to the *cheY* gene in *E. coli*, how it regulates chemotaxis is very different.

4.3.2 During chemotaxis, *P. aeruginosa* showed prolonged CW and CCW rotations that are adaptive

We introduced 10 mM serine as a chemoattractant after 120 s of observing the tethered cells in the M9 control buffer. We then compared the cells' rotation profiles before and after the addition of serine (Figure 4.2). In the control buffer, we saw a cell switching between CW and CCW rotations frequently and spending roughly equal amounts of time in either rotation (Figure 4.2 A and C). However, after the addition of serine, we saw that the rotation intervals were prolonged. Some cells exhibited a strong bias in the CCW rotations (Figure 4.2 *B*) while others exhibited a strong bias in the CW rotations (Figure 4.2 D). Thus, we hypothesize that if a cell happens to be rotating in the CW direction at the moment the chemoattractant is sensed, then the CW rotation is prolonged. Similarly, if the cell happens to be rotating in

the CCW direction at the moment the chemoattractant is sensed, then the CCW rotation is prolonged. This symmetry between the CW and CCW rotations is to be contrasted with the situation in *E. coli* where the cell runs in the CCW phase and tumbles in the CW phase.

Furthermore, the bias resulting from the prolonged rotations was most prominent immediately (in the first 30 s) after the addition of serine. It became reduced until the rotation profiles were similar to those observed before the addition of serine (Figure 4.2 B and D).

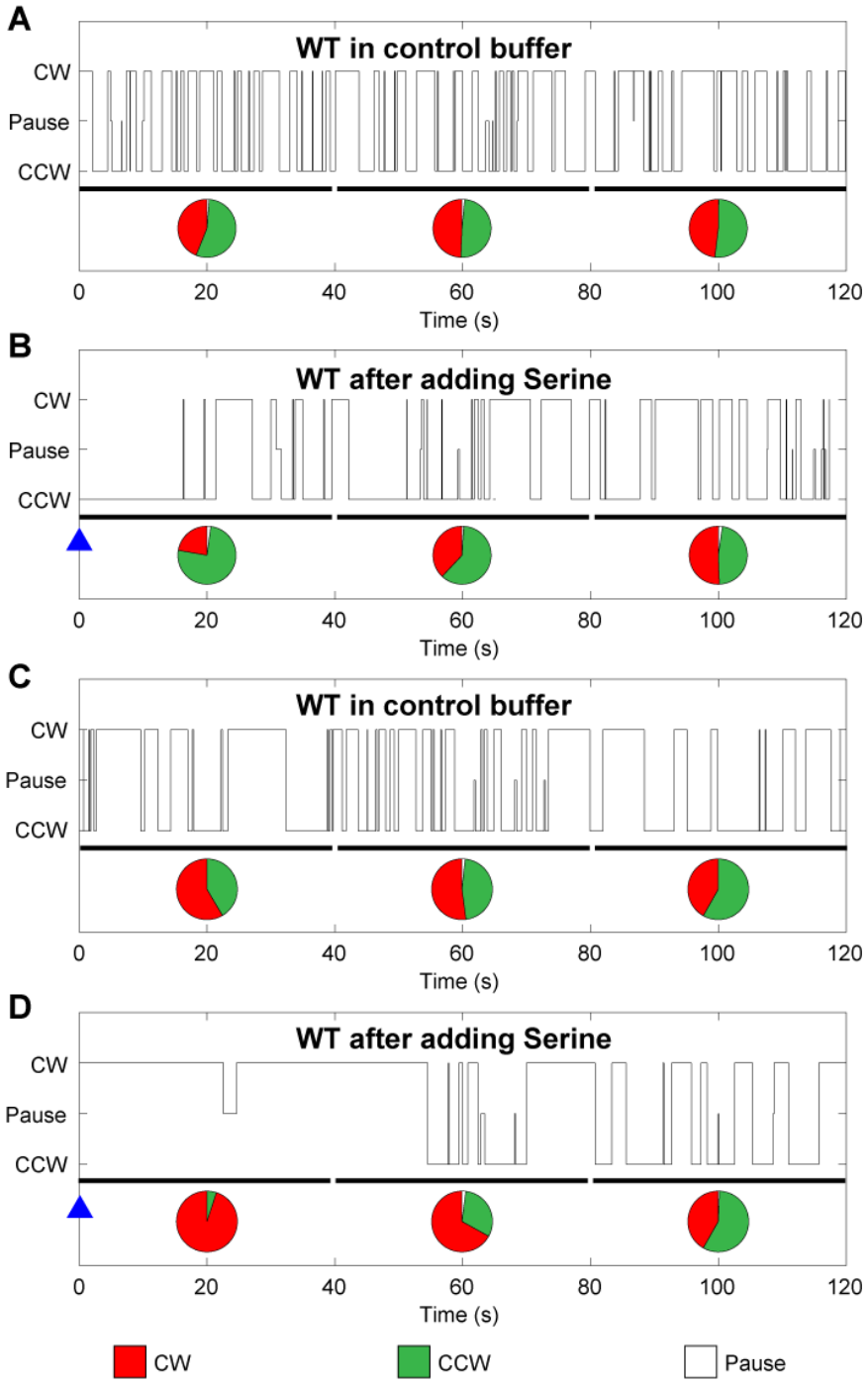

Figure 4.2 Samples of responses of wild-type *P. aeruginosa* cells before and after adding chemotaxis

(A) A sample time series of a wild-type P. aeruginosa cell in control condition. The percentage of CW and CCW are close. (B) The time series of the same *P. aeruginosa* cell as in (A) after adding chemo-attractant Serine at time 0 (blue triangle). The cell has a very long CCW for a period of time (high percentage of CCW) before adapts back to equal proportion. Insets: the percentage of

CW(red) /CCW(green) /pause(white) of every 40-seconds (thick bars at the bottom of the time series). In the control time series (A) the CW and CCW have similar percentages consistently; in the chemotactic time series (B) the CCW is strongly favored in the first 40 second, and the percentages start to adapt back to that of the control.

To study the prolonging of the rotation durations at the population level, we analyzed the rotations of 45 wild-type cells and 36 *cheY* mutant of *P. aeruginosa*. We found that, over a period of 120 seconds, the wild-type cells spent, on average, 45% ± 11% of their times in the CW state and the other 55% ± 11% in the CCW state. Furthermore, this CW percentage follows a normal distribution (Figure 4.3 A). However, for the first 30 seconds after the addition of the chemoattractant serine, the wild-type cells showed a very non-normal distribution of the amount of time spent in the CW state (Figure 4.3 B and F-J). In fact, the distribution is bimodal, showing high values at around 0% and around 100%. This suggests that, at the population level and for 30 seconds after the addition of the chemoattractant, the rotations are either all CW (100%) or CCW (0%). For subsequent periods of 30 second intervals, the distribution slowly adapted back to a normal distribution again, eventually peaking at 45% similar to that of the control group (Figure 4.3 C-E).

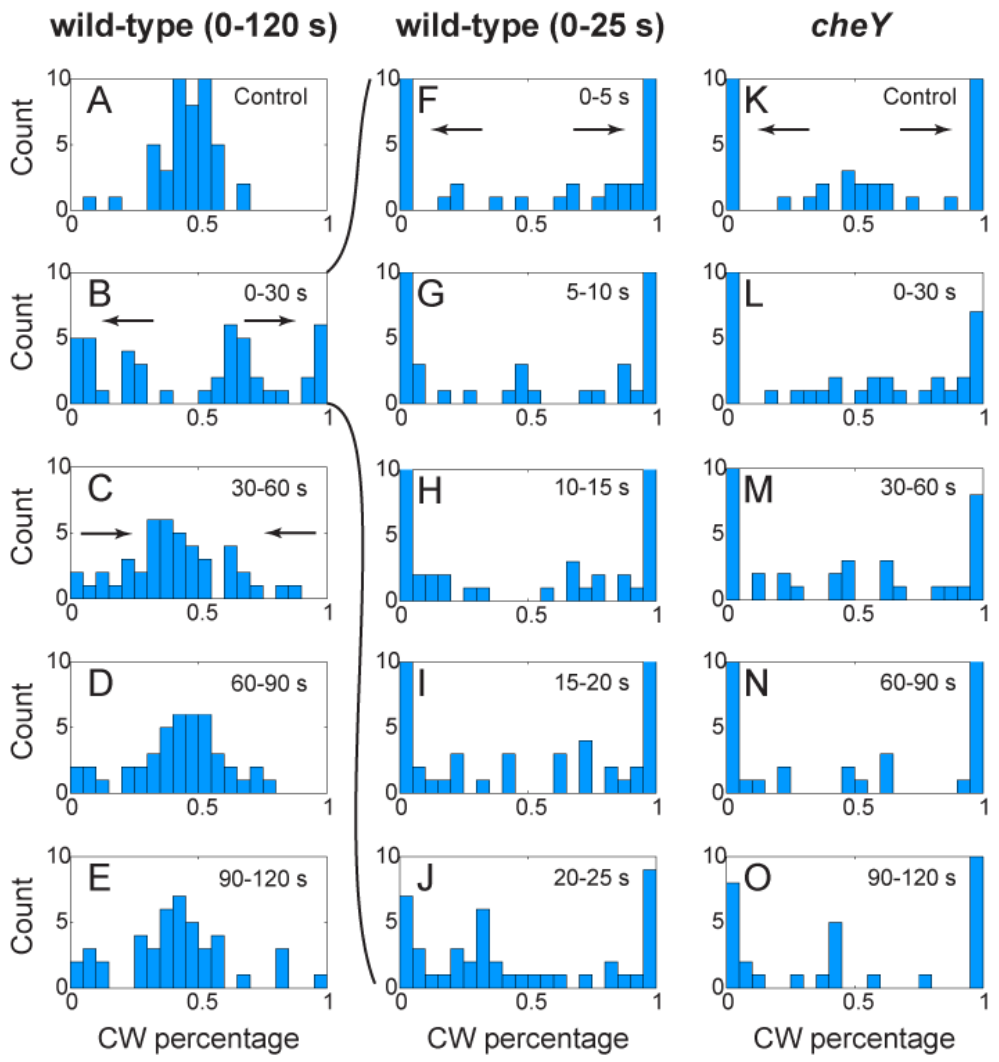

Figure 4.3 The distribution of the percentage of time spent in CW rotation the wild-type

(A-J) and the *cheY* mutant (K-O). (A) and (K) are control groups of wild-type cells and *cheY* cells, respectively, in M9 motility buffer for 120 s before adding chemoattractant serine. (B-E and L-O) are these distributions for every 30 s after adding the chemoattractant serine. (B and L: 0-30 s, C and M: 30-60 s, D and N: 60-90 s, E and O: 90-120 s). (F-J) are the distributions for every 5 s after adding the chemoattractant. Data are taken from 45 wild-type (A-J) cells and 36 *cheY* mutant (K-O) cells, respectively. Black arrows emphasize the split and merge of the peaks.

As *P. aeruginosa* has homologous chemotaxis genes as *E. coli* and the concentration of the CheY protein in *E. coli* is known to be down-regulated in response to increased chemoattractant concentration, we also tested whether

the rectified chemotactic response in *P. aeruginosa* were caused by the CheY protein. Thus, we repeated a similar analysis with the *cheY* mutant of *P. aeruginosa*. In M9 buffer without chemoattractants, the mutants exhibited a similarly skewed distribution of CW percentage with peaks at 0% (corresponding to all rotations being CCW) and 100% (corresponding to all rotations being CW) with no single normally distributed peak (Figure 4.3 K). This suggested that in the *cheY* mutants, the cells do not switch from CW to CCW rotations, and vice versa. More importantly, the addition of the chemoattractant serine did not alter the distribution (Figure 4.3 L-O), indicating that its absence does not affect the rotations of the motors. Thus, we concluded that the CheY protein is involved in linking the chemotaxis pathway to the rotation of the molecular motor. However, one key difference between the role of the CheY protein in *E. coli* and *P. aeruginosa* is that, in the former, CheY binding to the motor increases the probability of CW rotation (leading to more tumbling), whereas in the latter, CheY binding to the motor can lead to prolonged duration of CW or prolonged duration of CCW rotation, by reducing their respective switching frequencies to the opposite rotation direction (Figure 4.1 E).

4.3.3 A computational model of "rectified run-and-reverse"

E. coli takes advantage of an asymmetric outcome (run versus tumble) from the symmetric rotations (CCW versus CW) of the motors, due to the nature of the flagellar bundling. This, coupled with the sensing of the environment which resulted in biasing the frequency of tumbling versus

running, leads to chemotaxis (Figure 4.4 A). However, in *P. aeruginosa*, there is no such asymmetry to exploit, as the CW and CCW rotations of the motor lead to backward and forward movements, respectively. Consequently, there has to be an alternative mechanism to generate a bias in order for the cell to undergo chemotaxis. Our results so far indicated that the bias is generated by prolonging the rotation durations during chemotaxis. Thus, if the cell was rotating in the CCW direction (running forward) upon sensing the chemoattractant, then this CCW rotation is prolonged, leading to long runs and short reverses. Similarly, if the cell was rotating in the CW direction (running backward) upon sensing the chemoattractant, then this CW rotation is prolonged, leading to long reverses and short runs (Figure 4.4 B). We term this chemotactic response "rectified run-and-reverse". Furthermore, our results indicated that the CheY protein is necessary for this response.

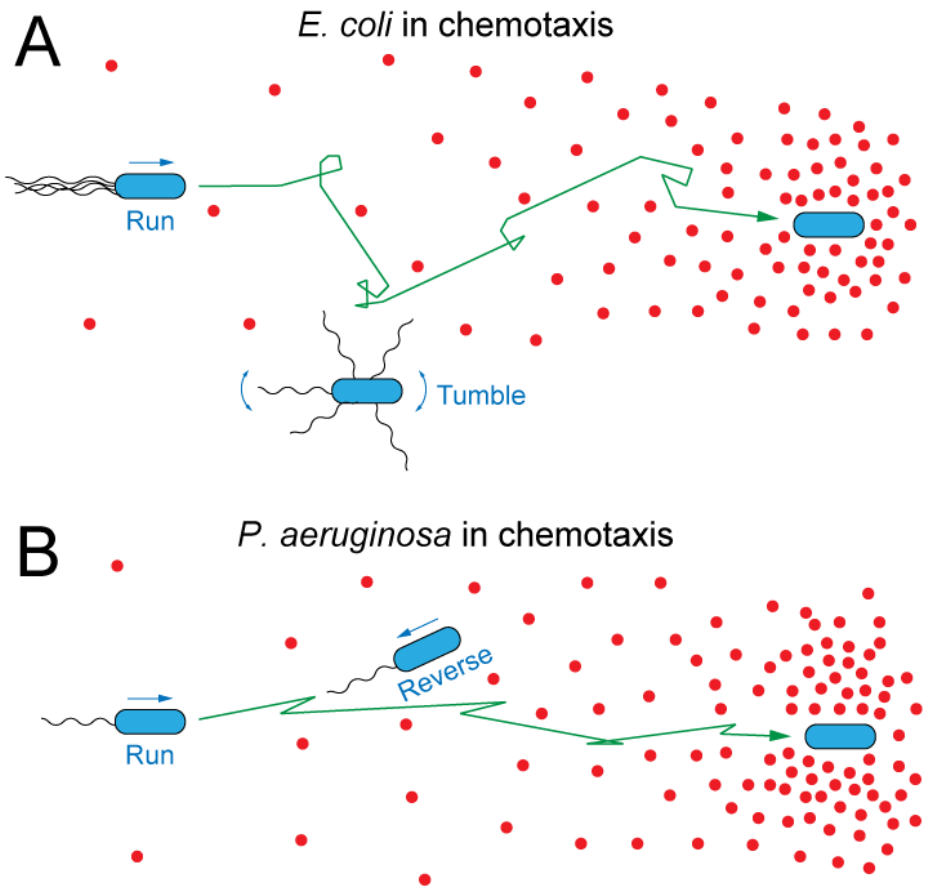

Figure 4.4 Schematic illustration of *E. coli* and *P. aeruginosa* in chemotaxis

(A) Illustration of the *E. coli*'s chemotaxis. The cell has a run-and-tumble strategy to move toward higher concentration. Red dots represent chemoattractant. (B) Illustration of the proposed *P. aeruginosa*'s chemotaxis. The cell can run or reverse its movement with smaller direction shift compared to *E. coli*'s tumbling, but the rectified durations on run and reverse migrate the cell toward higher concentration. Illustrations adapted from [107].

Previous research have shown that *P. aeruginosa* has two sets of sensory genes, *che* and *che2*, both involved in flagella-mediated chemotaxis [69]. We have demonstrated from our tethering experiments that the major component in the motor function control in *P. aeruginosa* is the CheY protein encoded from the gene set *che*. As *P. aeruginosa*'s *che* gene set is homologous to *E. coli*'s *che* gene set, we assumed that the signaling pathway upstream of

CheY that transduces the ligand concentration to CheY concentration and hence CheY concentration. CheY in *E. coli* binds to the flagellar motor and induces a bias in CCW rotation. This relationship has a high cooperativity with a Hill's coeffiencient close to 10 (Figure 4.5 *A* [7]). Based on our results from *P. aeruginosa*, we require that CheY-P binding to the motor protein upon sensing of chemoattractant to modify both the CW and CCW rotations in a symmetric way, and not just the CCW alone. Assuming that a cell in a chemoattractant gradient is moving up the gradient. It could be moving forward (propelled by a flagellum in CCW rotation) or be moving backward (dragged by a flagellum in CW rotation). In either case, the CheY-P concentration in the cell would be low due to the increased chemoattractant concentration in the environment. However, in the former case, the cell now would have to favor CCW rotation, so as to keep moving in the same direction (i.e., long run and short reverse). Therefore, the relation between the CheY-P concentration and the CW bias of the motor must follow a similar Hill's curve (Figure 4.5 B, blue curve); in the latter case, the cell now would have to favor CW rotation, so as to keep moving in the same direction (i.e., long reverse and short run). Therefore, the corresponding relation should follow an inverted shape of that in the former case (Figure 4.5 B, yellow curve). In other words, the cell must "memorize" whether the motor is rotating in the CCW or CW state, i.e., that the *P. aeruginosa* motor's response to CheY-P is dependent on the motor's current rotational state. If the current state is CCW, then the rotational response curve follows the blue curve in Figure 4.5 B; if the current

state is CW, then the rotational response curve follows the yellow curve in Figure 4.5 B.

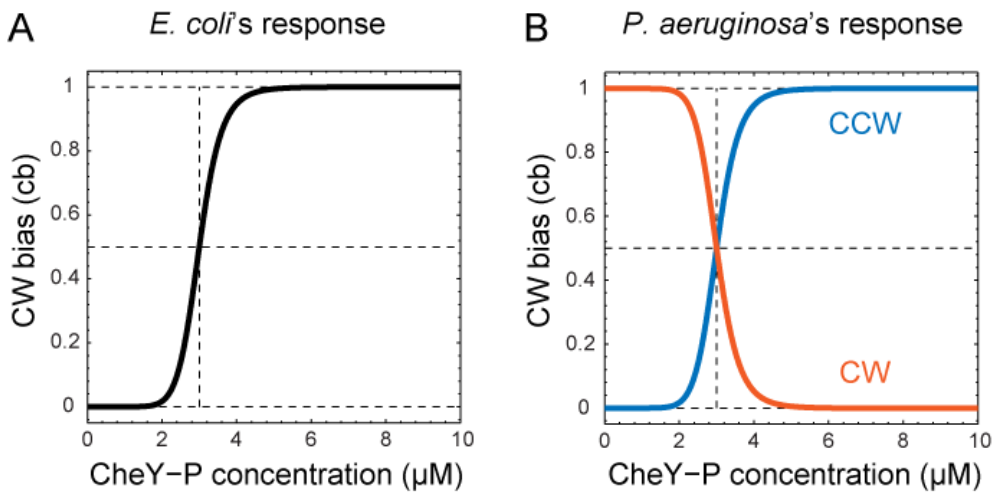

Figure 4.5 *E. coli*'s response curve to CheY-P and our proposed *P. aeruginosa*'s response curve

(A) The illustration of the response curve between the CW bias of the motor and the CheY-P protein in *E. coli* (Modified based on [7]). (B) The illustration of our hypothesized bi-states response curves between the CW bias of the motor and the concentration of the CheY-P protein in *P. aeruginosa.* The response curve is dependent on the current rotational state of the motor. If the current state is CCW, then the curve follows the blue curve; if the current state is CW, then the curve follows the yellow curve.

With these assumptions, we used computational simulation to examine the chemotaxis behavior of *P. aeruginosa*. For the signaling pathway upstream of CheY, we simply used the model previously proposed for *E. coli* [108]. In modeling the chemotaxis network, we used the similar mean field approach as previous research for *E. coli* [108]. The model can be simplified as in the schematic illustration (Figure 4.6). There are three variables in describing this chemotaxis network: the external ligand concentration L, the average CheA kinase activity A and the average methylation level of the receptor complex M.

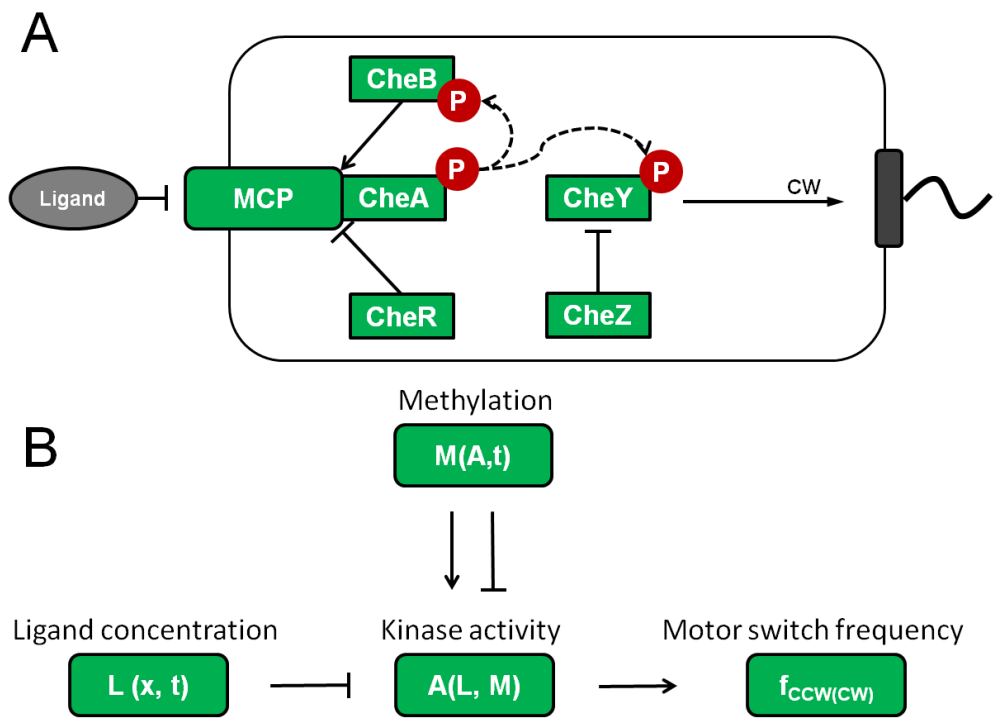

Figure 4.6 Diagram of the model in simulation

(A) The chemotaxis pathway. The MCP complex serves as the sensor of ligands and can be active (CheA-P) or inactive (CheA). CheA-P phosphorylates CheY and CheB. The former binds to the motor and alter its rotational states. CheZ dephosphorylates CheY-P. CheB-P and CheR methylates and demethylates the MCP respectively. (B) Diagram of the model. There are three dynamic variables, ligand concentration $L(\mathbf{x},\mathrm{t})$, kinase activity $A(L,M)$ and methylation level $M(A,t)$. The kinase activity determines the motor switch frequency and therefore the motion of bacteria.

During locomotion the external ligand concentration $L(\mathbf{x},\mathrm{t})$ is determined by the time t and the physical location of the bacteria cell $\mathbf{x}(t)$ in a chemotaxis gradient.

The simplest model to describe the kinase activity of a single chemo-receptor assumes that it has two states: one active and one inactive. Taken into account the receptor's ligand binding status, the state of a receptor can be

characterized by a variable pair (a,l) where $a=0,1$ representing the inactive and active states of the receptor respectively and $l=0,1$ representing the free and ligand-binding receptor respectively. The ligand dissociation coefficient of ligands binding to the active and inactive receptors are K_A and K_I (unit: μM). Without ligand binding, the dimensionless free energy between the active and inactive states of the receptor is only dependent on the methylation level, which can be written as $f_m(M)$. Note that $f_m(M)$ is a dimensionless energy related term normalized by k_BT, where k_B is the Boltzmann's constant and T the thermodynamic temperature. Therefore in equilibrium, the probability of each of the states $P(a,l)$ of a receptor has following relations:

$$\frac{P(0,1)}{P(0,0)}=\frac{[L]}{K_I},\ \frac{P(1,1)}{P(1,0)}=\frac{[L]}{K_A},\ \frac{P(0,0)}{P(1,0)}=e^{-f_m(M)} \tag{4.1}$$

where $[L]$ is the ligand concentration. Because $P(0,0)+P(1,0)+\mathrm{P}(0,1)+\mathrm{P}(1,1)=1$, from (4.1) we can derive the average probability of a receptor being active at steady-state:

$$\begin{aligned} A &= P(1,0)+P(1,1) \\ &= \frac{1+[L]/K_A}{1+[L]/K_A+e^{-f_m(M)}\left(1+[L]/K_I\right)} \\ &= \frac{1}{1+e^{-\left[f_m(M)+\ln\left(\frac{1+[L]/K_A}{1+[L]/K_I}\right)\right]}} \end{aligned} \tag{4.2}$$

As the kinase activity A only depends on the concentration of ligands L (unit: μM) and the relative methylation level M (unit: dimensionless) therefore it can be expressed as $A(L,M)$. The cooperativity among receptors can be described using the Monod-Wyman-Changeus (MWC) allosteric model [109], [110], which proposed a all-or-none coupling among all receptors in a cluster. The MWC model has been popular due to its simplicity and has been successful in describing the receptor system in *E. coli*. Therefore the average activity can be written based on (4.2):

$$\langle A \rangle = \frac{1}{1+e^{-N\cdot f(M,L)}} \tag{4.3}$$

where N is the number of receptors in a cluster unit and $f(M,L)$ is a dimensionless term associated with free energy difference of an individual receptor, dependent on its methylation level and ligand binding (see Table 1 for a summary of symbols and values used in the simulation). Note that the function of A is a dimensionless sigmoid type probability function with a range from 0 to 1, representing minimum and maximum activity respectively. Obviously from (4.2) and (4.3), we can split $f(M,L)$ into two dimensionless terms:

$$f(M,L) = f_m(M) + f_L(L) = f_m(M) + \ln\left(\frac{1+[\mathrm{L}]/K_A}{1+[\mathrm{L}]/K_I}\right) \tag{4.4}$$

where $f_m(M)$ is the same dimensionless term mentioned in (4.1) and (4.2) and $f_L(L)$ is a dimensionless term associated with ligand-dependent free energy difference. As we know higher level of methylation results in higher kinase activity, for simplicity we assume a linear relation $f_m(M) = \varepsilon_m(M - M_0)$. ε_m, M and M_0 are all dimensionless quantities where M_0 is the base methylation level. In the limit where $[L] \to 0$, results in zero kinase activity; where $[L] \to \infty$, $f_L(L)$ should reach a limiting number determined by the ratio of the two binding constant $\ln\left(\frac{K_I}{K_A}\right)$, which sets the boundary of the signal to which the system can respond sensitively. Here in the simulation we use $N = 6$, $\varepsilon_m = 1.7$, $M_0 = 1$, $K_A = 3\,\mu\text{M}$ and $K_I = 18.2$ μM [111].

Assuming that CheR and CheB binds to receptor complex independently, the process of the (de)methylation can be described by a linear approximation:

$$\frac{dM}{dt} = k_R(1 - A) - k_B A \tag{4.5}$$

where k_R and k_B are the rates (unit: s^{-1}) for methylation and demethylation respectively, with the assumption that CheR only binds to inactive kinase and CheB only binds to active kinase. Both M and A are dimensionless. For simplicity we used $k_R = k_B$ and fix the steady state activity level $A^* = 0.5$. The

methylation rates can be estimated by the adaptation time from experiments with a step chemo-stimuli [46]. We use $k_R = 0.005$/s for *E. coli* in MeAsp, and similarly $k_R \approx 0.015$ /s for *P. aeruginosa* in serine based on the estimation from our experiments in serine. The dimensionless methylation level M is integrated by Euler method:

$$M(t+dt) = M(t) + \left[k_R (1 - A(t)) - k_B A(t) \right] dt \qquad (4.6)$$

In the simulation we use $dt = 0.1$ s .

We used a simple phenomenological model to link the CheY to probability states of motor rotations. Define CW bias (cb) as:

$$cb = T_{CW} / (T_{CW} + T_{CCW}) \qquad (4.7)$$

where T_{CCW} and T_{CW} are the average duration of exponentially distributed CCW and CW states respectively. For *E. coli*, cb and T_{CCW} are functions of Y, the effective CheY-P concentration in the cell; T_{CW} is independent of Y according to experiments [48]. Therefore, in *E. coli* the frequency (unit: s^{-1}) of having a CCW→CW (tumble) switch can be expressed as:

$$f_{CW \to CCW}(Y) = 1/T_{CW} \qquad (4.8)$$

$$f_{CCW\to CW}(Y)=\frac{1}{T_{CCW}}=\frac{1}{T_{CW}}\cdot\frac{1}{\frac{T_{CCW}}{T_{CW}}}=\frac{1}{T_{CW}}\cdot\frac{1}{\frac{1}{cb(Y)}-1} \tag{4.9}$$

During chemotaxis, according to the measure response of the motor's bias to the CheY-P concentration Y:

$$cb(Y)=\left(1+\left(\frac{1}{cb_{1/2}}-1\right)\left(\frac{Y_{1/2}}{Y}\right)^{H}\right)^{-1} \tag{4.10}$$

where Y is the effective CheY-P concentration during chemotaxis with a unit of μM, $Y_{1/2}=3\,\mu\text{M}$ is that concentration estimated when $cb=cb_{1/2}=1/2$ measured from the response curve in experiments and $H=10$ is the estimated Hill's coefficient [7]. We assume that phosphorylated CheY-P Y is linear proportional to the kinase activity A:

$$Y=C_A\cdot A(L,M) \tag{4.11}$$

where C_A is a coefficient with unit of μM, Y has a unit of μM and A is dimensionless. In steady-state, it has been measured that $cb^*=T_{CW}/(T_{CW}+T_{CCW})\approx 0.2/(0.2+0.8)$ [45] and $A^*=0.5$, therefore C_A (unit: μM) can be estimated from Eq. (4.10) and Eq. (4.11)

$$C_A = \frac{Y^*}{A^*} = \frac{\dfrac{Y_{1/2}}{\left(\dfrac{\dfrac{1}{cb^*}-1}{\dfrac{1}{cb_{1/2}}-1}\right)^{1/H}}}{A^*} \tag{4.12}$$

In simulation, after each time step dt, the motor switch its rotation direction from the present state with the corresponding switching frequency $P_{CCW\to CW(CW\to CCW)} = f_{CCW\to CW(CW\to CCW)} \times dt$.

In *P. aeruginosa*, to gain population drift, we made an assumption that the CW bias depends on the previous rotation state before getting into chemotaxis. Therefore the cb-*cheY*-P relationship can be described by two Hill's curves:

$$cb(Y,s) = \left(1+\left(\frac{1}{cb_{1/2}}-1\right)\left(\frac{Y_{1/2}}{Y}\right)^H\right)^{-1}, s=-1 \tag{4.13}$$

$$cb(Y,s) = 1-\left(1+\left(\frac{1}{1-cb_{1/2}}-1\right)\left(\frac{Y_{1/2}}{Y}\right)^H\right)^{-1}, s=1 \tag{4.14}$$

where $s \in \{1,-1\}$ represent the CW and CCW states of a cell's motor and after each motor switch $s = s\cdot(-1)$. For simplicity we assume that during chemotaxis, although one of CW/CCW rotation will be favored, the sum of average durations of CW and CCW would be unchanged, i.e., $T_{CW} + T_{CCW} = \tau_0 = \langle T_{CW}\rangle + \langle T_{CCW}\rangle = 2.4\,\text{s}$, thus the motor switch frequency (unit: s^{-1}) can be calculated as:

$$f_{CW\to CCW}(Y)=\frac{1}{T_{CW}}=\frac{1}{\tau_0\cdot cb} \tag{4.15}$$

$$f_{CCW\to CW}(Y)=\frac{1}{T_{CCW}}=\frac{1}{\tau_0(1-cb)} \tag{4.16}$$

The swimming speeds of both *E. coli* and *P. aeruginosa* were set to be at a constant $v=20\,\mu$m/s for easy comparison, with their directions subjected to rotational diffusion - In the simulation after each time step dt, the moving direction of the cell changes by a stochastic angle $d\theta$, which follows a normal distribution:

$$d\theta\sim N\left(0,\sqrt{2D_r dt}\right) \tag{4.17}$$

where the rotational diffusion coefficient $D_r=0.062\,\text{rad}^2\ \text{s}^{-1}$ [5]. When a tumbling event happens for a *E. coli* cell, its tumbling angle is randomly distributed between $[-\pi,\pi]$ for simplicity and after a motor switch a *P. aeruginosa* cell changes its new moving direction θ' to be the opposite of its previous one ($\theta,\theta'=\theta+\pi$) with an additional angle variation $d\theta$ by the rotational diffusion similar to that in *E. coli*.

Table 1 Parameters used in the simulation

Simulation of *E. coli*

Constants	Description	Value	Reference

N	Number of receptors in a cluster	6	[108]
K_I	Dissociation coefficient of ligand binding to inactive receptor	18.2 μM	[111]
K_A	Dissociation coefficient of ligand binding to active receptor	3 mM	[111]
ϵ	Linear constant for methylation energy difference	1.7	[111]
M_0	Base methylation level	1	[111]
A*	Steady-state kinase activity	0.5	[111]
k_R	Methylation rate for *E. coli*	0.005 /s	[111]
k_B	Demethylation rate for *E. coli*	0.005 /s	[111]
$cb_{1/2}$	CW bias. This is a referencing CW bias point	0.5	[7]
$Y_{1/2}$	CheY-P concentration if CW bias is cb_0	3 μM	[7]
H	Hill's coefficient of CheY-P-cb curve	10	[7]
cb*	Steady-state CW bias in *E. coli*	0.2	[45]
D_r	Rotational diffusion coefficient	0.062 rad^2s^{-1}	[5]

Simulation of *P. aeruginosa*

Constants	Description	Value	Reference
N	Number of receptors in a cluster	6	[108]

K_I	Dissociation coefficient of ligand binding to inactive receptor	18.2 μM	[111]
K_A	Dissociation coefficient of ligand binding to active receptor	3 mM	[111]
ϵ	Linear constant for methylation energy difference	1.7	[111]
M_0	Base methylation level	1	[111]
A*	Steady-state kinase activity	0.5	Assumption
k_R	Methylation rate for *P. aeruginosa*	0.015 /s	This work
k_B	Demethylation rate for *P. aeruginosa*	0.015 /s	This work
$cb_{1/2}$	CW bias. This is a referencing CW bias point	0.5	[7]
$Y_{1/2}$	CheY-P concentration if CW biase is cb_0	3 μM	[7]
H	Hill's coefficient of CheY-P-cb curve	10	[7]
cb*	Steady-state CW bias in *P. aeruginosa*	0.5	This work
D_r	Rotational diffusion coefficient	0.062 rad^2s^{-1}	[5]

Using this model, we simulated four scenarios: *E. coli* in an environment without chemoattractant (blank control) (Figure 4.7 A and C) and in a linear chemoattractant gradient (Figure 4.7 B and D), and *P. aeruginosa* in an environment without chemoattractant (Figure 4.7 E and G) and in a linear chemoattractant gradient (Figure 4.7 F and H). In the blank control, both *E. coli* and *P. aeruginosa* showed random movements without any preference in particular directions. This is more clearly seen by calculating the population drift, defined to be the net distance moved in the direction of the chemoattractant gradient, averaged over all cells. It was close to zero (Figure

4.7 A and E, insets). In the linear chemoattractant gradient scenarios, the "run-and-tumble" *E. coli* climbed up the gradient as demonstrated by the general rightward movements of the individual cell trajectories (Figure 4.7 B). Furthermore, the population drift was positive (≈ 100 μm/min, Figure 4.7 B, inset). Similarly, the "rectified run-and-reverse" *P. aeruginosa* also climbed up the gradient, and the population drift was positive also (≈ 30 μm/min, Figure 4.7 F and inset). However, due to the "tumbling" events, *E. coli* cells changed swimming direction with larger variations (Figure 4.7 C and D). In contrast, *P. aeruginosa* cells could not tumble and the switching of the rotation from CCW to CW, or vice versa, resulted in the cells switching from running forward to running backward (reversing), or vice versa. The orientation changes during these switching events were not as large as those in *E. coli* (Figure 4.7 G and H). This was also reflected in the average population drift distance, where we saw that *E. coli* tended to have a more efficient chemotactic movement than *P. aeruginosa* (100 μm/min vs. 30 μm/min). Nevertheless, the model and the simulation qualitatively proved that a "rectified run-and-reverse" mechanism in *P. aeruginosa* breaks the CW/CCW symmetry and allows for their biased movements in chemotactic environments.

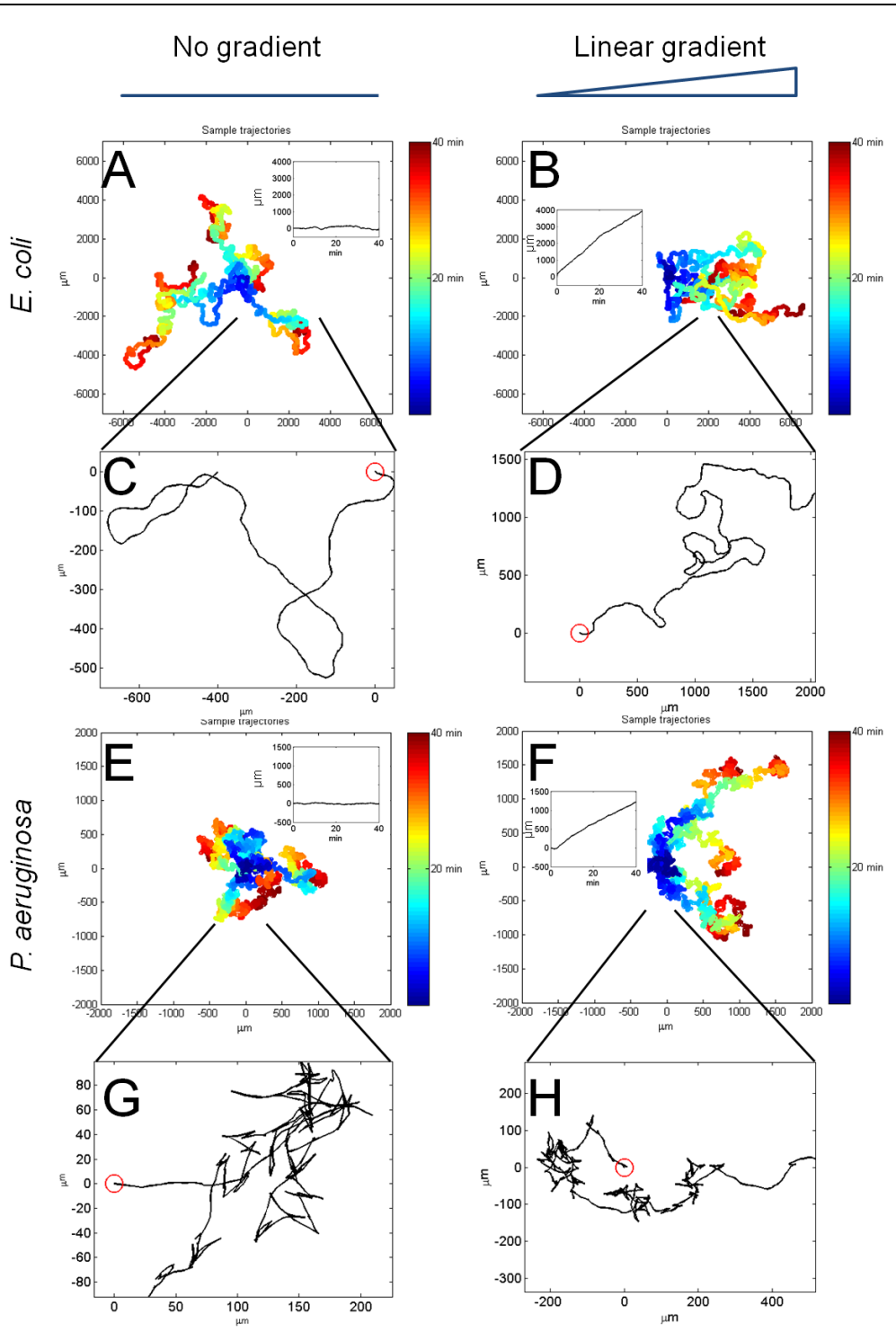

Figure 4.7 Simulation of *E. coli* and *P. aeruginosa* in chemotaxis

Five sample trajectories of a *E. coli* cell are presented moving in environment that (A) without chemical gradient and (B) with a linear gradient. Five sample trajectories of a P. aeruginosa cell moving in environment that (E) without chemical gradient and (F) with a linear gradient. (C, D, G, and H) are the detail of a sample trajectory taken from (A, B, E, and F) respectively, where

the red circle marks the starting location. The color codes the simulation time for each cell according to the color bar. The insets in (A, B, E, and F) show the average chemotactic drift distance (displacement along the gradient. In all four cases, rightward) of 100 simulated cells in same conditions. Both cases of *E. coli* and P. aeruginosa in chemotaxis show strong chemotactic drift (*E. coli* ≈ 4000 μm and P. aeruginosa ≈ 1200 μm after 40 min), and both cases of *E. coli* and P. aeruginosa without chemogradient show chemotactic drift close to zero. All simulated cells are started at location (0, 0) and simulation time is 40 min. The linear gradient increases at 10 μM/100 μm rightward.

4.3.4 Discussion

Compared to peritrichous bacteria such as *E. coli*, monotrichous bacteria such as *P. aeruginosa* enjoy the savings of energy in flagellar biosynthesis. However this energetic cost reduction is offset by the inability to reorient to explore the environment. Although an *E. coli* cell can induce tumbling, by disrupting the rotating bundle from the reversal of the motor, to largely change its swimming direction, monotrichous bacteria such as *P. aeruginosa* cannot reorient by simple reversal of the motor. Different monotrichous species have evolved different mechanisms to overcome this problem. For example, the marine monotrichous bacterium *Vibrio alginolyticus* is likely to adopt a "turning-by-buckling" mechanism [61] to vary its turning angles: at the onset of a forward swimming of the bacteria cell, the flexible hook at the base of the flagellum undergoes compression and buckles, resulting in reorientation of its swimming direction. It has also been suggested that a similar mechanism is also found in other fast-swimming marine bacteria such as *Pseudoalteromonas haloplanktis* [112] or *Vibrio coralliilyticus* [113]. In a previous study, we have also shown that *P. aeruginosa*'s motor has a novel 'pause' state aside of CW and CCW states.

The duration of the pause correlates with the size of turning angles when the bacteria swim, suggesting that the monotrichous bacteria may exploit pause as a mean to increase degrees of freedom during swimming. However, it is still unclear how these various mechanisms in creating larger turning angles can be regulated to achieve chemotaxis. In fact, as discussed earlier, the pauses in *P. aeruginosa* trajectories were shown to be not involved in chemotaxis (Figure 4.1 A and B). Thus, it is unlikely that the reorientation due to rotational diffusion during the pauses (the "turn" phase in the "run-reverse-turn" model) is involved in *P. aeruginosa* chemotaxis. Instead, we have shown that *P. aeruginosa* moves toward a particular direction, upon sensing a chemoattractant gradient, by rectifying the phase of the flagellar rotation that favors it continuing to move along that direction. We have also proposed a molecular-level model by homology with a similar model proposed for *E. coli*, and showed that we can reproduce realistic swimming trajectories. Furthermore, by setting the moving speed of the simulated *E. coli* and *P. aeruginosa* to be the same 20 μM/s, we can compare the efficiency of their chemotaxis strategies. We define the population drift as the average net displacement of cells in the direction of the chemoattractant gradient. We found that *E. coli* can achieve a more efficient population drift of ≈100 μm/min, compared to a value of ≈30 μm/min for *P. aeruginosa*, in a gradient of 10 μM/100 μm. Thus, we may say that the "run-and-tumble" strategy adopted by *E. coli* is more efficient than the "rectified run-and-reverse" strategy adopted by *P. aeruginosa*. This is perhaps a trade-off for

monotrichous bacteria during evolution as a compensation for the energy saving in flagella synthesis.

The exact mechanism of the CheY-motor interaction in *P. aeruginosa* is still unknown. Previous studies in *E. coli* have shown that the cooperative relationship between the phosphorylated CheY and the motor protein (Figure 4.5 A) can be explained by the conformational spread model [37], [43]. The model states that the FliN protein in the rotor adopts two conformational configurations, corresponding to the CW and CCW rotations. The FliN protein without CheY-P binding favors the CCW configuration and therefore the motor rotates in CCW state in the absence of CheY-P binding, i.e., without any response to chemoattractant sensing. The binding of CheY-P to the ring protein changes the energy landscape and favors the CW configuration. The neighboring FliN proteins tend to adopt the same configuration because homogenous configured proteins neighbors have lower free energy. As a result, the CW configuration "spreads" to the whole ring and the motor rotates in the CW state (Figure 4.8 A).

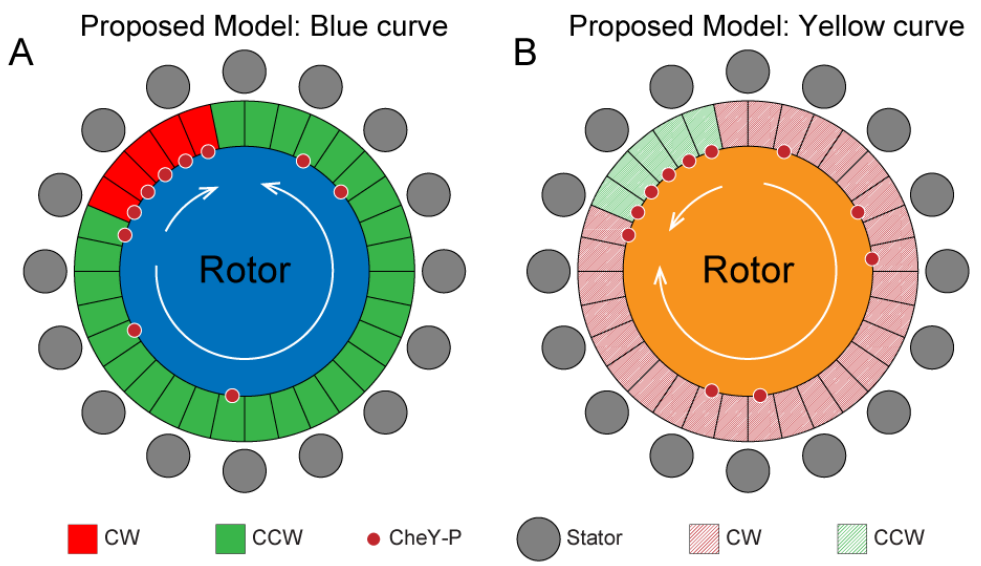

Figure 4.8 Illustrations of the molecular mechanism of the motor rotation

Both (A) and (B) shows schematic top views of the molecular motor. The outer gray circles are stators and the inner rings are conformations of the rotor. (A) The mechanism based on the blue curve in Figure 4.5 B. The FliM ring by default favors the conformation that leads to CCW rotation (solid green). CheY-P (red dots) binds to the FliM ring proteins and changes the energy landscape so that the bound FliM protein favors the conformation that leads to CW rotation (solid red). The conformation will spread or collapse depending on the adjacent energy penalty describe in the model in a stochastic way. (B) The mechanism based on the yellow curve in Figure 4.5 B. A mechanism that label (either by conformational change or another protein binding) the rotational state of the motor (shaded red/green) that shift the energy landscape of Che-P binding to the conformation of FliM proteins. The labeled FliM proteins by default favor the conformation that leads to CW rotation (shaded red). The CheY-P binding to the labeled FliM protein change its conformation which leads to CCW rotation (shaded green). Illustrations adapted from [114]

However in *P. aeruginosa* the response curves are dependent on the rotational state of the motor (Figure 4.8 B). At the molecular level, one way that this response can be implemented is by assuming that the binding of CheY-P to the FliN motor protein leads to two potential outcomes: if the current motor state were in CW then the energy landscape of configurations is similar to that in *E. coli* (Figure 4.5 A), but if the current motor state were in CCW then the FliN proteins reverse their energy landscape such that binding

of CheY-P leads to CCW rotation (Figure 4.8 B). This implements a short-term memory of the motor's rotation state. The characteristic time of the state-dependence is likely to be longer than the binding/unbinding of the CheY-P to the FliN protein, but shorter than the characteristic time of adaptation through methylation.

5 CONCLUSION

5.1 Bacterial tethering analysis program (BTAP) reveals "run-reverse-turn" mechanism for *Pseudomonas* spp. motility

The overall purpose of this research was to study the motor properties of monotrichous *P. aeruginosa* and to elucidate its controlling mechanism of the motor in a changing micro-environment in order to achieve motility and chemotaxis. This thesis proposed a new method and computational tool to analyze the tethering data of motor rotations in monotrichous bacteria and proposed a run-reverse-turn motion pattern for *P. aeruginosa* motility.

The first major result of the thesis was a new method together with the computational tool – Bacterial Tethering Analysis Program (BTAP) – with an improved accuracy and stability to analyze the tethered rotational behavior of monotrichous bacteria. Unlike the tethering data collected from the commonly used tethering protocols in peritrichous bacteria such as *E. coli*, the data from monotrichous bacteria were not satisfactory because the polar-located flagellum and flexible hook together resulted in unstable rotations. BTAP, compared with other methods and tools, has several advantages. First, it reduces the positional noise of the tethered cell bodies by automatic correction to the actual rotational axis. Secondly, the noisy spikes in the curve of instantaneous rotational speed are further smoothed out by the piecewise linear fitting from the accumulative revolution curve. Thirdly, the transition of the

rotational phases can be easily spotted from BTAP than from the previous moving average method, which needs to balance between the moving average smoothness and the loss of precision in phase transitions. BTAP is an open-source tool available online and it could help researchers in rendering credible results in analyzing images and data in the research of monotrichous bacteria.

The second major result of the thesis was the proposal of a run-reverse-turn mechanism in the *P. aeruginosa*. By using BTAP, we were able to study some of the novel properties of *P. aeruginosa*'s rotary motor in a high-throughput manner. First, it was discovered that the *P. aeruginosa* motor spent roughly equal time in counterclockwise (CCW) and clockwise (CW) rotation, which corroborated with some of the early reports in the free-swimming studies [56]. Secondly, the average speeds in both CCW and CW phase were close, indicating symmetry in the molecular rotor dynamics. Moreover a pause phase was identified from the data which accounted for 10-20% of the motor behaviors. As there was a positive correlation between the turn angles and durations of the turning events from 2D swimming data, it was therefore proposed that the pause phase allows the cell to reorient with a larger than normal angle, which effectively boosts its efficiency in exploring the space. There have been different models proposed for polar-flagellated bacteria to overcome their limitation in degree of freedom while moving. The run-reverse-turn model proposed in this thesis added another possibility of the moving pattern in nature.

5.2 Experiments and computational modeling reveal a rectified run-and-reverse mechanism for *P. aeruginosa* chemotaxis

In the thesis we have analyzed *P. aeruginosa*'s response in chemotaxis using previously developed tethering analysis program [79] and found that upon receiving an increasing concentration of chemoattractant stimulus, *P. aeruginosa* prolonged either its CW or CCW rotation durations by reducing the frequency of switching. In chemotaxis, although the difference of the average durations between CW and CCW rotations was not significant, in individual cell the percentage of total durations of CW and CCW was strongly biased: the rotations were prolonged and are either all CW or all CCW. We further showed that this process was most likely modulated through signaling protein CheY. As CCW and CW rotations in monotrichous *P. aeruginosa* correspond to forward and backward movement of the cell respectively, we term this response in chemotaxis "rectified run-and-reverse". This was very different from the known chemotaxis interactions between the homologous protein CheY and the molecular motor in *E. coli*, that the decreased concentration of CheY-P, caused by an increasing chemoattractant concentration, results in prolonged CCW duration and its high percentage versus CW rotations only.

Assuming that the upstream chemotaxis pathways of CheY in *E. coli* and *P. aeruginosa* are similar, we simulated this "rectified run-and-reverse" response following previous established models for *E. coli*'s. In addition we

hypothesized that the rectified CW and CCW rotation response is state-dependent based on a short memory of the motor's rotation states. We demonstrated that in such conditions, the simulated *P. aeruginosa* cells exhibited chemotaxis movement in a linear chemoattractant gradient. To explain *P. aeruginosa*'s chemotactic response from the molecular level, we also proposed a potential mechanism for the CheY-motor interaction.

5.3 Limitations

There are also some limitations with methods proposed in this thesis.

First, all the rotational data from the motor were drawn from the tethering experiments described in Section 3.2. While the tethering method is commonly used among scientists due to its simplicity, it does not take into account the effect of the size of the cell body and its shape. The size of the cell body determines the rotational drag on the cell body, which affects the rotational speed of the motor [16], [99]. Since the load on the flagellar motor is associated with the shape of the cell body, the shape variation among individual cell bodies also accounts for the different rotational speed under the same condition. This is an intrinsic flaw of the tethering experiment because it is impossible to control the cell sizes and shapes to be identical, although one may synchronize the growth phase of the bacteria to keep the population as homogeneous as possible. However it should not change the statistics from the population study because one should assume that the bulk quantities such as the average rotational speed and phase percentages should reflect the

properties of the motor under different conditions if the population studied is big enough. Nevertheless, the lack of control on drag forces on the cell body may increase the variance of data collected, therefore render more noisy results.

Secondly, the tethering experiment and its results are valid in tracking a bacterium for long time, but it is hard to corroborate the results from a swimming tracking experiment. Also in the chemotaxis experiment we hypothesized the "rectified run-and-reverse" mechanism from the behavior of *P. aeruginosa*'s flagellar motor, but tracking (therefore verifying) for such behavior during swimming would require a long-time tracking (with many reversal events) in a temporal changing chemogradient. This was hard to achieve because the bacteria swim freely in the 3D space, and the focal plane depth of a normal microscope is not enough to capture the object's movement in the z-axis for long times. As a result of that usually only a very short fraction of a cell's trajectory could be recorded (with one or two reversal events). To solve the problem of 3D tracking, one can either track an individual cell for a long time using a moving stage adjusting its position to keep the cell within the focal plane [45], or track a group of cells using the hues from optical imaging [76], [115] which effectively increases the depth of the focal plane to a limited extend. Another approach would be to put the bacteria cells in a flat chamber so the z-dimension is reduced, thus the 3D tracking becomes effectively a quasi-2D tracking. The problem with this approach is the hydrodynamic boundary effect on the swimming bacteria

which alters their trajectories significantly [116]–[119]. The free-swimming tracking is a common limitation in this field as so far there have not been a satisfying method to track bacteria in 3D for long times in high throughput.

Thirdly, during the chemotaxis experiment the change of the concentration of chemoattractant was a step function. Due to limitations in our experimental platform we were not able to generate other precise chemical gradient profiles such as pulse function, exponential function or oscillation functions that had been applied to *E. coli* [6], [91]. In particular, tethered *E. coli* cells rotate for hours, even days [46], on which one can test complex concentration profiles with a single cell consistently. However, tethered *P. aeruginosa* cells from our experiments only rotate for few minutes before they stop rotating completely or detach from the tethered surface. This shortened the time window to deliver the chemical gradient to induce the chemotactic response. The dynamics of the motor would be better calibrated using varieties of chemical profiles.

Lastly, during modeling we linked the CheY protein to the flagellar motor and assumed that its dynamic in interacting with the motor is similar to its homologous protein of *E. coli* (i.e., a similar Hill's function). Although the simulation verified that this type of interactions indeed lead to chemotaxis, we could not measure the kinetics of such interaction like the others did in *E. coli* [7], due to the lack of available experimental platform established in *P. aeruginosa*.

5.4 Future work

Based on the experimental and computational results of this thesis, there are several potential areas worth exploring in the future about the motility and chemotaxis of *P. aeruginosa*.

5.4.1 Precise single-cell study of the molecular motor

Studies showed that there is large variability among individual bacteria [120]–[122]. This is due to the molecular fluctuation and adaptation nature of the system. A study from a population level therefore would results in enhanced noise, rendering the experimental results uninterpretable. It is therefore critical to examine closely how a single molecular motor operates in the monotrichous bacteria. The bead test has been applied in the *E. coli* experiment to allow precise control of the drag torque exerted on the motor [7] (by controlling the size of the bead) and has obtained good results [25], [77], [123]. More importantly, a fixed cell body allows directly measurement of the CheY-P concentration concurrently with the rotation response of the motor. However this test has not been applied to monotrichous bacteria because polar-flagellated bacteria, when tethered to a surface, have their rotational axis of flagella parallel to the surface they tethered, which results in the undistinguishable signal from the microscope. There has been demonstrations of using optical tweezers to anchor a bacterium's cell body in a 3D space [124], [125], it is therefore recommended to use the same technique to 'float' a monotrichous bacterium's cell body vertically in the 3D space for the bead

test, so one can directly measure the motor's behavior based on the CheY-P concentration and verify our hypothesis in live (Figure 4.5).

5.4.2 Long-time three dimensional tracking of *P. aeruginosa* cells in a chemo-gradient

Recent advance in holographic 3D tracking enabled researchers to track *P. aeruginosa* for a focal depth of a few hundred μm [126]. It is therefore possible to track *P. aeruginosa* bacteria with longer time so that the "rectified run-and-reverse" mechanism can be verified. An alternative approach would be to create a high viscosity environment so that the rotation of the flagellar motor would be slowed down, and so would a cell's moving speed, consequently limit the moving range of a *P. aeruginosa* cell to allow longer tracking.

5.4.3 Microfluidic channel assay to measure the bulk chemotaxis efficiency of *E. coli* and *P. aeruginosa*

Recent progress in microfluidic channel engineering has provided a way to measure the average chemotaxis efficiency [97]. It is therefore possible to construct a experiment with a stable chemical gradient to verify the chemotaxis efficiency simulated and predicted as shown in Figure 4.7. By changing the chemical concentration in the inlets (Figure 5.1 A), a linear gradient perpendicular to the main microchannel will be created and the chemotaxis efficient can be measured by the change of fluorescence intensities (Figure 5.1 B).

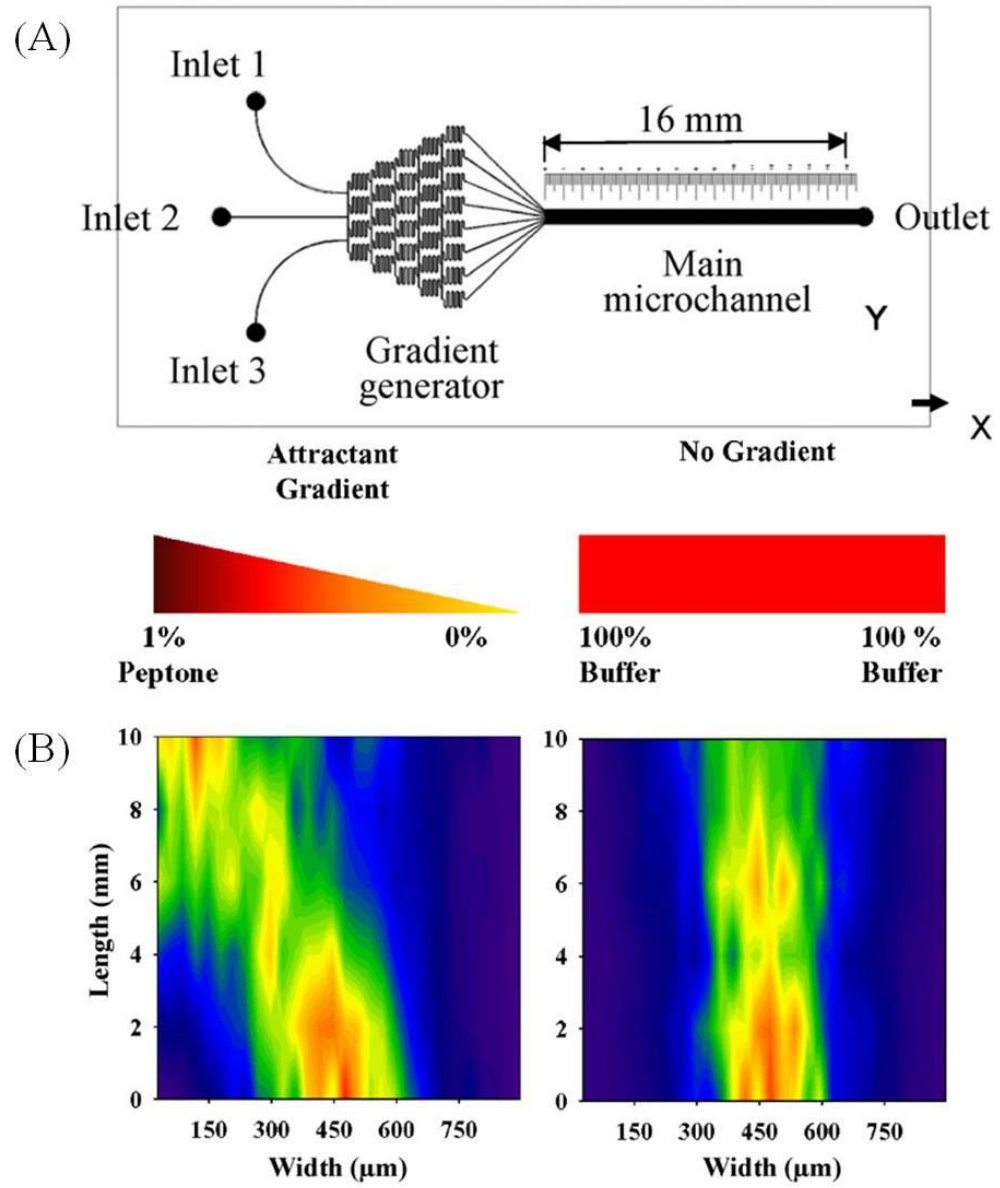

Figure 5.1 Illustrations of the microfluidic channel setting

(A) is the top view of the microfluidic device for the generation of a chemical gradient. It has three inlets, a gradient generator and a main microchannel for the measurement. (B) Example of response of *P. aeruginosa* PAO1 wild-type to the buffer (right) and attractant (left). The x axis is the dissection of the main microchannel while the y axis is the major axis of the main microchannel. The population density of the bacteria (heatmap) is obtained by the fluorescence intensities. Color bars on top represent the concentration gradient of attractant.[97]

5.4.4 Full modeling of *P. aeruginosa*'s motility, chemotaxis and biofilm formation

Thanks to decades of joint efforts, there has been a few complete *in silico* models for *E. coli* motility and chemotaxis [111], [127]. *P. aeruginosa* is known to have a more complex chemotaxis system with sets of genes [83] involved and distinctive motile patterns (swimming, swarming, and twitching). It is therefore tempting to build a full model based on the receptor kinetics, signaling pathways, and motor's responses of *P. aeruginosa*. Moreover, as an opportunistic pathogen, *P. aeruginosa* is heavily involved in the biofilm formation in nature. The motility and chemotaxis are critical for the dispersion of motile cells before forming a new colony, and its quorum sensing also plays important role in aggregation and initial attachment. The motility and chemotaxis model could be coupled with the measurement [128] and the models for biofilm formation [129]–[133].

6 BIBLIOGRAPHY

[1] E. M. Purcell, “Life at low Reynolds number,” *Am. J. Phys*, vol. 45, no. 1, pp. 3–11, 1977.

[2] H. C. Berg and R. A. Anderson, “Bacteria swim by rotating their flagellar filaments,” *Nature*, vol. 245, p. 380, 1973.

[3] H. C. Berg, *E. coli in Motion*. New York: Springer, 2003.

[4] H. C. Berg, “Motile behavior of bacteria,” *Phys. Today*, pp. 24–29, 2000.

[5] H. C. Berg, *Random walks in biology*. Princeton University Press, 1993.

[6] S. M. Block, J. E. Segall, and H. C. Berg, “Impulse responses in bacterial chemotaxis,” *Cell*, vol. 31, no. 1, pp. 215–226, Jul. 1982.

[7] P. Cluzel, M. G. Surette, and S. Leibler, “An ultrasensitive bacterial motor revealed by monitoring signaling proteins in single cells,” *Science*, vol. 287, no. 5458, pp. 1652–1655, Mar. 2000.

[8] S. F. Goldstein, N. W. Charon, and J. A. Kreiling, “Borrelia burgdorferi swims with a planar waveform similar to that of eukaryotic flagella.,” *Proc. Natl. Acad. Sci.*, vol. 91, no. April, pp. 3433–3437, 1994.

[9] I. R. Gibbons, “Cilia and flagella of eukaryotes.,” *J. Cell Biol.*, vol. 91, no. 3 Pt 2, p. 107s–124s, Dec. 1981.

[10] J. J. Blum and M. Hines, “Biophysics of flagellar motility.,” *Q. Rev. Biophys.*, vol. 12, no. 2, pp. 103–80, May 1979.

[11] H. C. Berg, “The rotary motor of bacterial flagella.,” *Annu. Rev. Biochem.*, vol. 72, pp. 19–54, Jan. 2003.

[12] L. Turner, W. S. Ryu, and H. C. Berg, “Real-time imaging of fluorescent flagellar filaments,” *J. Bacteriol.*, vol. 182, no. 10, p. 2793, 2000.

[13] E. Lauga and T. R. Powers, “The hydrodynamics of swimming microorganisms,” *Reports Prog. Phys.*, vol. 72, no. 9, p. 096601, Sep. 2009.

[14] G. Lowe, M. Meister, and H. C. Berg, “Rapid rotation of flagellar bundles in swimming bacteria,” *Nature*, vol. 325, no. 12, pp. 637–640, 1987.

[15] M. Kim, J. C. Bird, A. J. Van Parys, K. S. Breuer, and T. R. Powers, “A macroscopic scale model of bacterial flagellar bundling.,” *Proc. Natl. Acad. Sci. U. S. A.*, vol. 100, no. 26, pp. 15481–5, Dec. 2003.

[16] J. Xing, F. Bai, R. M. Berry, and G. Oster, “Torque–speed relationship of the bacterial flagellar motor,” *Proc. Natl. Acad. Sci. U. S. A.*, vol. 103, no. 5, 2006.

[17] H. C. Berg, “Dynamic properties of bacterial flagellar motors,” *Nature*, 1974.

[18] T. Ueno, K. Oosawa, and S.-I. Aizawa, “M ring, S ring and proximal rod of the flagellar basal body of Salmonella typhimurium are composed of subunits of a single protein, FliF,” *J. Mol. Biol.*, vol. 227, no. 3, pp. 672–7, Oct. 1992.

[19] T. Ueno, K. Oosawa, and S. Aizawa, “Domain Structures of the MS Ring Component Protein (FliF) of the Flagellar Basal Body of Salmonella typhimurium,” *J. Mol. Biol.*, 1994.

[20] T. F. Braun and D. F. Blair, “Targeted disulfide cross-linking of the MotB protein of Escherichia coli: evidence for two H(+) channels in the stator Complex.,” *Biochemistry*, vol. 40, no. 43, pp. 13051–9, Oct. 2001.

[21] I. H. Khan, T. S. Reese, and S. Khan, “The cytoplasmic component of the bacterial flagellar motor.,” *Proc. Natl. Acad. Sci. U. S. A.*, vol. 89, no. 13, pp. 5956–60, Jul. 1992.

[22] J. Zhou, S. a Lloyd, and D. F. Blair, “Electrostatic interactions between rotor and stator in the bacterial flagellar motor.,” *Proc. Natl. Acad. Sci. U. S. A.*, vol. 95, no. 11, pp. 6436–41, May 1998.

[23] S. A. Lloyd and D. F. Blair, “Charged residues of the rotor protein FliG essential for torque generation in the flagellar motor of Escherichia coli,” *J. Mol. Biol.*, vol. 266, no. 4, pp. 733–44, Mar. 1997.

[24] S. Kojima and D. F. Blair, “The bacterial flagellar motor: structure and function of a complex molecular machine.,” *Int. Rev. Cytol.*, vol. 233, pp. 93–134, Jan. 2004.

[25] C. V Gabel and H. C. Berg, “The speed of the flagellar rotary motor of Escherichia coli varies linearly with protonmotive force.,” *Proc. Natl. Acad. Sci. U. S. A.*, vol. 100, no. 15, pp. 8748–51, Jul. 2003.

[26] Y. Sowa, A. D. Rowe, M. C. Leake, T. Yakushi, M. Homma, A. Ishijima, and R. M. Berry, “Direct observation of steps in rotation of the bacterial flagellar motor.,” *Nature*, vol. 437, no. 7060, pp. 916–9, Oct. 2005.

[27] D. Walz and S. R. Caplan, “An electrostatic mechanism closely reproducing observed behavior in the bacterial flagellar motor.,” *Biophys. J.*, vol. 78, no. 2, pp. 626–51, Feb. 2000.

[28] R. Schmitt, “Helix rotation model of the flagellar rotary motor.,” *Biophys. J.*, vol. 85, no. 2, pp. 843–52, Aug. 2003.

[29] G. Meacci and Y. Tu, “Dynamics of the bacterial flagellar motor with multiple stators,” *Proc. Natl. Acad. Sci. U. S. A.*, vol. 106, no. 10, pp. 3746–51, Mar. 2009.

[30] T. Mora, H. Yu, Y. Sowa, and N. S. Wingreen, “Steps in the bacterial flagellar motor,” *PLoS Comput. Biol.*, vol. 5, no. 10, p. e1000540, Oct. 2009.

[31] F. Bai, C.-J. Lo, R. M. Berry, and J. Xing, “Model studies of the dynamics of bacterial flagellar motors.,” *Biophys. J.*, vol. 96, no. 8, pp. 3154–67, Apr. 2009.

[32] M. Silverman and M. I. Simon, “Flagellar rotation and the mechanism of bacterial motility,” *Nature*, vol. 249, pp. 73–74, 1974.

[33] S. Kudo, Y. Magariyama, and S.-I. Aizawa, “Abrupt changes in flagellar rotation observed by laser dark-field microscopy,” *Nature*, vol. 346, no. 16, pp. 677–680, 1990.

[34] S. Yamaguchi, S. Aizawa, M. Kihara, M. Isomura, C. J. Jones, and R. M. Macnab, “Genetic evidence for a switching and energy-transducing complex in the flagellar motor of Salmonella typhimurium.,” *J. Bacteriol.*, vol. 168, no. 3, pp. 1172–9, Dec. 1986.

[35] C. M. Dyer, A. S. Vartanian, H. Zhou, and F. W. Dahlquist, “A molecular mechanism of bacterial flagellar motor switching.,” *J. Mol. Biol.*, vol. 388, no. 1, pp. 71–84, Apr. 2009.

[36] M. K. Sarkar, K. Paul, and D. Blair, “Chemotaxis signaling protein CheY binds to the rotor protein FliN to control the direction of flagellar rotation in Escherichia coli,” *Proc. Natl. Acad. Sci. U. S. A.*, vol. 107, no. 20, pp. 9370–9375, May 2010.

[37] L. K. Lee, M. A. Ginsburg, C. Crovace, M. Donohoe, and D. Stock, “Structure of the torque ring of the flagellar motor and the molecular

basis for rotational switching," *Nature*, vol. 466, no. 7309, pp. 996–1000, Aug. 2010.

[38] S.-Y. Park, B. Lowder, A. M. Bilwes, D. F. Blair, and B. R. Crane, "Structure of FliM provides insight into assembly of the switch complex in the bacterial flagella motor.," *Proc. Natl. Acad. Sci. U. S. A.*, vol. 103, no. 32, pp. 11886–91, Aug. 2006.

[39] T. Minamino, K. Imada, M. Kinoshita, S. Nakamura, Y. V Morimoto, and K. Namba, "Structural insight into the rotational switching mechanism of the bacterial flagellar motor.," *PLoS Biol.*, vol. 9, no. 5, p. e1000616, May 2011.

[40] V. Sourjik and H. C. Berg, "Binding of the Escherichia coli response regulator CheY to its target measured in vivo by fluorescence resonance energy transfer.," *Proc. Natl. Acad. Sci. U. S. A.*, vol. 99, no. 20, pp. 12669–74, Oct. 2002.

[41] Y. Sagi, S. Khan, and M. Eisenbach, "Binding of the chemotaxis response regulator CheY to the isolated, intact switch complex of the bacterial flagellar motor: lack of cooperativity.," *J. Biol. Chem.*, vol. 278, no. 28, pp. 25867–71, Jul. 2003.

[42] T. A. Duke, N. Le Novère, and D. Bray, "Conformational spread in a ring of proteins: a stochastic approach to allostery.," *J. Mol. Biol.*, vol. 308, no. 3, pp. 541–53, May 2001.

[43] F. Bai, R. W. Branch, D. V Nicolau, T. Pilizota, B. C. Steel, P. K. Maini, and R. M. Berry, "Conformational spread as a mechanism for cooperativity in the bacterial flagellar switch," *Science*, vol. 327, no. 5966, pp. 685–689, 2010.

[44] Q. Ma, D. V Nicolau, P. K. Maini, R. M. Berry, and F. Bai, "Conformational spread in the flagellar motor switch: a model study.," *PLoS Comput. Biol.*, vol. 8, no. 5, p. e1002523, Jan. 2012.

[45] H. C. Berg and D. A. Brown, "Chemotaxis in Escherichia coli analysed by three-dimensional tracking," *Nature*, vol. 239, no. 5374, pp. 500–504, 1972.

[46] H. C. Berg and P. M. Tedesco, "Transient response to chemotactic stimuli in Escherichia coli.," *Proc. Natl. Acad. Sci. U. S. A.*, vol. 72, no. 8, pp. 3235–9, Aug. 1975.

[47] S. M. S. M. Block, J. E. J. E. Segall, and H. C. H. C. Berg, "Adaptation kinetics in bacterial chemotaxis.," *J. Bacteriol.*, vol. 154, no. 1, pp. 312–23, Apr. 1983.

[48] H. C. Berg, "The bacterial rotary motor," *Enzym.*, vol. XXIII, no. 95, pp. 143–202, 2003.

[49] D. P. Clark, P. Dunlap, M. Madigan, and J. Martinko, "Brock Biology of Microorganisms," *Benjamin Cummings, San Fr.*, 2009.

[50] N. Barkai and S. Leibler, “Robustness in simple biochemical networks,” *Nature*, vol. 387, no. 6636, pp. 913–917, 1997.

[51] M. Welch, K. Oosawa, S.-L. Aizawa, and M. Eisenbach, “Phosphorylation-dependent binding of a signal molecule to the flagellar switch of bacteria,” *Proc. Natl. Acad. Sci. U. S. A.*, vol. 90, no. 19, pp. 8787–8791, Oct. 1993.

[52] F. Matthäus, M. Jagodic, and J. Dobnikar, “E. coli superdiffusion and chemotaxis-search strategy, precision, and motility.,” *Biophys. J.*, vol. 97, no. 4, pp. 946–57, Aug. 2009.

[53] Y. V Kalinin, L. Jiang, Y. Tu, and M. Wu, “Logarithmic sensing in Escherichia coli bacterial chemotaxis.,” *Biophys. J.*, vol. 96, no. 6, pp. 2439–48, Mar. 2009.

[54] B. A. Mello and Y. Tu, “Perfect and near-perfect adaptation in a model of bacterial chemotaxis,” *Biophys. J.*, vol. 84, no. 5, pp. 2943–56, May 2003.

[55] C. H. Hansen, R. G. Endres, and N. S. Wingreen, “Chemotaxis in Escherichia coli: a molecular model for robust precise adaptation.,” *PLoS Comput. Biol.*, vol. 4, no. 1, p. e1, Jan. 2008.

[56] B. Taylor and D. E. Koshland, “Reversal of flagellar rotation in monotrichous and peritrichous bacteria: generation of changes in direction,” *J. Bacteriol.*, 1974.

[57] L. Xie, T. Altindal, S. Chattopadhyay, and X. L. Wu, “Bacterial flagellum as a propeller and as a rudder for efficient chemotaxis,” *Proc. Natl. Acad. Sci.*, vol. 108, no. 6, pp. 2246–2251, 2011.

[58] T. Altindal, L. Xie, and X. L. Wu, “Implications of three-step swimming patterns in bacterial chemotaxis,” *Biophys. J.*, vol. 100, no. 1, pp. 32–41, Jan. 2011.

[59] P. S. Poole and J. P. Armitage, “Motility response of Rhodobacter sphaeroides to chemotactic stimulation.,” *J. Bacteriol.*, vol. 170, no. 12, pp. 5673–9, Dec. 1988.

[60] H. L. Packer, H. Lawther, and J. P. Armitage, “The Rhodobacter sphaeroides flagellar motor is a variable-speed rotor,” *FEBS Lett.*, vol. 409, no. 1, pp. 37–40, Jun. 1997.

[61] K. Son, J. S. Guasto, and R. Stocker, “Bacteria can exploit a flagellar buckling instability to change direction,” *Nat. Phys.*, vol. 9, no. 8, pp. 494–498, Jul. 2013.

[62] T. Doyle, A. Hawkins, and L. McCarter, “The Complex Flagellar Torque Generator of Pseudomonas aeruginosa,” *J. Bacteriol.*, vol. 186, no. 19, pp. 6341–6350, 2004.

[63] S. L. Porter, G. H. Wadhams, and J. P. Armitage, “Signal processing in complex chemotaxis pathways,” *Nat. Rev. Microbiol.*, vol. 9, no. 3, pp. 153–165, Mar. 2011.

[64] C. K. Stover, X. Q. Pham, A. L. Erwin, S. D. Mizoguchi, P. Warrener, M. J. Hickey, F. S. Brinkman, W. O. Hufnagle, D. J. Kowalik, M. Lagrou, R. L. Garber, L. Goltry, E. Tolentino, S. Westbrock-Wadman, Y. Yuan, L. L. Brody, S. N. Coulter, K. R. Folger, A. Kas, K. Larbig, R. Lim, K. Smith, D. Spencer, G. K. Wong, Z. Wu, I. T. Paulsen, J. Reizer, M. H. Saier, R. E. Hancock, S. Lory, and M. V Olson, "Complete genome sequence of Pseudomonas aeruginosa PAO1, an opportunistic pathogen.," *Nature*, vol. 406, no. 6799, pp. 959–964, Aug. 2000.

[65] A. Darzins, "Characterization of a Pseudomonas aeruginosa gene cluster involved in pilus biosynthesis and twitching motility: sequence similarity to the chemotaxis proteins of enterics and the gliding bacterium Myxococcus xanthus," *Mol. Microbiol.*, vol. 11, no. 1, pp. 137–153, 1994.

[66] C. B. Whitchurch, A. J. Leech, M. D. Young, D. Kennedy, J. L. Sargent, J. J. Bertrand, A. B. T. Semmler, A. S. Mellick, P. R. Martin, R. a Alm, M. Hobbs, S. a Beatson, B. Huang, L. Nguyen, J. C. Commolli, J. N. Engel, A. Darzins, and J. S. Mattick, "Characterization of a complex chemosensory signal transduction system which controls twitching motility in Pseudomonas aeruginosa," *Mol. Microbiol.*, vol. 52, no. 3, pp. 873–893, May 2004.

[67] D. A. D'Argenio, M. W. Calfee, P. B. Rainey, and E. C. Pesci, "Autolysis and autoaggregation in Pseudomonas aeruginosa colony

morphology mutants," *J. Bacteriol.*, vol. 184, no. 23, pp. 6481–6489, 2002.

[68] J. W. Hickman, D. F. Tifrea, and C. S. Harwood, "A chemosensory system that regulates biofilm formation through modulation of cyclic diguanylate levels," *Proc. Natl. Acad. Sci. U. S. A.*, vol. 102, no. 40, pp. 14422–14427, Oct. 2005.

[69] Z. T. Güvener, D. F. Tifrea, and C. S. Harwood, "Two different Pseudomonas aeruginosa chemosensory signal transduction complexes localize to cell poles and form and remould in stationary phase," *Mol. Microbiol.*, vol. 61, no. 1, pp. 106–118, Jul. 2006.

[70] S. L. Bardy and J. R. Maddock, "Polar localization of a soluble methyl-accepting protein of Pseudomonas aeruginosa," *J. Bacteriol.*, vol. 187, no. 22, pp. 7840–7844, 2005.

[71] M. E. Davey and G. A. O'toole, "Microbial biofilms: from ecology to molecular genetics," *Microbiol. Mol. Biol. Rev.*, vol. 64, no. 4, pp. 847–867, 2000.

[72] R. Morgan, S. Kohn, S.-H. Hwang, D. J. Hassett, and K. Sauer, "BdlA, a chemotaxis regulator essential for biofilm dispersion in Pseudomonas aeruginosa.," *J. Bacteriol.*, vol. 188, no. 21, pp. 7335–43, Nov. 2006.

[73] M. Klausen, A. Heydorn, P. Ragas, L. Lambertsen, A. Aaes-Jørgensen, S. Molin, and T. Tolker-Nielsen, "Biofilm formation by Pseudomonas

aeruginosa wild type, flagella and type IV pili mutants," *Mol. Microbiol.*, vol. 48, no. 6, pp. 1511–1524, May 2003.

[74] J. Adler, "A method for measuring chemotaxis and use of the method to determine optimum conditions for chemotaxis by Escherichia coli," *J. Gen. Microbiol.*, vol. 74, no. 1, pp. 77–91, Jan. 1973.

[75] J. Adler, "Chemotaxis in bacteria," *Science*, vol. 44, pp. 341–56, Jan. 1966.

[76] M. Wu, J. W. Roberts, S. Kim, D. L. Koch, and M. P. DeLisa, "Collective bacterial dynamics revealed using a three-dimensional population-scale defocused particle tracking technique.," *Appl. Environ. Microbiol.*, vol. 72, no. 7, pp. 4987–94, Jul. 2006.

[77] J. Yuan and H. C. Berg, "Resurrection of the flagellar rotary motor near zero load.," *Proc. Natl. Acad. Sci. U. S. A.*, vol. 105, no. 4, pp. 1182–5, Jan. 2008.

[78] B. E. Scharf, K. A. Fahrner, L. Turner, and H. C. Berg, "Control of direction of flagellar rotation in bacterial chemotaxis.," *Proc. Natl. Acad. Sci. U. S. A.*, vol. 95, no. 1, pp. 201–6, Jan. 1998.

[79] C. Qian, C. C. Wong, S. Swarup, and K.-H. Chiam, "Bacterial tethering analysis reveals a 'run-reverse-turn' mechanism for pseudomonas species motility," *Appl. Environ. Microbiol.*, vol. 79, no. 15, pp. 4734–4743, Aug. 2013.

[80] M. Kojadinovic, A. Sirinelli, G. H. Wadhams, and J. P. Armitage, “New Motion Analysis System for Characterization of the Chemosensory Response Kinetics of Rhodobacter sphaeroides under Different Growth Conditions.,” *Appl. Environ. Microbiol.*, vol. 77, no. 12, pp. 4082–8, Jun. 2011.

[81] P. S. Poole, D. R. Sinclair, and J. P. Armitage, “Real time computer tracking of free-swimming and tethered rotating cells,” *Anal. Biochem.*, vol. 175, no. 1, pp. 52–58, Nov. 1988.

[82] S. Chen, M. Beeby, and G. Murphy, “Structural diversity of bacterial flagellar motors,” *EMBO J.*, vol. 30, no. 14, pp. 2972–2981, Jul. 2011.

[83] J. Kato, H.-E. Kim, N. Takiguchi, A. Kuroda, and H. Ohtake, “Pseudomonas aeruginosa as a model microorganism for investigation of chemotactic behaviors in ecosystem.,” *J. Biosci. Bioeng.*, vol. 106, no. 1, pp. 1–7, Jul. 2008.

[84] E. Kanda, T. Tatsuta, T. Suzuki, F. Taguchi, K. Naito, Y. Inagaki, K. Toyoda, T. Shiraishi, and Y. Ichinose, “Two flagellar stators and their roles in motility and virulence in Pseudomonas syringae pv. tabaci 6605.,” *Mol. Genet. Genomics*, vol. 285, no. 2, pp. 163–74, Feb. 2011.

[85] M. W. Silby, C. Winstanley, S. a C. Godfrey, S. B. Levy, and R. W. Jackson, “Pseudomonas genomes: diverse and adaptable.,” *FEMS Microbiol. Rev.*, vol. 35, no. 4, pp. 652–80, Jul. 2011.

[86] C. S. Harwood, K. Fosnaugh, and M. Dispensa, “Flagellation of Pseudomonas putida and analysis of its motile behavior.,” *J. Bacteriol.*, vol. 171, no. 7, pp. 4063–6, Jul. 1989.

[87] R. M. Macnab, “Examination of bacterial flagellation by dark-field microscopy,” *J. Clin. Microbiol.*, vol. 4, no. 3, pp. 258–265, 1976.

[88] L. Ping, “Swimming behavior of the monotrichous bacterium Pseudomonas fluorescens SBW25,” *FEMS Microbiol.*, vol. 86, no. 1, pp. 36–44, Jan. 2013.

[89] K. B. Barken, S. J. Pamp, L. Yang, M. Gjermansen, J. J. Bertrand, M. Klausen, M. Givskov, C. B. Whitchurch, J. N. Engel, and T. Tolker-Nielsen, “Roles of type IV pili, flagellum-mediated motility and extracellular DNA in the formation of mature multicellular structures in Pseudomonas aeruginosa biofilms,” *Environ. Microbiol.*, vol. 10, no. 9, pp. 2331–2343, Sep. 2008.

[90] E. Keogh, S. Chu, D. Hart, and M. Pazzani, “Segmenting time series: A survey and novel approach,” *Data Min. time Ser. databases*, vol. 57, pp. 1–22, 2004.

[91] J. E. Segall, S. M. Block, and H. C. Berg, “Temporal comparisons in bacterial chemotaxis.,” *Proc. Natl. Acad. Sci. U. S. A.*, vol. 83, no. 23, pp. 8987–91, Dec. 1986.

[92] M. Eisenbach, A. Wolf, M. Welch, S. R. Caplan, I. R. Lapidus, R. M. Macnab, H. Aloni, and O. Asher, “Pausing, switching and speed fluctuation of the bacterial flagellar motor and their relation to motility and chemotaxis.,” *J. Mol. Biol.*, vol. 211, no. 3, pp. 551–63, Feb. 1990.

[93] S. C. Kuo and D. E. Koshland, “Multiple kinetic states for the flagellar motor switch.,” *J. Bacteriol.*, vol. 171, no. 11, pp. 6279–87, Nov. 1989.

[94] C. M. Toutain, M. E. Zegans, and G. A. O’Toole, “Evidence for Two Flagellar Stators and Their Role in the Motility of Pseudomonas aeruginosa,” *J. Bacteriol.*, 2005.

[95] C. M. Toutain, N. C. Caizza, M. E. Zegans, and G. a O’Toole, “Roles for flagellar stators in biofilm formation by Pseudomonas aeruginosa.,” *Res. Microbiol.*, vol. 158, no. 5, pp. 471–7, Jun. 2007.

[96] M. Theves, J. Taktikos, V. Zaburdaev, H. Stark, and C. Beta, “A bacterial swimmer with two alternating speeds of propagation.,” *Biophys. J.*, vol. 105, no. 8, pp. 1915–24, Oct. 2013.

[97] H.-H. Jeong, S.-H. Lee, J.-M. Kim, H.-E. Kim, Y.-G. Kim, J. Y. Yoo, W.-S. Chang, and C.-S. Lee, “Microfluidic monitoring of Pseudomonas aeruginosa chemotaxis under the continuous chemical gradient.,” *Biosens. Bioelectron.*, vol. 26, no. 2, pp. 351–6, Oct. 2010.

[98] M. Hashimoto, T. Mashimo, T. Hirano, S. Yamaguchi, and S. Aizawa, “Functional roles of the hook in a rotating tethered cell.,” *J. Mol. Biol.*, vol. 375, no. 2, pp. 367–75, Jan. 2008.

[99] H. C. Berg and L. Turner, “Torque generated by the flagellar motor of Escherichia coli.,” *Biophys. J.*, vol. 65, no. 5, pp. 2201–16, Nov. 1993.

[100] Y. Magariyama, S. Sugiyama, K. Muramoto, and R. Rate, “Simultaneous measurement of bacterial flagellar rotation rate and swimming speed,” *Biophys. J.*, vol. 69, no. November, pp. 2154–2162, 1995.

[101] A. Masduki, J. Nakamura, T. Ohga, R. Umezaki, J. Kato, and H. Ohtake, “Isolation and characterization of chemotaxis mutants and genes of Pseudomonas aeruginosa,” *J. Bacteriol.*, vol. 177, no. 4, pp. 948–52, Feb. 1995.

[102] K. Taguchi, H. Fukutomi, A. Kuroda, J. Kato, and H. Ohtake, “Genetic identification of chemotactic transducers for amino acids in Pseudomonas aeruginosa,” *Microbiology*, vol. 143, no. 1997, pp. 3223–9, Oct. 1997.

[103] H. Packer, D. Gauden, and J. Armitage, “The behavioural response of anaerobic Rhodobacter sphaeroides to temporal stimuli,” *Microbiology*, vol. 142, pp. 593–599, Mar. 1996.

[104] U. Alon, M. G. Surette, N. Barkai, and S. Leibler, “Robustness in bacterial chemotaxis.,” *Nature*, vol. 397, no. 6715, pp. 168–71, Jan. 1999.

[105] T.-M. Yi, Y. Huang, M. I. Simon, and J. Doyle, “Robust perfect adaptation in bacterial chemotaxis through integral feedback control,” *Proc. Natl. Acad. Sci. U. S. A.*, vol. 97, no. 9, pp. 4649–4653, Apr. 2000.

[106] A. Ferrández and A. Hawkins, “Cluster II che genes from Pseudomonas aeruginosa are required for an optimal chemotactic response,” *J. ...*, vol. 184, no. 16, pp. 4374–4383, 2002.

[107] B. Alberts, D. Bray, J. Lewis, and M. Raff, “Molecular biology of the cell,” *Garland, New York*, 1994.

[108] Y. Tu, T. S. Shimizu, and H. C. Berg, “Modeling the chemotactic response of Escherichia coli to time-varying stimuli,” *Proc. Natl. Acad. Sci. U. S. A.*, vol. 105, no. 39, pp. 14855–14860, Sep. 2008.

[109] B. A. Mello and Y. Tu, “An allosteric model for heterogeneous receptor complexes: understanding bacterial chemotaxis responses to multiple stimuli,” *Proc. Natl. Acad. Sci. U. S. A.*, vol. 103, no. 11, 2005.

[110] J. E. Keymer, R. G. Endres, M. Skoge, Y. Meir, and N. S. Wingreen, “Chemosensing in Escherichia coli: two regimes of two-state receptors,” *Proc. Natl. Acad. Sci. U. S. A.*, vol. 103, no. 6, pp. 1786–91, Mar. 2006.

[111] L. Jiang, Q. Ouyang, and Y. Tu, “Quantitative modeling of Escherichia coli chemotactic motion in environments varying in space and time,” *PLoS Comput. Biol.*, vol. 6, no. 4, p. e1000735, Apr. 2010.

[112] R. Stocker, J. R. Seymour, A. Samadani, D. E. Hunt, and M. F. Polz, “Rapid chemotactic response enables marine bacteria to exploit ephemeral microscale nutrient patches,” *Proc. Natl. Acad. Sci. U. S. A.*, vol. 105, no. 11, pp. 4209–4214, Mar. 2008.

[113] E. Rosenberg, O. Koren, L. Reshef, R. Efrony, and I. Zilber-Rosenberg, “The role of microorganisms in coral health, disease and evolution,” *Nat. Rev. Microbiol.*, vol. 5, no. 5, pp. 355–362, May 2007.

[114] F. Bai, T. Minamino, Z. Wu, K. Namba, and J. Xing, “Coupling between Switching Regulation and Torque Generation in Bacterial Flagellar Motor,” *Phys. Rev. Lett.*, vol. 108, no. 17, p. 178105, Apr. 2012.

[115] S.-H. Lee and D. G. Grier, “Holographic microscopy of holographically trapped three-dimensional structures.,” *Opt. Express*, vol. 15, no. 4, pp. 1505–12, Feb. 2007.

[116] E. Lauga, W. R. DiLuzio, G. M. Whitesides, and H. A. Stone, “Swimming in circles: motion of bacteria near solid boundaries.,” *Biophys. J.*, vol. 90, no. 2, pp. 400–12, Jan. 2006.

[117] A. Berke, L. Turner, H. C. Berg, and E. Lauga, “Hydrodynamic Attraction of Swimming Microorganisms by Surfaces,” *Phys. Rev. Lett.*, vol. 101, no. 3, pp. 1–4, Jul. 2008.

[118] Y. Magariyama, M. Ichiba, K. Nakata, K. Baba, T. Ohtani, S. Kudo, and T. Goto, “Difference in bacterial motion between forward and backward swimming caused by the wall effect.,” *Biophys. J.*, vol. 88, no. 5, pp. 3648–58, May 2005.

[119] T. Goto, K. Nakata, K. Baba, M. Nishimura, and Y. Magariyama, “A fluid-dynamic interpretation of the asymmetric motion of singly flagellated bacteria swimming close to a boundary.,” *Biophys. J.*, vol. 89, no. 6, pp. 3771–9, Dec. 2005.

[120] E. Korobkova, T. Emonet, J. M. Vilar, T. S. Shimizu, and P. Cluzel, “From molecular noise to behavioural variability in a single bacterium,” *Nature*, vol. 279, no. 13, pp. 12005–8, Mar. 2004.

[121] T. Emonet and P. Cluzel, “Relationship between cellular response and behavioral variability in bacterial chemotaxis.,” *Proc. Natl. Acad. Sci. U. S. A.*, vol. 105, no. 9, pp. 3304–9, Mar. 2008.

[122] H. Park, W. Pontius, C. C. Guet, J. F. Marko, T. Emonet, and P. Cluzel, “Interdependence of behavioural variability and response to small stimuli in bacteria.,” *Nature*, vol. 468, no. 7325, pp. 819–23, Dec. 2010.

[123] J. Yuan, K. a Fahrner, and H. C. Berg, “Switching of the bacterial flagellar motor near zero load.,” *J. Mol. Biol.*, vol. 390, no. 3, pp. 394–400, Jul. 2009.

[124] S. Chattopadhyay, R. Moldovan, C. Yeung, and X. L. Wu, “Swimming efficiency of bacterium Escherichia coli.,” *Proc. Natl. Acad. Sci. U. S. A.*, vol. 103, no. 37, pp. 13712–7, Sep. 2006.

[125] T. L. Min, P. J. Mears, L. M. Chubiz, C. V Rao, I. Golding, and Y. R. Chemla, “High-resolution, long-term characterization of bacterial motility using optical tweezers.,” *Nat. Methods*, vol. 6, no. 11, pp. 831–5, Nov. 2009.

[126] S. M. Vater, S. Weiße, S. Maleschlijski, C. Lotz, F. Koschitzki, T. Schwartz, U. Obst, and A. Rosenhahn, “Swimming behavior of Pseudomonas aeruginosa studied by holographic 3D tracking.,” *PLoS One*, vol. 9, no. 1, p. e87765, Jan. 2014.

[127] N. Vladimirov, L. Løvdok, D. Lebiedz, and V. Sourjik, “Dependence of bacterial chemotaxis on gradient shape and adaptation rate.,” *PLoS Comput. Biol.*, vol. 4, no. 12, p. e1000242, Dec. 2008.

[128] A. Heydorn, A. T. Nielsen, M. Hentzer, C. Sternberg, M. Givskov, B. K. Ersbøll, and S. Molin, “Quantification of biofilm structures by the novel computer program COMSTAT,” *Microbiology*, vol. 146, no. 10, pp. 2395–407, Oct. 2000.

[129] E. Alpkvista, “A multidimensional multispecies continuum model for heterogeneous biofilm development,” *Bull. Math. Biol.*, vol. 69, no. 2, pp. 765–789, Jan. 2007.

[130] I. Klapper, “Mathematical description of microbial biofilms,” *SIAM Rev.*, vol. 52, no. 2, pp. 1–45, 2010.

[131] V. Janakiraman, D. Englert, and A. Jayaraman, “Modeling growth and quorum sensing in biofilms grown in microfluidic chambers,” *Ann. Biomed.*, vol. 37, no. 6, pp. 1206–1216, 2009.

[132] R. Dillon, L. Fauci, A. Fogelson, and D. Gaver III, “Modeling Biofilm Processes Using the Immersed Boundary Method,” *J. Comput. Phys.*, vol. 129, no. 1, pp. 57–73, Nov. 1996.

[133] M. R. Frederick, C. Kuttler, B. A. Hense, and H. J. Eberl, “A mathematical model of quorum sensing regulated EPS production in biofilm communities,” *Theor. Biol. Med. Model.*, vol. 8, no. 1, p. 8, 2011.

7 APPENDIX

Figure 7.1 Comparison between BTAP labeled rotational phases and manual annotated phases

Ten sample cells has illustrated by comparisons between the BTAP labeled rotational phases and manual labeled rotational phases. The red color denotes CW, green color CCW and white color pause.